Turbulence Modeling and Simulation of Unsteady Transitional Boundary Layers and Wakes with Application to Wind-Turbine Aerodynamics

Di Zhang

Dissertation submitted to the Faculty of the
Virginia Polytechnic Institute and State University
in partial fulfillment of the requirements for the degree of

Doctor of Philosophy
in
Aerospace Engineering

Eric G. Paterson, Chair
William J. Devenport
K. Todd Lowe
Anne E. Staples

November 13, 2017
Blacksburg, Virginia

Keywords: Hybrid RANS/LES, DES, Wind Energy, Boundary Layer Transition

Turbulence Modeling and Simulation of Unsteady Transitional Boundary Layers and Wakes with Application to Wind-Turbine Aerodynamics

Di Zhang

(ABSTRACT)

A hybrid RANS/LES turbulence model integrated with transition formulation is developed and tested by a surrogate model problem through joint experimental and computational fluid dynamics approaches. The model problem consists of a circular cylinder for generating coherent unsteadiness and a downstream airfoil in the cylinder wake. The cylinder flow is subcritical, with a Reynolds number of $64,000$ based upon the cylinder diameter.

The quantitative dynamics of vortex shedding and Reynolds stresses in the cylinder near wake were well captured, owing to the turbulence-resolving large eddy simulation method that was invoked in the wake. The power spectrum density of velocity components showed that the flow fluctuations were well-maintained in cylinder wake towards airfoil and the hybrid model switched between RANS/LES mode outside boundary layer as expected. According to the experimental and simulation results, the airfoil encountered local flow angle variations up to $\pm 50^\circ$, and the turbulent boundary layer remained attached. Inspecting the boundary layer profiles over one shedding cycle, the oscillation about mean profile resembled the Stokes layer with zero mean. Further processing the data through phase-averaging technique found phase lags along the chordwise locations and both the phase-averaged and mean profiles collapsed into the Law-of-the-wall in the range of $0 < y^+ < 50$. The features of high blade loading fluctuations due to unsteadiness and transitional boundary layers are of interest in the aerodynamic studies of full-scale wind turbine blades, making the model problem a comprehensive benchmark case for future model development and validation.

Turbulence Modeling and Simulation of Unsteady Transitional Boundary Layers and Wakes with Application to Wind-Turbine Aerodynamics

Di Zhang

(General Audience Abstract)

Wind energy industry thrived in the last three decades, environmental concerns and government regulations stimulate studies on wind farm location selection and wind turbine design. Full-scale experiments and high-fidelity simulations are restrictive due to the prohibitively high cost, while the model-scale experiments and low-fidelity calculations miss key flow physics of of the full-scale models.

The current study adopted a joint experimental and computational fluid dynamic approach to design a surrogate problem that features the unsteady flow physics presented in the full-scale wind turbine blades. A new hybrid turbulence model was implemented and validated against the complementary experimental results. The new model improves the accuracy of the current industry-standard turbulence models without excessive computational cost, making it a viable solution to the high-fidelity full-scale simulations in the future.

Acknowledgments

I would like to express my sincere gratitude to my advisor Dr Eric Paterson and Dr Todd Lowe for their support and guidance during my research.

Thank Dr Tarak Nandi for his help on transition model implementation in OpenFoam.

Thank the Cyber-Wind-Facility team for the opportunity of participating the development a comprehensive computing environment for the wind plant CFD. This experience brought me insights into the wind energy industry and essential skills and tools for conducting the current research.

Thank Advanced Research Computing center in Virginia Tech for high-performance computing support and assistantship during second and third year.

The financial support provided by the Institute for Critical Technology and Applied Science (ICTAS) in Virginia Tech is gratefully acknowledged.

Finally, thank my family for your love and patience to make it all possible.

Contents

7 Numerical Study of Unsteady Boundary Layer of Wind Turbine Airfoils

List of Figures

List of Tables

Chapter 1

Introduction

Modern interests in wind energy emerged after first oil crisis in 1970s. Megawatt wind turbine debuted in 1998. By 2010, $2 \sim 3.6$MW and $5 \sim 6$MW wind turbines became the standard onshore and offshore respectively, a larger 10MW wind turbine has been design and tested offshore [1]. The introduction of 10MW-20MW wind turbine with rotor diameter over 200m is also planned [2].

Wind turbines operate in the eddies and gusts generated by wakes from upstream turbines and atmospheric turbulence. The highly unsteady flow over the rotating blades is characterized by large transient changes in angle-of-attack, laminar-turbulent transition, flow separation and reattachment, and dynamic stall. Most experimental studies use model-scale wind turbine due to the high cost of full-scale testing and the numerical studies are conducted via multiple approaches of different fidelities. Rotor-scale large-eddy simulation (LES) of the blade boundary layer for a full-scale wind turbine still exceeds the state-of-the-art [3]; thus, lower-fidelity models such as the actuator-line model [4] [5] are often used. Unfortunately, lower-fidelity models are incapable of predicting the aforementioned unsteady flow phenomena. The uncertainty in wind energy industry remains high compared with traditional energy sources.

While the LES of full-scale turbulent rotor flow is still too expensive for most practical problems, the next order of fidelity, Reynolds-averaged Navier Stokes (RANS) models cannot replicate many complex flow features. As such, RANS approaches currently fall short in precisely predicting the shaft torque at stall, as laminar/turbulent transition and flow separation have both been shown to have a first-order effect on blade aerodynamics predictions [5]. Full-scale CFD studies show that increasing RANS fidelity for separated flows and wake regions by employing detached-eddy simulation (DES) can significantly improve predictions of blade torque near stall compared with RANS [6] [7] [8] and the application of the hybrid RANS/LES model yields nearly identical solutions compared with RANS at low wind speed.

One of the major difficulties in full-scale CFD is the large diversity of both temporal and spatial scales in wind plant operation conditions. In the atmospheric boundary layer, the energy-containing motions are on the time scale of minutes and the length scale from 10 to 1000 meters. The attached blade surface viscous layers are on the order of milliseconds with length scale from 10 to 100 microns [3]. Thus, neither RANS nor LES models perform well across the entire time/space range.

The hybrid RANS/LES model in this study is based on a correlation-based four-equation RANS transition model, which integrates two local-variable transport equations with the shear stress transport (SST) $k-\omega$ turbulence model framework [9]. It is capable of capturing natural, bypass and separation-induced transition [10]. An application of the transition model to a small, full-scale wind turbine in the literature showed improved agreement with experiments compared with RANS and engineering models [11]. For a wind turbine operating in the wake of an upstream turbine, blades experience large variations in angle of attack, the transition model alone helps capturing the load hysteresis loop in dynamic stall [12]. Recent study assessed the effects of blade boundary layer transition inside atmospheric turbulence eddies through blade-resolved simulation and full-scale field experiments, the boundary layer separation is closely correlated with the transition location in off-design conditions, where the blade experiences massive separations and deep stall [13]. Despite the improvement,

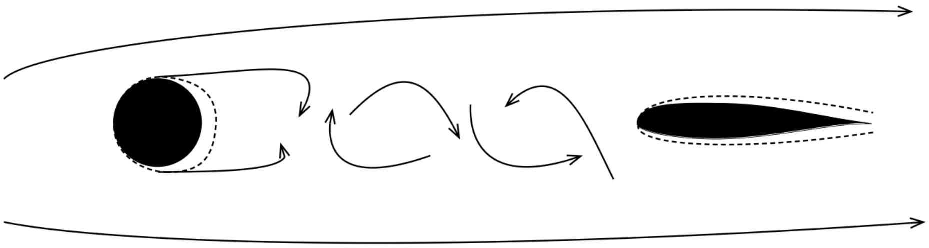

Figure 1.1: Surrogate model overview

however, further development is needed for properly predicting the reattachment process.

In the current effort, a new surrogate model problem (figure 1.1) is developed that encompasses key flow physics such as large-scale, rotational unsteadiness and a transitional boundary layers over an aerodynamic body. Detailed experimental results have been obtained, providing quantitative data for comparison and insight that guides model developments. Leveraging the new insight, we have developed a novel hybrid RANS/LES approach which includes transition modeling and, thus, has the advantages of resolving the energy-containing turbulence structures generated upstream of the blade, while improving the fidelity of physics modeled in the blade boundary layer region. Some preliminary results of circular cylinder flow and airfoil boundary layer were published in [14].

1.1 Thesis Outline

This thesis consists of 8 chapters that focus on developing and testing a new transition hybrid turbulence model through a joint numerical/experimental study of a surrogate problem, a summary of each chapter is as follows:

Chapter I is an overview of the thesis, a general introduction and motivation.

Chapter II reviews related studies of numerical/experimental wind turbine design and testing.

Chapter III introduces solution algorithms and implementation of the transition hybrid turbulence model.

Chapter IV presents the surrogate model design with key model parameters.

Chapter V tests the transition model performance using results from original model implementation and experimental data.

Chapter VI is an analysis of the circular cylinder flow which is used as the surrogate atmospheric turbulence. It also serves as a comprehensive test of the full transition hybrid model.

Chapter VII analyzes the unsteady flow physics in airfoil boundary layer and compares with the available experimental data.

Chapter VIII summarizes the whole thesis with a revision of the major conclusions and a prognosis of future applications to large-scale models.

1.2 Ph.D Research Objectives

The objectives of my research are:

- To construct a surrogate problem that captures the essence of the the unsteady flow physics of a wind turbine blade rotating through wakes and atmospheric turbulence, and which can be inexpensively tested in a wind tunnel.
- To develop a new hybrid RANS/LES turbulence model that incorporates transition prediction.
- To implement the new turbulence model and test its performance by analyzing the unsteady transitional boundary layer and wake from experiments and simulations data.

- To formulate a benchmark problem for future model development and validation.

This study aims to seek a new turbulence modeling approach for addressing the difficulties in high-fidelity wind turbine CFD. For full-scale transitional and/or separated flow on the turbine blade, neither RANS or LES is capable of solving the whole flow field with acceptable accuracy and cost, and furthermore, boundary layer transition is proven to play significant role in predicting blade loading and power production. The transition hybrid model developed in this study provides improved prediction compared with RANS without excessive cost.

Chapter 2

Previous and Related Studies

2.1 Wind Energy Industry Overview

The first wind turbine generating electricity was built in 1891 by Danish engineer Dane Poul la Cour, the modern wind energy industry was revived after the first oil crisis in 70s. From the beginning of this decade, over 100 billion US dollar is invested in the wind power industry worldwide every year [15]. By the end of 2015, 41% of worldwide wind energy capacity was install in Asia, followed by 34% in Europe and 21% in North America [15]. Compared with 2010, wind power capacity increased by 120% in 5 years, Asia saw the fastest boost of 177% in the same period of time. In Europe, the main driver of wind energy is the fixed feed-in tariffs for wind power, which reduces financial risk for wind power investors. In America, federal government provides wind power industry 2.2cents/kWh tax credit since 1992, state-level policy continues to stimulate local wind power installations [16]. US government aims to reach 20% energy penetration nationwide by 2030 [17]. Currently, China replaced US with the most wind energy installed and has initiated offshore wind power projects after Europe.

Wind energy requires moderate integration cost, and no additional storage is required in large balancing areas. However, the uncertainty in wind energy industry is relatively high, for a single wind power plant, the mean absolute error varies from $4 - 12\%$ to $12 - 25\%$ for hourly and day-ahead forecasts [18]. The wind plant capacity factor is comparable to hydropower plant, at 30% [17]. As technology advances over time, the wind power price drops to less than one-sixth since early 1980s. Current wind power installation cost ranges from $\$2000/kw$ to $\$2500/kw$, which is lower than coal power plants ($\$3000/kw$ to $\$4000/kw$) and nuclear power plants ($\$4000/kw$ to $\$8000/kw$).

Most wind turbines used today are horizontal-axis type turbines. The three-blade design has the advantage of better rotor moment handling and lower noise level [19], and it dominates the market of grid-connected wind turbines. All the related work mentioned in this chapter is about the horizontal-axis wind turbine(HAWT).

2.2 Role of Aerodynamics in Wind Turbine Design

From 1970s to the current time, distinct wind turbine design philosophy in each time period determines the wind turbine characteristics. Early design pursues maximum power coefficients at various wind speed, the wind turbine aerodynamic study is mostly conducted via low-fidelity engineering model, e.g. Blade Element Momentum(BEM) theory, the interactions between the wind turbine and inflow turbulence were less considered [20].

Today, wind energy directly competes with conventional energy sources, e.g. hydropower and nuclear energy, the emphasis is on minimizing the energy cost. The most notable design trend are the growth of wind turbine rotor size for higher energy harvest and the use of composite materials for less weight and higher structural rigidity [21]. Large span of the rotor brings higher tip-speed ratio compared with smaller wind turbines, the tip design becomes a key element of blade performance [22]. Maintenance cost is one of the dominant factors that determine the wind energy cost, excessive loadings and fatigue cause premature drivetrain failure [23], the down time of the wind turbine further reduces the capacity factor. Therefore, it is essential for the wind turbine to meet or exceed the standards of operating under extreme aerodynamic conditions [24].

In recently years, engineers focused on installing offshore wind turbines for higher energy density and less environmental impact. Furthermore, the large coastal cities in the vicinity of offshore wind farm help reducing the integration cost of the wind energy. The impact of ocean waves on either buoy platforms or monopiles introduces significantly structural loadings. Both CFD and engineering models are applied to study the wave force impact on the structure [25], which is further integrated with aerodynamic forces on rotor for total loadings on wind turbine [26]. The full-scale experimental studies of wind turbine are restricted due to the large size and high cost of the test rig, no wind tunnel can accommodate a full-scale commercial wind turbine. The experimental aerodynamics is usually studied via model-scale wind turbine and some essential flow physics, e.g. transition and separation on full-scale turbine blades, are not captured.

2.3 CFD Application in Wind Energy Industry

2.3.1 CFD study of wind plant

Wind turbines operate in the eddies and gusts generated by wakes from upstream turbines and atmospheric turbulence(figure 2.1). With the growth of computing power, extensive studies have been conducted on wind plant CFD. The Penn State Cyber-Wind-Facility (CWF) project [26], which was supported by the U.S. Department of Energy, developed a high-fidelity multi-scale computing environment for conducting “cyber field experiments” and collecting “cyber data” on turbines operating in neutral and moderately convective atmospheric boundary layer (ABL).

Owing to the highly-unsteady flow behind each turbine, LES leads the current trend in wind plant aerodynamics and its results are used for improving engineering models [28]. Studies found higher turbulence intensity helps mixing in the ABL and thus increases power

Figure 2.1: Horns Rev wind farm illustrating unsteady inflow from upstream turbines [27]

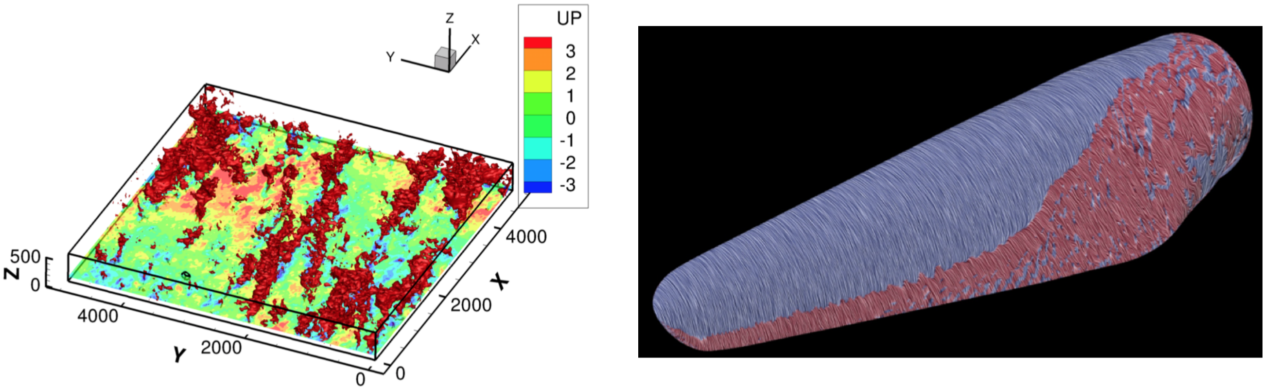

Figure 2.2: Cyber Wind Facility simulation of atmospheric turbulence and visualization of blade boundary layer separation streamlines [3]

production of the wind farm [29]. The terrain surface roughness and ABL stability also has significant effects on the turbine loads and power production [30]. Compare with the less expensive RANS model, LES predicts slower wake recovery and thus lower power production [31].

As the least expensive approach, engineering models provide the fastest but least accurate prediction than RANS and LES [32]. Actuator-Line Model(ALM) is widely used for wind turbine aerodynamics. In CWF, ALM was integrated in general-purpose open-source CFD software OpenFOAM [33], the implementation was validated by experimental results and other engineering code [4]. ALM enables the studies of multi-turbine and turbine-turbine interactions in atmosphere turbulence at low cost. The effect of wind turbine wake on downstream turbine performance was studied extensively by large-eddy simulation (LES) coupled with ALM [34].

The ambitious 3-year CWF project made good progress on developing tools at several levels of fidelity, simultaneously resolving both atmospheric eddies on micro-scale LES domains ($5km \times 5km \times 0.5km$) and blade boundary layers on rotating machines still exceed the state-of-the-art. The adoption of low-fidelity engineering model neglects important unsteady flow physics, which has significant impact on wind turbine performance prediciton in off-design conditions [13].

2.3.2 CFD study of full-scale wind turbine

As in the wind plant CFD studies, instead of resolving the blade boundary layers, the full-scale wind turbine flow is usually calculated by the low-fidelity engineering model that projects the turbine loadings onto the passing flow as body force [35]. Since airfoil data is used to calculate sectional blade force and ignores atmospheric turbulence effect and spanwise flow dynamics, it is inaccurate at high turbulence intensity and largely-separated cases. Furthermore, force projection introduces extra uncertainties into the model. As the medium-fidelity approach, RANS model suffers from the same problem at predicting wind turbine performance at stall conditions.

LES of high-fidelity full-scale turbulent rotor flow is still expensive today. As an alternative approach, the hybrid RANS/LES model yields nearly identical solutions as from RANS at low wind speed, and it provides significantly improved prediction of turbine torque in fully-stalled and yawed flows [6]. Fluid Structure Interaction(FSI) in full-scale study introduces another level of complexity, a fully-coupled aerodynamics and FSI framework was introduced to study interactions of rotor with nacelle and tower [36–38].

2.3.3 CFD study of wind turbine blade flow

Full-scale turbine blade flow is widely studied by CFD techniques. Blade torque prediction from RANS simulation of single rotating blade has poor agreement with experimental data at near stall conditions [7]. Zonal hybrid turbulence model was introduced in CWF project for computing the variations of space-time loadings on a full-scale Single-Rotating-Blade-In-Atmosphere(SRBIA) [3]. The zonal approach requires knowledge and/or experience at defining the explicit switching interface and thus impractical for flow problems with complex geometries.

The effects of flow separation can be captured by Detached-Eddy Simulation(DES) and the force and pressure prediction compares fairly well even at largely-separated flow [8]. The two-equation transition model integrated with RANS further improves the prediction of the 1^{st} order transition effect on blade [5, 39, 40].

CFD study of blade flow is an important approach in blade-design process, studies found that improved blade tip increases ratio of torque over thrust [22] and optimized inboard blade twist and trailing edge thickness yield in higher power capturing [41].

2.4 Wind Turbine Aerodynamics Experiments

2.4.1 Model-scale wind turbine experiments

Due to the high cost of full-scale wind turbine testing, most experimental studies use model-scale instead. Experiments on wind plant aerodynamics facilitate better understanding of the interactions between atmosphere and wind turbine array. Studies show that the free stream turbulence level has significant effect on model turbine blades' aerodynamics [42], combined with upstream turbine wake, the downstream wind turbine power loss can be up to 46%. By operating the upstream turbine in yawed condition, which deflects its wake, helps increasing total power output of the wind plant [43]. The model testing data is also used for validation purpose of dynamics models in LES framework [44].

2.4.2 Full-scale wind turbine experiments

Wake flow measurement from model-scale wind turbine significantly differs from full-scale experimental data, mainly due to the boundary layer behaviors of model blade [45]. NREL's extensive Unsteady Aerodynamics Experiment (UAE) in NASA Ames wind tunnel [46] offers valuable data for both engineering and CFD model calibration and validation. For FSI studies, an innovative approach was suggested to use hydraulic shakers for testing structural dynamics due to aerodynamic loading and the results compared very well with modes from wind excitation [47]. Extra structural loadings are induced by ocean waves on offshore wind turbine, the dynamic properties of the full-machine were calculated via rotor-stop tests [48, 49] and it is vital to avoid resonance at different sea conditions.

2.5 Turbulence Modeling

2.5.1 Transition models

Transition prediction can be categorized into two groups: either use 1) low-Reynolds number turbulence model or 2) experimental correlations. The first approach utilizes damping factor of low-Reynolds number formulations of various one- and two-equation turbulence models at wall proximity. It only accounts for flow variations in the wall-normal direction and other factors that affects transition, e.g. freestream turbulence intensity, separation, wall roughness, are not captured [50].

The second approach is favored by engineers and researchers, it typically correlates freestream turbulence intensity with momentum thickness Reynolds number at transition onset [9]. Experiments conducted on flat-plate was investigated at different pressure gradient and freestream turbulence levels over a significant range. Empirical correlations for the start and end position of transition were established for various boundary layer parameters [51]. This classical methodology mandates a comparison between momentum thickness Reynolds number and the transition value from correlations. An extensive integration and search for the critical values introduces global operations, extra computations and uncertainties from integration algorithms.

In the context of large-scale parallel computing, global operations increase communications overhead among processors, which significantly reduce scaling of parallel computing. Menter et al. [52] introduced a novel approach that only requires local information by using vorticity Reynolds number to link correlation with turbulence intermittency and instead of integration operation, the transition momentum thickness Reynolds number is computed by a transport equation in freestream and diffused into boundary layer [9].

The two-equation correlation-based transition model provides a framework for incorporating other transition mechanisms and also for improved correlations. Detailed formulations will be given in Chapter III.

2.5.2 Hybrid RANS/LES methods

One of the major difficulties in full-scale CFD is the disperse of both time and space scales in wind plant operation. In atmospheric boundary layer, the energy containing motions are in the time scale of minutes with a length scale from 10 to 1000 meters, while the time scales of attached blade surface viscous layers are in the order of milliseconds with length scale from 10 to 100 microns [3]. The hybrid RANS/LES model is designed to predict the turbulence across all regions by switching modes across boundary layer and freestream flow.

The hybrid RANS/LES model in our study is based on a correlation-based four-equation RANS transition model, which integrates two local-variable transport equations into the shear stress transport (SST) $k-\omega$ turbulence model framework [9]. It is capable of capturing natural, bypass and separation-induced transition [10]. Study showed the application of transition model to a small full-scale wind turbine gives the best agreement with experimental results compared with RANS and low-fidelity engineering model [11]. For wind turbine operating in the wake, turbine blades experience large variation in angle of attack, basic transition model helps fairly capturing the load hysteresis loop in dynamic stall and further improvements are needed in predicting the reattachment process [12]. The hybrid transition RANS/LES approach in this study has the advantage of resolving the energy containing turbulence structures in cylinder wake and predicting transition and other turbulent boundary layer dynamics on the downstream airfoil.

2.6 Unsteady Boundary Layer and Wakes

Unsteady viscous flow can be generally categorized into impulsive and oscillatory motions, the oscillatory flow can be further divided into zero mean and non-vanishing mean flows

[53]. Analytical solutions of many model problems are derived through various analyzing approaches, e.g. perturbation methods, triple decomposition.

One of the most well-know example is the Stokes flow, which is created by oscillations of an infinite flat plate. The fluctuations of the motion die out exponentially as they move away from the wall. The oscillations have the same frequency throughout the flow, but there is a phase lag proportional to the distance from the wall. Despite its simple formulation, Stokes layer is quite often embedded in various flow fields with properties almost independent of the other fields. Flow phenomena that resembles Stokes layer is observed in airfoil boundary layer from our experimental results.

It is more complicated to study the mean and fluctuations of non-vanishing mean oscillatory flow. For organized oscillations, each term in the governing equations can be decomposed into three components, the mean, organized oscillations and random fluctuations. Such decomposing technique is call *triple decomposition*.

The analytical solutions of unsteady flow are usually based on multiple assumptions and simplifications. For example, the boundary layer equation assumes small amplitude fluctuations in the outer flow. As the unsteadiness grows, a wave-like disturbance with wavelength of the order of boundary layer thickness travels downstream and the fluctuations boundary layer equations are no longer valid [54]. This type of flow makes analytical analysis more complicated if not possible and numerical studies are often the only practical approach apart from experiments.

2.7 Flow Around a Circular Cylinder

Cylinder flow has been extensively studies both experimentally and numerically. Zdravkovich [55] categorized cylinder flow into 4 groups: at $Re_D < 200$ flow remains laminar; transition starts to take place in cylinder wake for $200 < Re_D < 400$. For $400 < Re_D < 100,000 - 200,000$ the transition moves upstream into the shear layers and it initiates along the free shear layers while the attached boundary layers remain fully laminar, flow in the shear layer bursts to turbulence at $20,000 - 40,000 < Re_D < 100,000 - 200,000$. Cylinder flow in this particular state, when transition takes place in shear layers, is called subcritical. The drag crisis happens at $100,000 - 200,000 < Re_D < 300,000 - 340,000$, transition starts in the attached boundary layer on cylinder, the onset of transition disturbs the near-wake and delays the eddy formation, which leads to an initial fall in the drag coefficient. As Reynolds number continue going up, transition moves further upstream before separation, and the cylinder flow is in supercritical regime.

2.7.1 Circular cylinder flow physics at subcritical Reynolds number

Our study focuses on cylinder Reynolds number at $Re_D = 64,000$, which corresponds to the region that flow in shear layer bursts to turbulence. The length of eddy formation region L_f, which is defined as the distance from cylinder rear stagnation point to the maximum vorticity in the wake centerline, decreases and the transition eddies disappear in the free shear layers compared with cylinder flow at lower Reynolds number. However, L_f and transition length L_t (the mean transition length in shear layer from laminar to turbulent) remain constant until supercritical regime. Shorter eddy formation region also results in wider near-wake, despite its relatively moderate Reynolds number, the subcritical cylinder flow at this regime is often encountered in chemical and mechanical engineering [55].

Hot-wire experiment shows laminar high velocity and turbulent low velocity fluctuations in free shear layer, which confirms the behavior of sudden burst into turbulence [56]. Low frequency oscillation across cylinder span leads to amplitude modulation and phase lag in hot-wire signal at various spanwise locations [57]. The velocity fluctuation period varies as large as 15% between cycles, one can thus only rely on average Strouhal number instead of instantaneous frequency [58].

The spanwise correlation coefficient [55] is defined as

$$R_{12} = \frac{(v_1' + v_2')^2 - (v_1' - v_2')^2}{4(v_1' \times v_2')^{1/2}}$$

Where v_1' and v_2' are velocity components at spanwise location 1 and 2. The correlation length is thus given as

$$L_c = \int_0^\infty R_{12}(z)dz$$

Shimizu and Kawamura [59] studied correlation length for cylinder Reynolds number ranges from 10^3 up to 10^5. L_c decreases from $12D$ at low Re down to $4D$ at $10^4 < Re_D < 10^5$. L_c also has strong dependance on cylinder aspect ratio L/D for $Re_D < 10^4$.

The mean Strouhal number is of primary importance for practical applications. As the correlation length, it approaches approximately 0.2 for all Reynolds number regimes($10^3 - 10^5$) that have transition in shear layer. However, scatter of instant St is still a genuine feature, which may vary up to ±10% [60].

The eddy shedding mechanism is complicated and interacts with the free stream. The roll-up of free shear layers create eddies at a almost fixed location. The eddies are then carried downstream and diffuse and decay along the wake. The diffused free shear layer grows in thickness, which decrease the shedding frequency, while the shortening of L_f as Re_D increase counteracts its effect and thus St remains constant. The eddy strength is related to the rate of vorticity generation and dissipation, which are similar throughout the subcritical regime, thus the strength of fully grown eddy is constant [60]. The entrainment of the adjacent free stream into the wake creates confluence points, which alternate at both sides of the cylinder near-wake. The entrainment stream displaces and elongates the eddies, the split eddy is then shed when it is engulfed by the entrainment stream [61].

2.7.2 Computational study of circular cylinder flow at subcritical Reynolds number

Extensive effort was devoted to the numerical studies of circular cylinder flow. The use of turbulence model ranges from 2D URANS to boundary-layer-resolved LES. The URANS simulation is relatively cheap, requires number of grids $N \sim logRe$, while the LES for wall-boundary flow requires $N \sim Re^{1.76}$ and LES for off-body flow requires $N \sim Re^{0.4}$ [62].

As one of the most studied configurations, the prediction of acoustic field around tandem cylinders are used for estimating the noise of aircraft landing gear system [63]. The low-cost URANS model cannot resolve small vortex structures, which influence each other to form large vortex structures through pairing process [64], and the use of incompressible solver mandates a second step using an acoustic analogy to transform the aerodynamic results into acoustic pressure [65]. Various hybrid model provided an affordable approach for accurate prediction of tandem cylinder problem by keeping turbulence model operating in RANS mode in wall-boundary flow, while switching to LES in off-body flow. The hybrid model helps improving the prediction of the flow forces in the wake interference regime and the Splart-Allmaras and $k-\omega$ SST based DDES/IDDES model were shown to provide good agreement with experiments in terms of drag and shedding frequency [62] [66]. A new hybrid approach named *Flow Simulation Methodology(FSM)* controls the dissipation of turbulence kinetic energy and the production of eddy viscosity in the limit between RANS and DNS, the calculation is seamless blended across all resolutions. Good agreement was found between FSM simulations and experiment and the effect of base model choice for FSM were also studied [67].

Some LES studies were conducted for single-circular-cylinder flow at moderately Reynolds number. Different LES models were assessed, less dissipative numerical algorithms are generally required for resolving the turbulence energy spectrum down to the inertial subrange, providing that the mesh resolution is fine enough [68]. Both von Karman and Kelvin-Helmholtz instability are captured by *power spectral density(PSD)* of the transverse velocity along the wake centerline [69]. Due to its complex nature of LES computations, grid refinement didn't necessarily lead to improved results compared with experiment data, i.e. the reduction of certain error source doesn't always lead to better predictions [70].

2.7.3 Experimental study of circular cylinder flow at subcritical Reynolds number

Experimental studies on circular cylinder focus on various aspects of the flow problems, including aero-acoustic [71], spanwise correlation [72], vortex and wake dynamics [73] [74], drag reduction [71], etc. Curve fitting of the extensive experimental data leads to empirical correlations between cylinder Reynolds number with various flow parameters including vortex shedding Strouhal number St, root-mean-square(RMS) of sectional lift coefficient C_l and spanwise correlation factor [75].

Hot-wire and particle image velocimetry(PIV) are the most popular cylinder flow measuring techniques. Due to the periodic nature of the von Karman wake, statistical approaches including *phase-averaging*, *proper orthogonal decomposition(POD)* and *ensemble averaging* are used to decompose the flow field into mean, period and stochastic components. The phase-averaging technique is adopted in our study to distinguish the energy of periodic motions apart from turbulent fluctuations [76], the pressure signal in cylinder near-wake is used as reference data for the Hilbert transform technique to determine the phase angle of band-limited velocity signals [77].

The 3D nature of turbulent flow causes phase shift in the spanwise direction, which accelerates the flow structure break-down and turbulent energy cascading [72]. By correlating the passage of vortex and boundary layer velocity fluctuations on a downstream flat-plate, the relation between the vorticity and flat-plate boundary layer dynamics, which includes the formation of secondary flow structure and transition onset, was revealed [73].

The study on the effect of cylinder wake on downstream airfoil is of particular interest for our research. The highly turbulent wake of the cylinder induces transition on airfoil and postpone separation on airfoil. Studies found that the attached boundary layer further reduces the vorticity magnitude in the airfoil wake, which improves its aerodynamic characteristics [71].

2.8 Conclusions and Summary

As the wind energy industry develops, the scale of the wind plant and the size of single wind turbine grows. Better aerodynamic and structural design significantly increases the energy production and reduces maintenance cost. Both experimental and numerical studies were conducted in various levels, from wind-plant scale to turbine blade boundary layers. The costs of the full-scale tests are still prohibitively high and researchers thus have to compromise between accuracy and efficiency.

The current numerical approaches target either the macro-scale studies using low-fidelity models or the micro-scale studies using high-fidelity boundary-layer-resolved methods. Researches found that the hybrid turbulence models improves the prediction accuracy while keeps the computational cost relatively manageable and the transition on turbine blade has significant effects on its aerodynamic characteristics. This study attempts to integrate transition formulation into the hybrid model framework to further investigate the combined benefits to the unsteady wake and boundary layer predictions.

Chapter 3

Research Methods

This chapter introduces the numerical and experimental research approaches adopted in this study, including CFD tools, detailed turbulence model formulations, high-performance computing and particle image velocimetry.

3.1 CFD Software and Solver Algorithms

All simulations in this study are conducted by open-source CFD code OpenFOAM. The GNU General Public License allows users to freely use and modify OpenFOAM source code, the modular design of the software makes the implementation of new turbulence models and solvers straightforward and intuitive. Details of OpenFOAM are introduced in Appendix A.

The incompressible unsteady flow problems are solved by the Pressure Implicit with Splitting of Operator(PISO) algorithm [78], which is based on the Semi-Implicit Method for Pressure Lined Equation(SIMPLE) algorithm [79]. Both algorithms consist of a *momentum predictor* step followed by one(SIMPLE) or more(PISO) *velocity correction* step(s). The PISO algorithm is at least $2nd$ order accurate with multiple *velocity correction* iterations. Details of both algorithms are given in Appendix B.

3.2 Turbulence Models

This section introduces the turbulence model used in the current study. The $k-\omega SST$ is used as the base model for transition and hybrid formulation, the final product is a four-equation turbulence model named as Transitional-k-ωSST-DDES.

3.2.1 $k-\omega$SST model formulation

The two-equation $k-\omega$SST model was firstly introduced in 1994 [80]. The original $k-\omega$ model [81] cannot correctly predict the asymptotic behavior of turbulence approaching the wall and the turbulence kinetic energy(TKE) and dissipation(ϵ) calculated from $k-\omega$ model does not agree with DNS data. Furthermore, the specific dissipation(ω) in boundary layer has strong dependence on the freestream value. In contrast, the $k-\epsilon$ model does not suffer from the above-mentioned issues, but it is inferior to $k-\omega$ model in logarithmic region in adverse pressure gradient flows and in compressible flows.

To take the advantages of both turbulence models, a blending formulation was introduced. The $k-\epsilon$ model is firstly transformed into $k-\omega$ form by the relation: $\epsilon = \beta^* k\omega$, where the constant $\beta^* = 0.09$ and k is the turbulent kinetic energy. Blending function F_1 is introduced to blend two turbulence models. The transformed $k-\epsilon$ model equations are multiplied by $(1-F_1)$ and the $k-\omega$ model equations are multiplied by F_1, and both are added together to form the new model. The value of F_1 equals to 1 in the viscous sublayer and logarithmic region($k-\omega$ mode) and gradually decrease to 0 in the wake region($k-\epsilon$ mode).

The definition of the eddy viscosity is further modified for the effects of turbulent Shear Stress Transportation(SST). The original formulation of $\nu_t = k/\omega$, which is the the ratio of TKE production to dissipation, is significantly over one in the adverse pressure gradient flows. The new formulation of ν_t (equation 3.8) eliminates this issue by introducing a second blending function F_2.

The complete model is given here [80]:

$$\begin{aligned} \frac{D\rho k}{Dt} &= \tau_{ij}\frac{\partial u_i}{\partial x_i} - \beta^* \rho\omega k + \frac{\partial}{\partial x_j}\left[(\mu + \sigma_k \mu_t)\frac{\partial k}{\partial x_j}\right] & (3.1) \\ \frac{D\rho\omega}{Dt} &= \frac{\gamma}{\nu_t}\tau_{ij}\frac{\partial u_i}{\partial x_j} - \beta\rho\omega^2 + \frac{\partial}{\partial x_j}\left[(\mu + \sigma_\omega \mu_t)\frac{\partial \omega}{\partial x_j}\right] + 2(1-F_1)\rho\sigma_{\omega 2}\frac{1}{\omega}\frac{\partial k}{\partial x_j}\frac{\partial \omega}{\partial x_j} & (3.2) \end{aligned}$$

The constants of $k-\omega SST$ model $\phi_{k-\omega SST}$ are the blending of the original $k-\omega$ [81] ϕ_1 and $k-\epsilon$ model ϕ_2 in the form of

$$\phi_{k-\omega SST} = F_1\phi_1 + (1 - F_1\phi_2) \tag{3.3}$$

The constants of $k-\omega$ model ϕ_1 are:

$$\sigma_{k1} = 0.85, \sigma_{\omega 1} = 0.5, \beta_1 = 0.0750$$

$$\beta^* = 0.09, \kappa = 0.41, \gamma_1 = \beta_1/\beta^* - \sigma_{\omega 1}\kappa^2/\sqrt{\beta^*}$$

The constants of $k-\epsilon$ model ϕ_2 are:

$$\sigma_{k2} = 1.0, \sigma_{\omega 2} = 0.856, \beta_2 = 0.0828$$

$$\beta^* = 0.09, \kappa = 0.41, \gamma_2 = \beta_2/\beta^* - \sigma_{\omega 2}\kappa^2/\sqrt{\beta^*}$$

The stress tensor τ_{ij} is given by

$$\tau_{ij} = \mu_t\left(\frac{\partial u_i}{\partial x_j} + \frac{\partial u_j}{\partial x_i} - \frac{2}{3}\frac{\partial u_k}{\partial x_k}\delta_{ij}\right) - \frac{2}{3}\rho k \sigma_{ij} \tag{3.4}$$

The blending function F_1 is defined as

$$\begin{aligned} F_1 &= \tanh(arg_1^4) & (3.5) \\ arg_1 &= \min\left[\max\left(\frac{\sqrt{k}}{0.09\omega y}; \frac{500\nu}{y^2\omega}\right); \frac{4\rho\sigma_{\omega 2}k}{CD_{k\omega}y^2}\right] & (3.6) \end{aligned}$$

y is the distance to the nearest wall, and the cross-diffusion term $CD_{k\omega}$ is

$$CD_{k\omega} = \max\left(2\rho\sigma_{\omega 2}\frac{1}{\omega}\frac{\partial k}{\partial x_j}\frac{\partial \omega}{\partial x_j}, 10^{-20}\right) \tag{3.7}$$

For the Shear-Stress Transport(SST) formulation, the eddy viscosity is defined as

$$\nu_t = \frac{a_1 k}{\max(a_1\omega; \Omega F_2)} \tag{3.8}$$

where Ω is the magnitude of the vorticity. The second blending function F_2 is give by

$$\begin{aligned} F_2 &= \tanh(arg_2^2) && (3.9) \\ arg_2 &= max\left(2\frac{\sqrt{k}}{0.09\omega y}; \frac{500\nu}{y^2\omega}\right) && (3.10) \end{aligned}$$

3.2.2 Two-equation correlation-based transition model

A correlation-based two equation transition model using local variables are adopted in the current study. The use of the local variables avoids global operations, which introduce excessive communications among computing nodes in large-scale parallel simulations. The empirical correlations are adopted to link the local variables with the transition criteria, thus the whole formulation does not model the transition physics but rather provides a framework for the implementation of correlation-based model.

The transition mode used in this study consists of two transport equations, one for the turbulence intermittency field γ and another for transition momentum thickness Reynolds number $\tilde{Re}_{\theta t}$. The turbulence intermittency field γ is used to restrict TKE production and $\tilde{Re}_{\theta t}$ is solved for calculating the transition onset criteria [9]. Those criteria are used to calculate the transition length and transition onset location, which triggers the production term in γ transport equation, through empirical correlations.

The turbulence intermittency equation is as follows [82]:

$$\frac{\partial(\rho\gamma)}{\partial t} + \frac{\partial(\rho U_j \gamma)}{\partial x_j} = P_\gamma - E_\gamma + \frac{\partial}{\partial x_j}\left[\left(\mu + \frac{\mu_t}{\sigma_f}\right)\frac{\partial\gamma}{\partial x_j}\right] \tag{3.11}$$

The transition source P_γ is the given as:

$$P_\gamma = F_{length} c_{a1} \rho S [\gamma F_{onset}]^{0.5} (1 - c_{e1}\gamma) \tag{3.12}$$

P_γ is proportional to the strain rate S and the length of the transition region, which is given by empirical correlation F_{length}. Function F_{onset} controls the transition onset criteria, which is the major difference between all intermittency based transition formulations.

The vorticity Reynolds number is defined as:

$$Re_V = \frac{\rho y^2 S}{\mu} \tag{3.13}$$

where y is the distance to the nearest wall. There exists a universal transition correlation between the maximum vorticity Reynolds number inside boundary layer with the momentum thickness Reynolds number for moderate pressure gradient (shape factor $2.3 < H < 2.9$):

$$Re_\theta = \frac{Re_{Vmax}}{2.193} \tag{3.14}$$

Function F_{onset} is given as follows:

$$\begin{aligned} F_{onset1} &= \frac{Re_V}{2.193 Re_{\theta c}} && (3.15)\\ F_{onset2} &= \min[\max(F_{onset1}, F_{onset1}^4), 2.0] && (3.16)\\ R_T &= \frac{\rho k}{\mu \omega} && (3.17)\\ F_{onset3} &= \max\left[1 - \left(\frac{R_T}{2.5}\right)^3, 0\right] && (3.18)\\ F_{onset} &= \max(F_{onset2} - F_{onset3}, 0) && (3.19) \end{aligned}$$

From the relationship of Re_V and Re_θ in equation 3.14, F_{onset1} remains less than 1 in the moderate pressure gradient regions and slowly rise beyond 1 in strong pressure gradient regions. As the definition of F_{onset2} suggests, the value of F_{onset2} varies in the range of $0 (Re_V = 0)$ to $2 (F_{onset1} \geq 1.19)$. R_T is the ratio between turbulence eddy viscosity k/ω to kinematic viscosity ν, it is a measure of local turbulence strength. F_{onset3} varies in the range of $0 (\nu_t \geq 2.5\nu)$ to 1(laminar), the function F_{onset} reaches maximum at regions with significant turbulence energy and $F_{onset} > 0$ in the strong pressure gradient regions even it is locally laminar.

F_{length} controls the transition region length, and is given by a empirical correlation [9] with momentum thickness Reynolds number $\tilde{Re}_{\theta t}$:

$$F_{length} = \begin{cases} 389.189 \cdot 10^{-1} + (-119.270 \cdot 10^{-4})\tilde{Re}_{\theta t} + (-132.567 \cdot 10^{-6})\tilde{Re}_{\theta t}^{2} & \tilde{Re}_{\theta t} < 400 \\ 263.404 + (-123.939 \cdot 10^{-2})\tilde{Re}_{\theta t} + (194.548 \cdot 10^{-5})\tilde{Re}_{\theta t}^{2} & \\ +(-101.695 \cdot 10^{-8})\tilde{Re}_{\theta t}^{3} & 400 \leq \tilde{Re}_{\theta t} < 596 \\ 0.5 - (\tilde{Re}_{\theta t} - 596.0) \cdot 3.0 \cdot 10^{-4} & 569 \leq \tilde{Re}_{\theta t} < 1200 \\ 0.3188 & 1200 \leq \tilde{Re}_{\theta t} \end{cases}$$

To eliminate unphysical sharp change of skin friction in viscous sublayer F_{length} is forced to be equal to its maximum value in viscous sublayer

$$F_{sublayer} = e^{-(R_\omega/0.4)^2} \tag{3.20}$$

$$R_\omega = \frac{\rho y^2 \omega}{500\mu} \tag{3.21}$$

$$F_{length} = F_{length}(1 - F_{sublayer}) + 40.0 \cdot F_{sublayer} \tag{3.22}$$

The critical momentum thickness Reynolds number $Re_{\theta c}$ which marks the beginning of transition region is derived through correlation with $\tilde{Re}_{\theta t}$ [9]:

$$Re_{\theta c} = \begin{cases} \tilde{Re}_{\theta t} - (396.035 \cdot 10^{-2} + (-120.656 \cdot 10^{-4})\tilde{Re}_{\theta t} + (868.230 \cdot 10^{-6})\tilde{Re}_{\theta t}^{2} & \\ +(-696.506 \cdot 10^{-9})\tilde{Re}_{\theta t}^{3} + (174.105 \cdot 10^{-12})\tilde{Re}_{\theta t}^{4}) & \tilde{Re}_{\theta t} \leq 1870 \\ \tilde{Re}_{\theta t} - (593.11 + (\tilde{Re}_{\theta t} - 1870.0) \cdot 0.482) & \tilde{Re}_{\theta t} > 1870 \end{cases}$$

The destruction term E_γ is defined as

$$E_\gamma = c_{a2}\rho\Omega\gamma F_{turb}(c_{e2}\gamma - 1) \tag{3.23}$$

Ω is the magnitude of vorticity. Term F_{turb} is used to disable the destruction term outside laminar boundary layer or viscous sublayer:

$$F_{turb} = e^{-(R_T/4)^4} \tag{3.24}$$

Close to the wall, the viscosity ratio parameter $R_T = \rho k/\mu\omega = \nu_t/\nu$ decreases towards 0 and the destruction term E_γ dominates, the behavior of turbulence intermittency field is thus well-posed in the limit of approaching wall.

A list of the constant for the intermittency equation are

$$c_{e1} = 1.0; \quad c_{a1} = 2.0; \quad c_{e2} = 50; \quad c_{a2} = 0.06; \quad \sigma_f = 1.0$$

In the case of separation, the local intermittency value over 1 to accelerate transition

$$\gamma_{sep} = \min\left(s_1 \max\left[0, \left(\frac{Re_V}{3.235 Re_{\theta c}}\right) - 1\right] F_{reattach}, 2\right) F_{\theta t} \tag{3.25}$$

and

$$\begin{aligned} F_{reattach} &= e^{-(R_T/20)^4} &(3.26)\\ s_1 &= 2 &(3.27)\end{aligned}$$

The *effective* intermittency is thus defined as

$$\gamma_{eff} = \max(\gamma, \gamma_{sep}) \tag{3.28}$$

The transport equation for the transition momentum thickness Reynolds number $\tilde{Re}_{\theta t}$ is

$$\frac{\partial(\rho \tilde{Re}_{\theta t})}{\partial t} + \frac{\partial(\rho U_j \tilde{Re}_{\theta t})}{\partial x_j} = P_{\theta t} + \frac{\partial}{\partial x_j}\left[\sigma_{\theta t}(\mu + \mu_t)\frac{\partial \tilde{Re}_{\theta t}}{\partial x_j}\right] \tag{3.29}$$

The source term is defined as

$$\begin{aligned} P_{\theta t} &= c_{\theta t}\frac{\rho}{t}(Re_{\theta t} - \tilde{Re}_{\theta t})(1.0 - F_{\theta t}) &(3.30)\\ t &= \frac{500\mu}{\rho U^2} &(3.31)\\ F_{\theta t} &= \min\left(\max\left(F_{wake}\cdot e^{-(y/\delta)^4}, 1.0 - \left(\frac{\gamma - 1/c_{e2}}{1.0 - 1/c_{e2}}\right)^2\right), 1.0\right) &(3.32)\\ F_{wake} &= e^{(-Re_\omega/1e5)^2}, Re_\omega = \frac{\rho\omega y^2}{\mu} &(3.33)\end{aligned}$$

$P_{\theta t}$ is designed to force $\tilde{Re}_{\theta t}$ matching local $Re_{\theta t}$ calculated from empirical correlation. The blending function $F_{\theta t} = 0$ in the freestream and 1 in the boundary layer, thus the source term is off inside boundary layer and allows the transported $\tilde{Re}_{\theta t}$ to diffuse in from freestream.

The constants in $\tilde{Re}_{\theta t}$ equation are

$$c_{\theta t} = 0.03, \quad \sigma_{\theta t} = 2.0$$

The empirical correlation that relates the pressure gradient parameter λ_θ and K:

$$\lambda_\theta = (\theta^2/\nu)dU/Ds \tag{3.34}$$

$$K = (\nu/U^2)dU/ds \tag{3.35}$$

dU/ds is the acceleration along the streamwise direction and the momentum boundary layer thickness θ is calculated from

$$\theta = \frac{\tilde{Re}_{\theta t}\mu}{\rho U} \tag{3.36}$$

The empirical correlation is defined as [9]

$$Re_{\theta t} = 803.73[Tu + 0.6067]^{-1.027}F(\lambda_\theta, K) \tag{3.37}$$

Function $F(\lambda_\theta, K)$ is defined as [9]

$$F(\lambda_\theta, K) = 1 - [-10.32\lambda_\theta - 89.47\lambda_\theta^2 - 265.51\lambda_\theta^3]e^{[-Tu/3.0]}, \lambda_\theta \leq 0 \tag{3.38}$$

$$F(\lambda_\theta, K) = 1 + [0.0962[K10^6] + 0.148[K10^6]^2 + 0.0141[K10^6]^3] \tag{3.39}$$

$$\times \quad (1 - e^{[-Tu/1.5]}) + 0.556[1 - e^{[-23.9\lambda_\theta]}]e^{[-Tu/1.5]}, \lambda_\theta > 0 \tag{3.40}$$

3.2.3 $k-\omega$SST-based Delayed Detached-Eddy Simulation(DDES)

The Delayed Detached-Eddy Simulation approach was introduced by Spalart et al. [83]. The new formulation overcomes the major issues in original DES [84]. The DDES formulation uses a blending function f_d [85]:

$$f_d \equiv 1 - \tanh([20r_d]^3) \tag{3.41}$$

$$r_d \equiv \frac{\nu_t + \nu}{\sqrt{U_{i,j}U_{ij}}\kappa^2 d^2} \tag{3.42}$$

d is the distance to the nearest wall. The function r_d equals to 1 in log layers and decreases to 0 towards the edge of boundary layer, thus f_d remains to 0 inside boundary layer and gradually increases to 1 in the LES region, where $r_d << 1$. The constant inside tanh function controls the position of the model switch, larger value delays the LES, value of 20 is calibrated for $k - \omega SST$ model [85], the original value that was proposed for SA model is 8 [83].

The new hybrid length scale L_H is a blend of RANS L_R and LES length scale L_L, viz.

$$L_H \equiv L_R - f_d \max(0, d - L_L) \tag{3.43}$$

Here, $L_L = C_{DES}\Delta$, where the constant $C_{DES} = 0.65$ and $\Delta = \max(L_x, L_y, L_z)$, i.e. the maximum dimension of the local grid, which is the smallest scale that can be resolved by the current mesh.

3.2.4 Transitional-$k - \omega$SST-DDES model formulations

The incompressible version of $k - \omega SST$ model is

$$\frac{Dk}{Dt} = \frac{\tau_{ij}}{\rho}\frac{\partial u_i}{\partial x_i} - \beta^* \omega k + \frac{\partial}{\partial x_j}\left[(\nu + \sigma_k \nu_t)\frac{\partial k}{\partial x_j}\right] \tag{3.44}$$

$$\frac{D\omega}{Dt} = \frac{\gamma}{\mu_t}\tau_{ij}\frac{\partial u_i}{\partial x_j} - \beta\omega^2 + \frac{\partial}{\partial x_j}\left[(\nu + \sigma_\omega \nu_t)\frac{\partial \omega}{\partial x_j}\right] + 2(1 - F_1)\sigma_{\omega 2}\frac{1}{\omega}\frac{\partial k}{\partial x_j}\frac{\partial \omega}{\partial x_j} \tag{3.45}$$

The production and destruction terms in TKE equation are denoted as

$$P_k = \frac{\tau_{ij}}{\rho}\frac{\partial u_i}{\partial x_i} \tag{3.46}$$

$$D_k = \beta^* \omega k \tag{3.47}$$

The RANS length scale in $k - \omega SST$ model is given as $L_R = \sqrt{k}/(\beta^* \omega)$, thus we can write the dissipation term in TKE equation in terms of L_R, viz.

$$D_k = \beta^* \omega k = \frac{k^{3/2}}{L_R} \tag{3.48}$$

L_R is replaced by L_H in DDES formulation, viz.

$$D'_k = \frac{k^{3/2}}{L_H} \tag{3.49}$$

The transition model is integrated by introducing the effective intermittency field (equation 3.28) into the production and the new destruction term D'_k:

$$\tilde{P}_k = \gamma_{eff} P_k \tag{3.50}$$

$$\tilde{D}_k = \min(\max(\gamma_{eff}, 0.1), 1.0) D_k \tag{3.51}$$

Since physical definition of turbulence intermittency is based on temporal statistics rather than just a weighting factor of TKE production that calculated by a separate transport equation, in order to avoid confusion, the intermittency filed γ will be explicitly referred to as Langtry Menter (LM) turbulence intermittency in the remaining of this study.

Implementation in OpenFOAM

The implementation of each term in OpenFOAM follows the above definitions, *min* and *max* functions are used to avoid numerical issues, e.g. divide by zero. In order to maintain prescribed inlet turbulent energy, a weak source term is added to turbulence equations [86] viz.

$$\beta^* \omega_{amb} k_{amb} \tag{3.52}$$

in k equation and

$$\beta \omega_{amb}^2 \tag{3.53}$$

in ω equation. The k_{amb} and ω_{amb} are the ambient value as prescribed in domain inlet. Inside boundary layer, the production of both turbulence fields far exceed the ambient value thus the extra source term can be neglected.

3.3 High-Performance Computing

The High-Performance Computing(HPC) is supported by Virginia Tech Advanced Research Computing(ARC) center. This section introduces the parallel computing architecture, flow visualization and data analysis approaches used in this study.

3.3.1 Parallel computing

The main simulations were run on ARC's latest cluster *Cascades*, which is 196-node system with Intel® Broadwell processors. Each node is equipped with two 16-core processors and 128 GB of memory, the cluster's normal queue allows up to 36,884 core-hours per user, which makes it suitable for large computations (e.g. OpenFOAM) using MPI.

OpenFOAM runs parallel computations on distributed processors through Message Passing Interface(MPI), which is a communication protocol that provides highly-scalable parallel computing. The computation domain is decomposed for even loading on every processor, the communication across boundaries of adjacent subdomains are achieved via point-to-point basics. MPI also provides collective communications among all processes for global operations. It is thus important to balance the computation load and communication overhead for each processor, as a rule-of-thumb, a minimum of 30,000 cells/processor is recommended.

The full-model mesh consists around 10 million cells and was decomposed into 320 subdomains. Approximately 320,000 core-hours are required for 1 second of simulation time.

3.3.2 Visualization

The flow visualization is powered by Fieldview®. The data processing and image rendering are accelerated through reverse SSH connection from local client to parallel Fieldview server running on remote cluster. The maximum number of server processes are fixed to 8 due to license limitation.

Chapter 4

Problem Formulation and CFD-Based Experimental Design

The full-scale wind plant aerodynamics covers a vast range of length and time scales, from microns to hundreds of meters, and milliseconds to minutes respectively (Table 4.1). The full-scale problem is too complicated and computationally expensive for fundamental model development and VVUQ (verification, validation, and uncertainty quantification). For example, studies of a full-scale single rotating blade in atmosphere with well-resolved boundary layer requires over 50 million cells and thousands of processors, and each time-step of data requires over 20GB of storage [3]. Therefore, we are motivated to develop a surrogate model problem.

Table 4.1: Range of scales and modeling techniques for full-scale wind turbines

Time scale	Length scale	Blade Re	Reduced frequency	Modeling technique
$\sim O(10^{-3}s - 10^{1}s)$	$\sim O(10^{-6}m - 10^{2}m)$	$\sim O(10^{7})$	$\sim O(10^{-2} - 10^{0})$	CFD, actuator methods, BEM

4.1 Model Problem Design

An overview of the experimental and numerical contributions is shown in figure 4.1. The flow chart is consisted of red blocks for numerical work, blue blocks for experimental work and black blocks for joint efforts. All the experiments and corresponding analysis were conducted by Daniel R. Cadel and the details can be found in his thesis [76].

The current study adopts a complementary CFD/EFD approach and preliminary CFD data was used to guide the experimental design. The data from experiments was used for turbulence model validation purpose and the final product is a new turbulence model for general use. The comparison and analysis of numerical and experimental data led to the fully-described flow physics of the unsteady boundary layer.

The experiments were conducted in a 28-inch-wide wind-tunnel test section, the surrogate model in our study consists of a modified 6-series airfoil [87] (figure 4.2) embedded in the wake of a circular cylinder, which is used as the surrogate atmospheric turbulence generator. Figure 4.3 is the sketch of experiment setup in the test section, the freestream velocity is at $U_\infty = 26m/s$ and turbulence intensity $Ti = 1\%$. The diameter of the circular cylinder $D = 1.5in.$ and airfoil chord length $c = 4in.$, which corresponds to $Re_D = 6.4 \times 10^4$ and $Re_c = 1.7 \times 10^5$.

The key parameter is the spacing L from cylinder center to airfoil leading edge, in order to minimize the direct effects on unsteady boundary layer physics from the upstream cylinder, the airfoil is placed outside the immediate wake of the cylinder. Various spacings from $1.5D$ up to $10D$ were test by potential flow solver in OpenFOAM and the pressure recovery curves are plotted from cylinder rear stagnation point to airfoil leading edge as shown in figure 4.4, as the airfoil moves further than $9D$ downstream the pressure recovers to near freestream level ($C_p = 0$) at $\sim 4D$. The furthest airfoil position is also limited by the experimental equipments, e.g. the total length of the test section and PIV camera blockage from test section supporting brackets, the spacing is finally fixed at $L = 16in.$, i.e. $10.67D$.

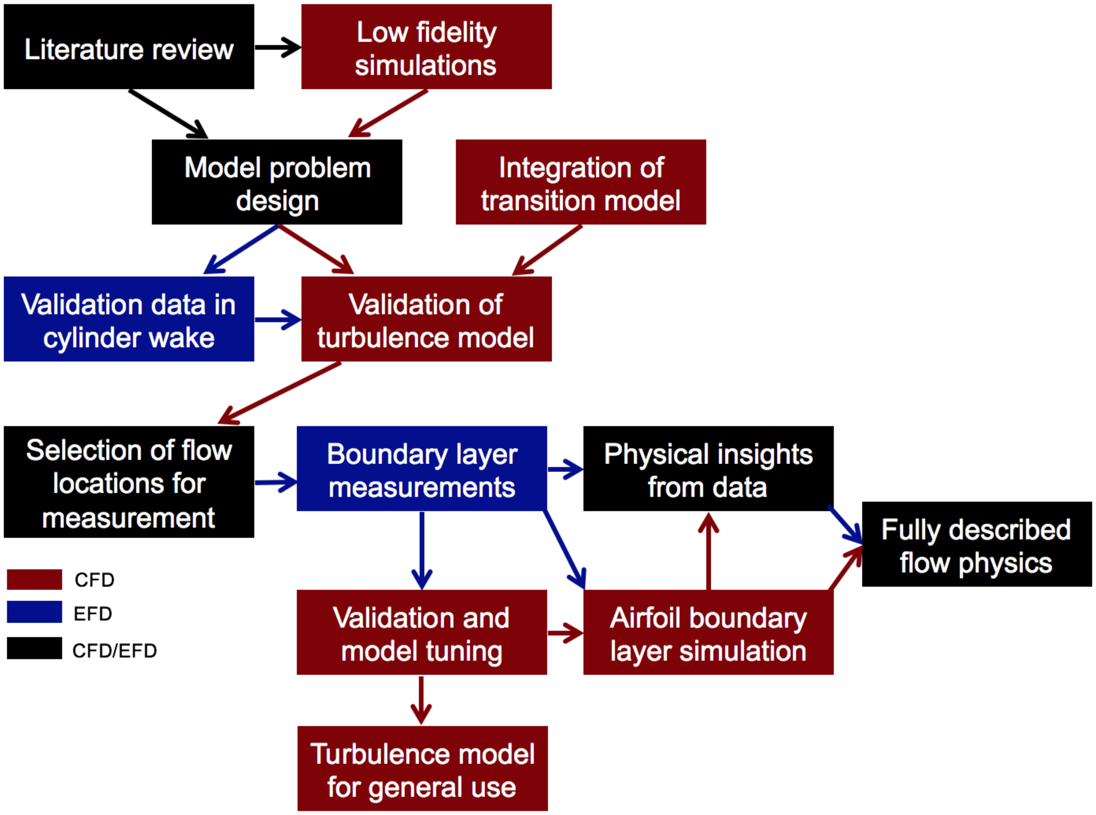

Figure 4.1: Overview of experimental and numerical contributions to the research. Experimental efforts in blue, numerical efforts in red and joint contributions in black

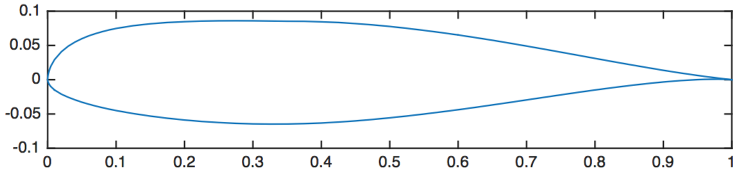

Figure 4.2: NACA63215b airfoil

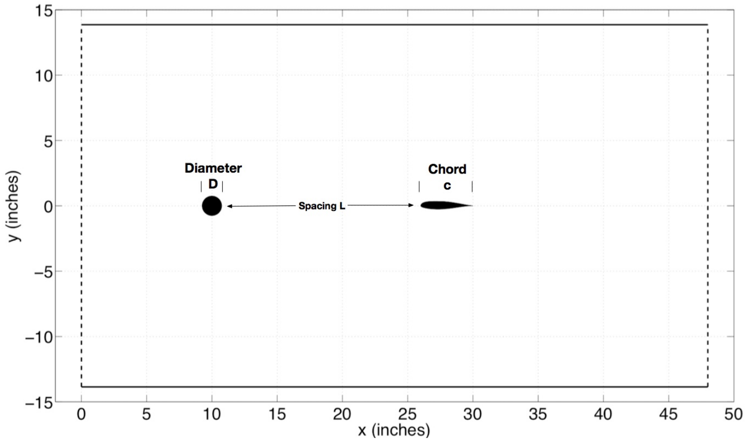

Figure 4.3: Diagram of 28-inch test section and experimental setup

A summary of the flow conditions and model parameters are presented in table 4.2.

Table 4.2: Test section flow conditions and surrogate model parameters

Freestream conditions	Test section dimensions	Circular cylinder	NACA63215b airfoil
$U_\infty = 26m/s$ $Ti = 1\%$	Streamwise(x): 48in. Transverse(y): 28in. Spanwise(z): 28in.	Diameter $D = 1.5in.$ $Re_D = 6.4 \times 10^4$ Aspect ratio $AR = 18.7$ Spacing $L = 10.7D$	Chord $c = 4in.$ $Re_c = 1.7 \times 10^5$ Aspect ratio $AR = 7$ Reduced frequency $k = 1.5$

4.2 Experimental Setups

The validation experiments were conducted in Virginia Tech's 0.7m blower type subsonic wind tunnel. The tunnel is powered by a 30hp BC-SW Size 365 Twin City centrifugal fan

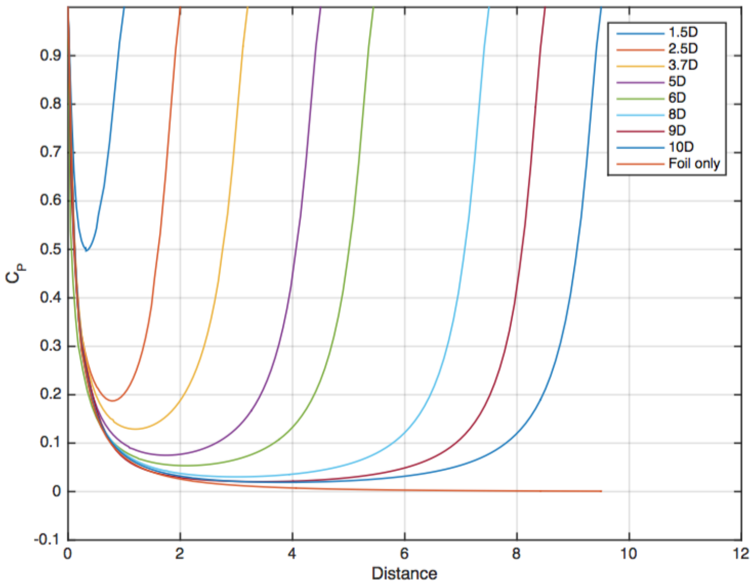

Figure 4.4: Pressure recovery along the centerline in cylinder wake

capable of up to $15m^3/s$ (figure 4.5).

The test section was enclosed by transparent acrylic walls with corner gussets (figure 4.6), the freestream velocity $U_\infty = 26m/s$ with turbulence intensity of 1%. The characterization measurements of tunnel freestream was conducted by Pitot probe, hot wire and flattened Pitot probe.

The stereoscopic Particle Image Velocimetry(PIV) systems in our experiments used two high-speed cameras under the test section (figure 4.8). The first PIV system operated at 2920 Hz and second system at 4 Hz. Due to low stereoscopic sensitivity of the spanwise component in the boundary layer measurements, only the in-plane velocity data was analyzed. PIV seed particles were introduced downstream of the tunnel fan in order to achieve uniform particle distribution at model position. Higher seed density was introduced upstream for the airfoil unsteady boundary layer measurements due to high magnification boundary layer planes. Owing to the limited spacial resolution, the uncertainty in PIV data is estimated at 1% of the velocity magnitude [76]. Both the airfoil and cylinder models were chrome-plated in order to mitigate laser flare during PIV testing (figure 4.7).

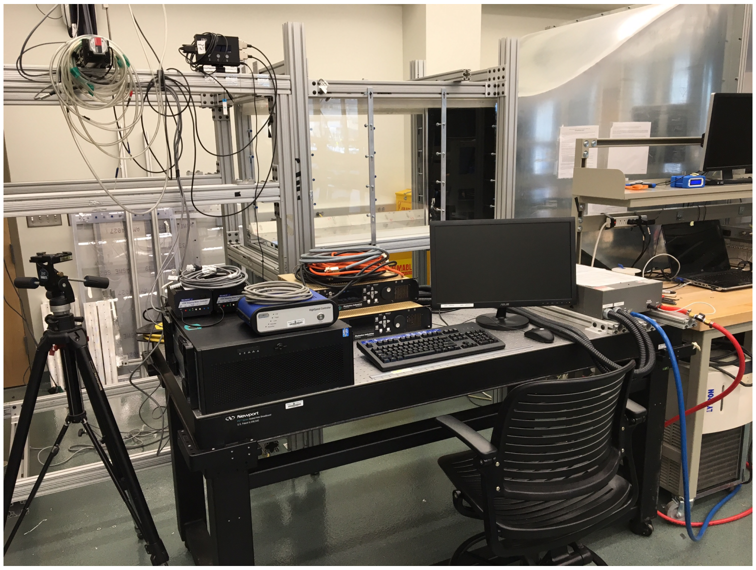

Figure 4.5: Low-speed wind tunnel and test section

Figure 4.6: Acrylic-wall enclosed test section with corner gussets

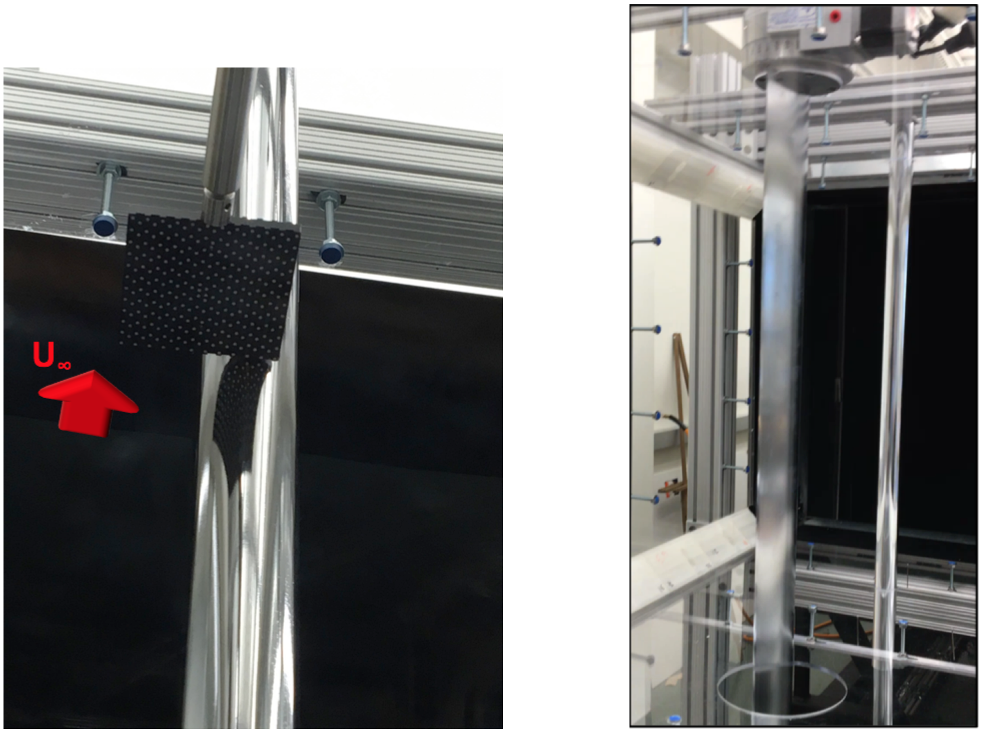

(a) Chrome-plated cylinder and PIV calibration plate

(b) Chrome-plated airfoil and circular cylinder

Figure 4.7: Circular and airfoil model in test section

The mean velocity components behind circular cylinder are shown in figure 4.9 and the recirculation zone is outlined by the the mean streamwise velocity distribution. Extra effort was devoted to three focal regions on airfoil suction side for optimized spatial resolution (figure 4.10).

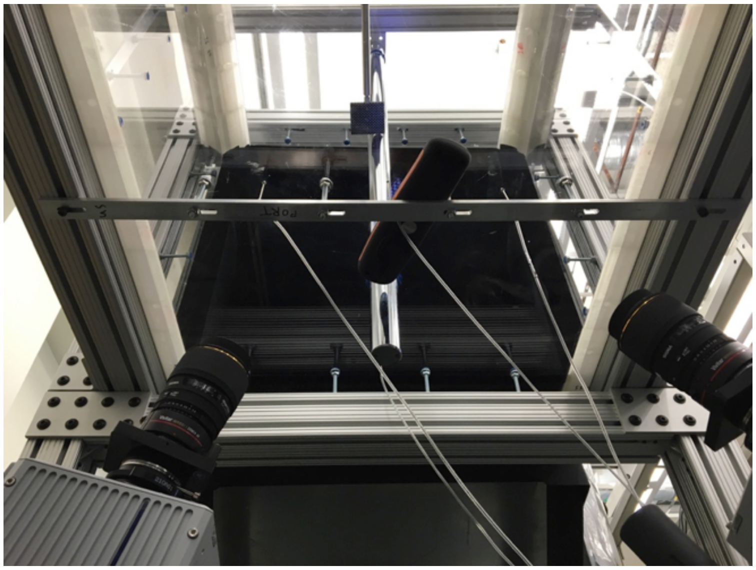

Figure 4.8: Camera setup of PIV system

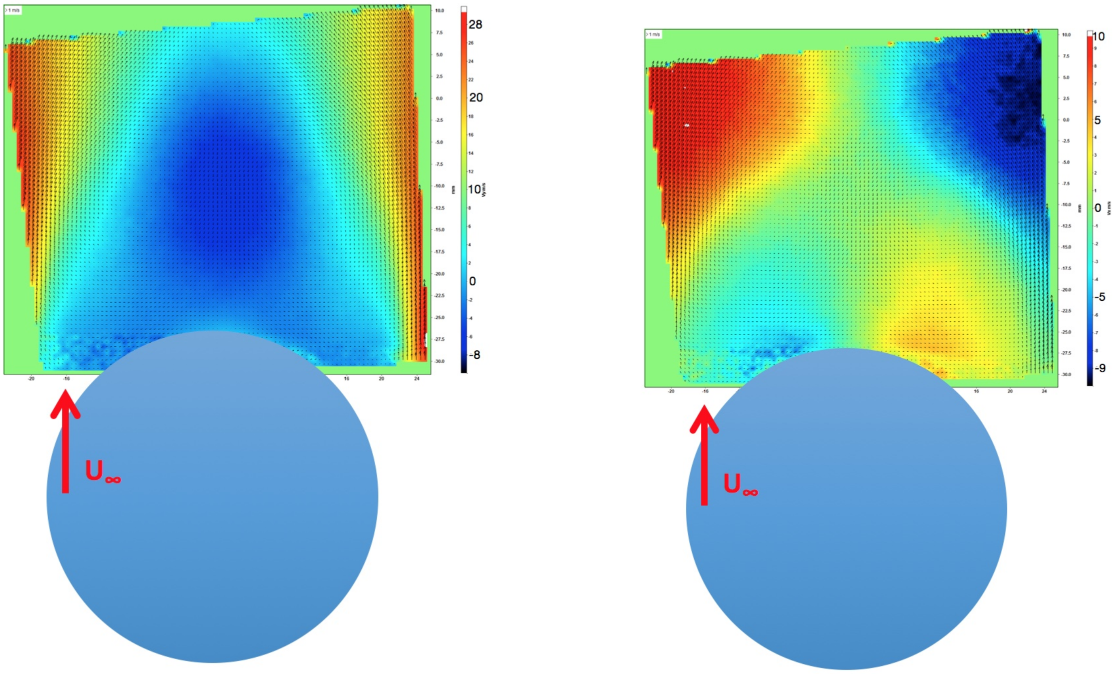

(a) Streamwise velocity

(b) Transverse velocity

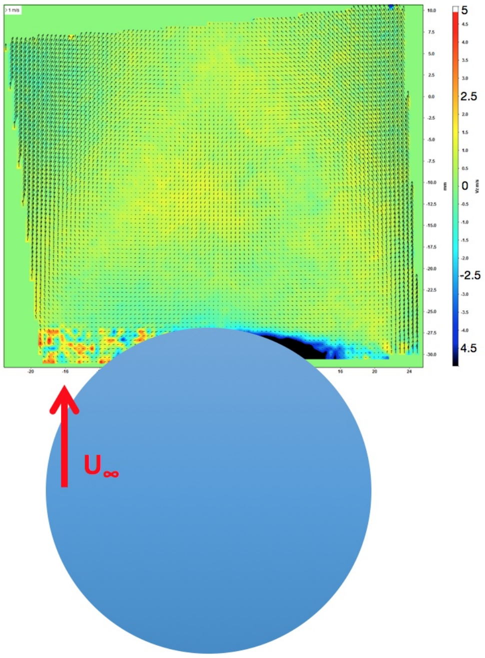

(c) Spanwise velocity

Figure 4.9: Velocity components in cylinder near-wake

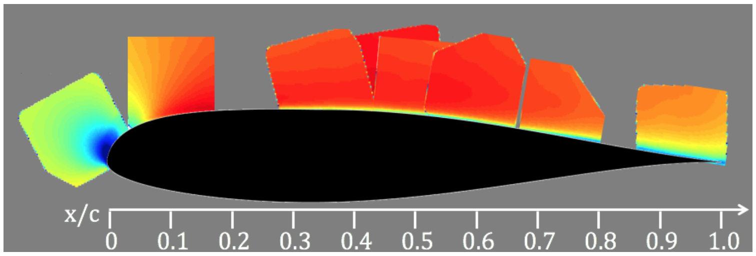

Figure 4.10: Focal regions on airfoil for optimized spatial resolution

Chapter 5

Verification and Validation of Transition Model Performance

The original $\gamma - \tilde{Re}_{\theta t}$ transition model was implemented in CFX-5, before applying the transition hybrid turbulence model to cylinder-airfoil simulation, the transition formulation integrated with $k-\omega$SST is tested on 2D flat-plate and wind turbine airfoil cases. With well-documented experimental data and numerical result by original implementation of $\gamma - \tilde{Re}_{\theta t}$ transition model, this section deals with the verification and validation of our implementation.

5.1 Problem Setup

This section introduces the flat-plate and S809 airfoil geometry and computation mesh together with the flow conditions and numerical schemes used in OpenFOAM.

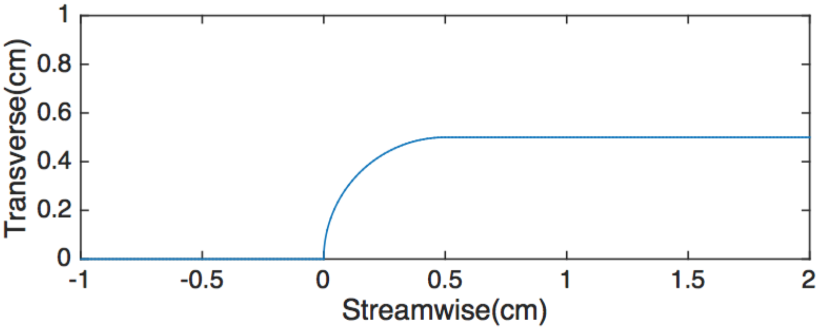

Figure 5.1: Flat-plate leading edge geometry

5.1.1 Model Geometry, Computation Mesh and Inflow Conditions

Flat-plate

The T3L series circular leading edge flat-plate([88]) is a widely-used case for validating transition model in different turbulence intensities. The circular leading edge is $1cm$ in diameter (figure 5.1) and the tangential flat-plate extends to 100 diameters downstream of the leading edge(figure 5.2).

The mesh was constructed according to the transition model grid requirements [89]. Numerical tests on T3L series flat-plate found the near-wall grid size was insensitive to y^+ value below 1 and the transition onset location starts to move upstream for y^+ over 8. The expansion factor of grid size in wall-normal direction should be kept below 1.1, same upstream shift of transition location also exists for large expansion factor.

In the current study, the wall normal mesh is refined to $y^+ \sim 1$ over the whole length and expansion ratio near flat-plate surface is fixed at 1.05. The total cells count of the 2D mesh is 73k. The freestream velocity is at $5m/s$ with turbulence intensity 0.63%, 2.06% and 5.34% in three cases T3LB, T3LC and T3LD respectively. The corresponding leading edge Reynolds number $Re_D = 3,300$.

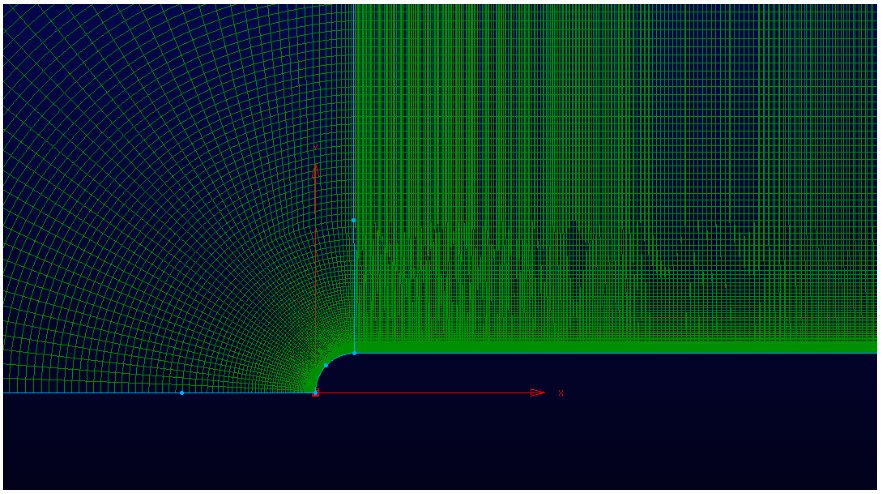

(a) Leading edge mesh

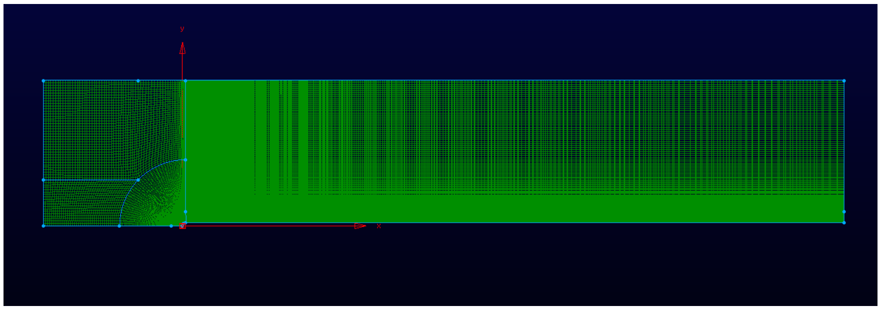

(b) Flow domain

Figure 5.2: Computational domain of flat-plate case

S809 airfoil

The S809 airfoil is originally designed by NREL ([90]) for horizontal-axis wind turbine. The thick design(21%) helps maintaining laminar flow on both surfaces at certain angle of attack range, as known as the laminar bucket, drag remains constant as lift increase. Outside the laminar bucket, the transition points move upstream rapidly, which is followed by steep increase of drag. A series of low-speed experiments were conducted in Delft University of Technology [91], detailed experimental data, including sectional lift and drag, pressure distribution and transition location were published.

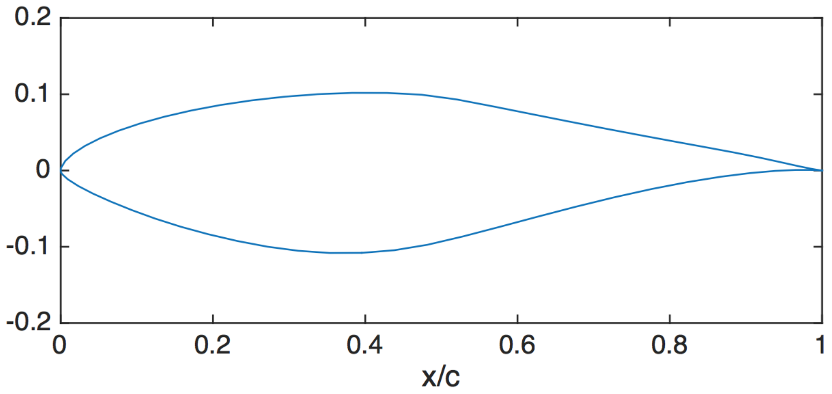

Figure 5.3: S809 airfoil profile

The S809 geometry is shown in figure 5.3. C-type mesh is constructed around the airfoil and expands $10c$ up&downstream of the airfoil (figure 5.4). The freestream velocity $U_\infty = 31.2m/s$, which corresponds to $Re_c = 2 \times 10^6$. The turbulence intensity around the airfoil is $\sim 0.2\%$. Mesh normal to airfoil surface is refined to $y^+ \sim 1$ as in the flat-plate case.

5.1.2 Numerical Schemes and Turbulence Model

Due to the cusped trailing edge of S809 and refined wall-normal mesh, simulations suffer from numerical instabilities in steady state simulation. The airfoil flow is solved by transient solver *pimpleFoam*, which is essentially PISO algorithm but with extra outer-iteration to increase solution stability especially in the case of large time-steps.

Time schemes

Both cases use implicit and bounded *CrankNicolson* 2^{nd} order time scheme with off-center parameter $\psi = 0.9$. $\psi = 1$ corresponds to pure CrankNicolsom and $\psi = 0$ is equivalent to 1^{st} order Euler scheme.

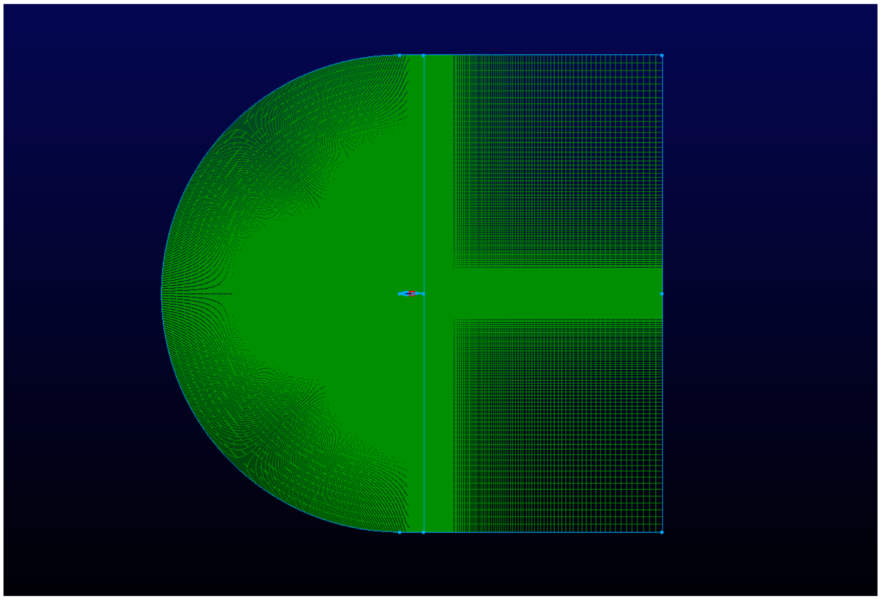

(a) Flow domain

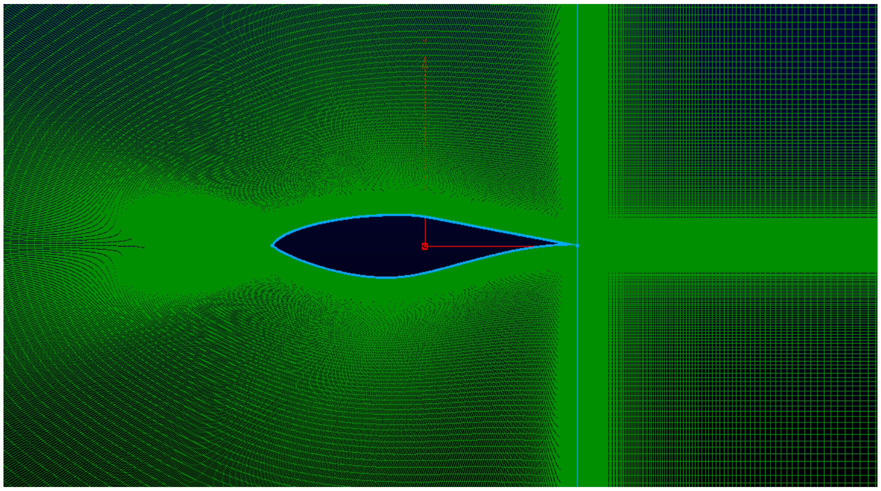

(b) Mesh around airfoil

Figure 5.4: Computational domain of S809 airfoil

Divergence schemes

The flat-plate case adopts *LUST* scheme, which is a hybrid scheme of linear(75%) and linear-upwind(25%). All S809 airfoil cases use 1^{st} order upwind scheme for better numerical stability.

Laplacian schemes

All Laplacian schemes use 2^{nd} order linear interpolation for the diffusion coefficient and *corrected* surface normal gradient scheme.

Turbulence model

All test cases used 2D mesh, the $k-\omega SST$ based model is integrated with transitional formulation and freestream turbulence energy sources terms to maintain the prescribed turbulence level from inlet to model position([39]).

5.2 Results and Analysis

All results in this section are compared with numerical data predicted by original model implementation ([92], [39]) and experimental results ([88], [90]).

5.2.1 Flat-plate Cases

The skin friction on circular leading edge flat-plate is given in figure 5.5. Laminar flow separates at 77° of the circular leading edge and forms a separation bubble, the separated flow reattaches to different locations on the flat portion of the plate depending on the free stream turbulence intensity. Table 5.1 lists the reattachment position on the flat-plate starting from the leading edge, as turbulence intensity increase from 0.63% in T3LB to 5.34% in T3LC the reattachment position move upstream from $5.6r$ to $3.1r$.

The streamwise velocity and LM intermittency distribution in figure 5.6 shows the range of the separation bubble and flow transition on the flat-plate. The separated flow attaches at the locations where the LM intermittency reaches value 1 on the flat-plate surface. In low turbulence intensity cases, there is a region at the outer boundary layer where the LM intermittency is approximately 0.5, it is an artifact from laminar separation upstream. As turbulent boundary layer grows, this region soon disappear downstream.

The laminar and fully-turbulent flow skin friction from Blasius theory and Schultz-Grunow correlation is plotted in figure 5.5 for reference, the skin friction of transitional flow sits between the two limits. Examine the turbulence intermittency field in figure 5.6, the boundary layer is turbulent near the reattachment point ($\gamma \sim 1$) and the reattached flow downstream is transitional ($\gamma \sim 0.5$). While in experiments, the boundary layer flow experiences gradual transition from laminar to turbulent and the skin friction rises monotonically over the reattachment location. Compared with the experimental data, both Langtry's prediction and current simulation data over-predicts skin friction right after reattachment, and gradually converges to experimental result downstream.

Table 5.1: Reattachment positions on flat plate (r is the leading edge radius)

	T3LB	T3LC	T3LD
Ti	0.63%	2.06%	5.34%
Reattach	$2.8cm(5.6r)$	$2.2cm(4.4r)$	$1.6cm(3.1r)$

5.2.2 S809 airfoil Cases

The S809 airfoil is tested at $AoA = 1^\circ$ and $AoA = 9^\circ$. Figure 5.7 shows the pressure distribution from the simulation results of current implementation, Langtry's implementation [39] and experimental data [90]. The laminar separation, transition and reattachment points are marked out in the case of $AoA = 1^\circ$, the chordwise location from all three sources collapse within 5% of the chord length. In the case of $AoA = 9^\circ$, flow separated near leading edge on the suction side while the separation is further delayed downstream compared with the case of $AoA = 1^\circ$.

The pressure distribution from present results shows oscillation on suction side near $x/c = 0.05$, while the airfoil geometry and surface discretization remains smooth. Inspecting the

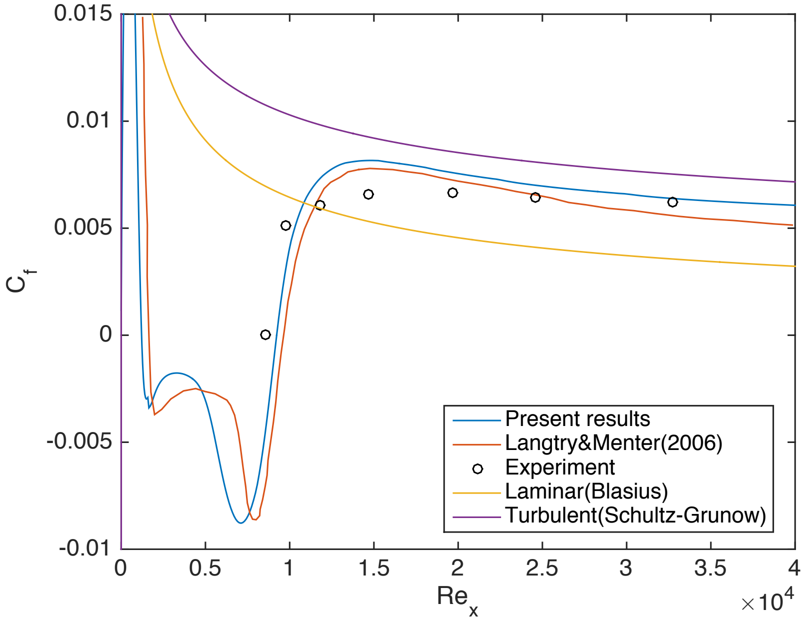

(a) T3LB, $Ti = 0.63\%$

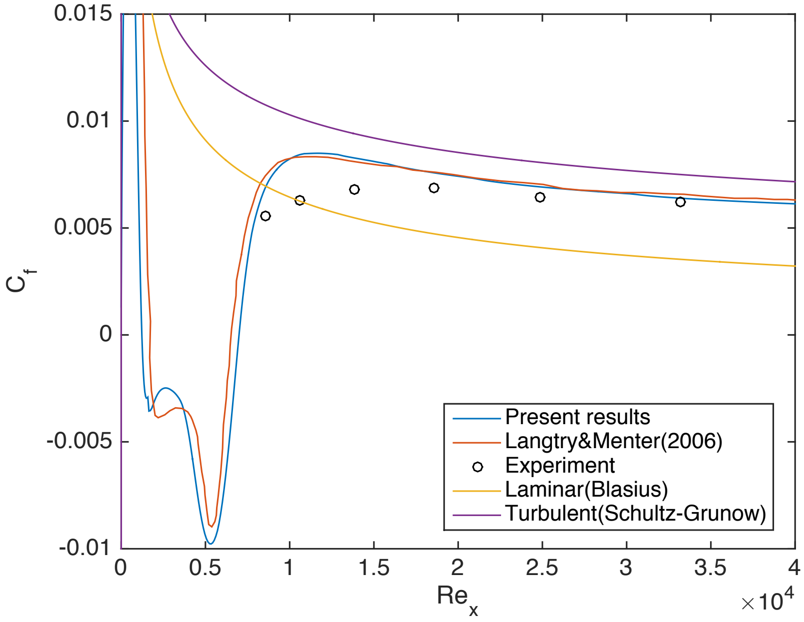

(b) T3LC, $Ti = 2.06\%$

Figure 5.5: Flat-plate skin friction

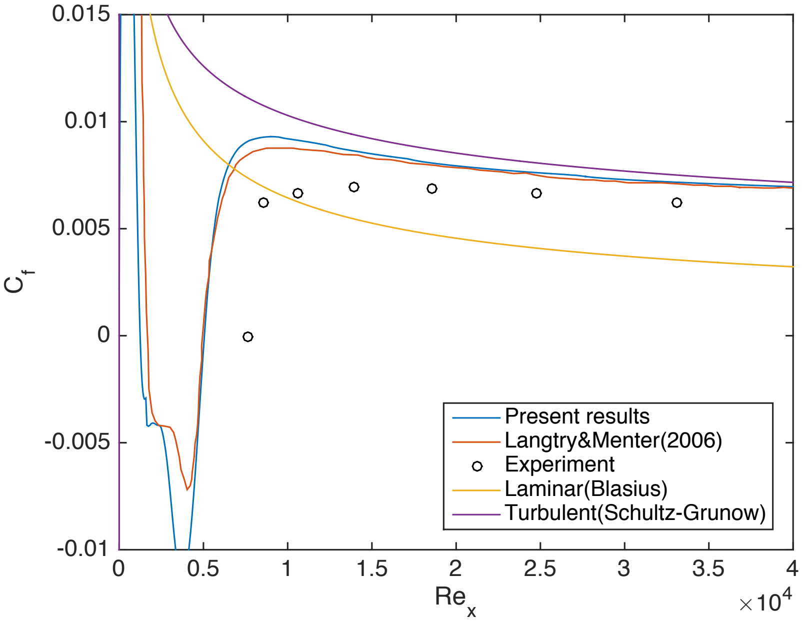

(c) T3LD, $Ti = 5.34\%$

Figure 5.5 (cont.): Flat-plate skin friction

turbulence intermittency field, the distribution of γ remains constant over this region. The cause of the oscillations in pressure field needs further investigation.

The transition locations and force coefficients are summarized in table 5.2. The drag coefficient matches across all three cases, owing to the accurate prediction of separation points and low skin friction by transition model. At $AoA = 1°$, the transition location of two CFD implementations agrees well with only 1% discrepancy on pressure side and both CFD results predict transition earlier than experiments. For $AoA = 9°$, transition on pressure side is precisely captured, while there is a relatively large error near leading edge on suction side where high adverse pressure gradient exists. It could be caused by 3D unsteadiness and wind tunnel blockage effects that is not present in 2D simulations. Transition location prediction of the $AoA = 9°$ case from the current implementation matches experimental data better than Langtry's data(table 5.2), which is also the case for the lift coefficient.

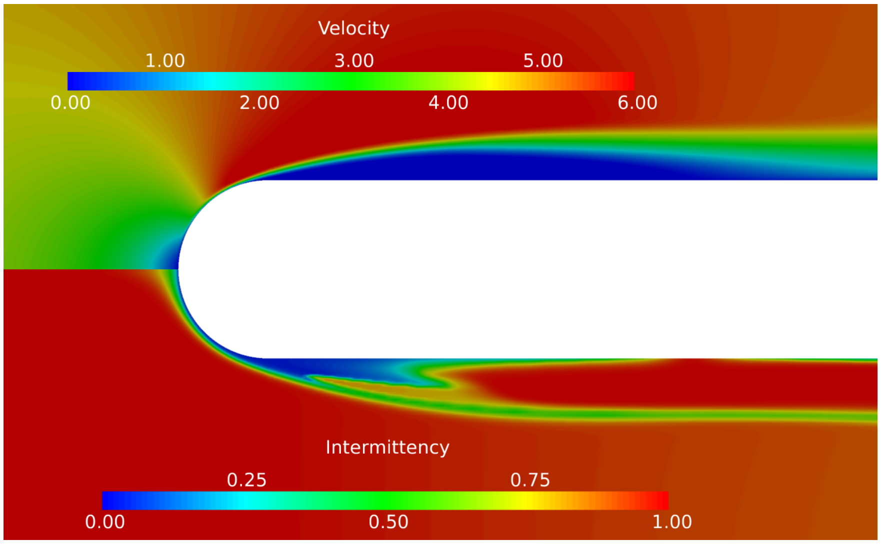

(a) T3LB, $Ti = 0.63\%$

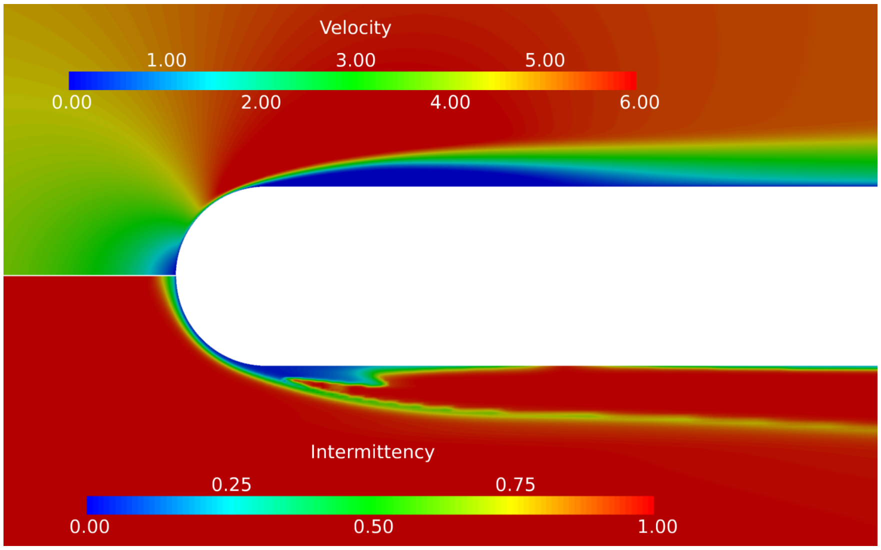

(b) T3LC, $TI = 2.06\%$

Figure 5.6: Flat-plate streamwise velocity and LM turbulence intermittency

5.3 Conclusions and Summary

Two benchmark problems were investigated to verify the implementation of the transition model in OpenFOAM and both were also validated against the experimental results. The transition model is sensitive to the freestream turbulence intensities in terms of the transi-

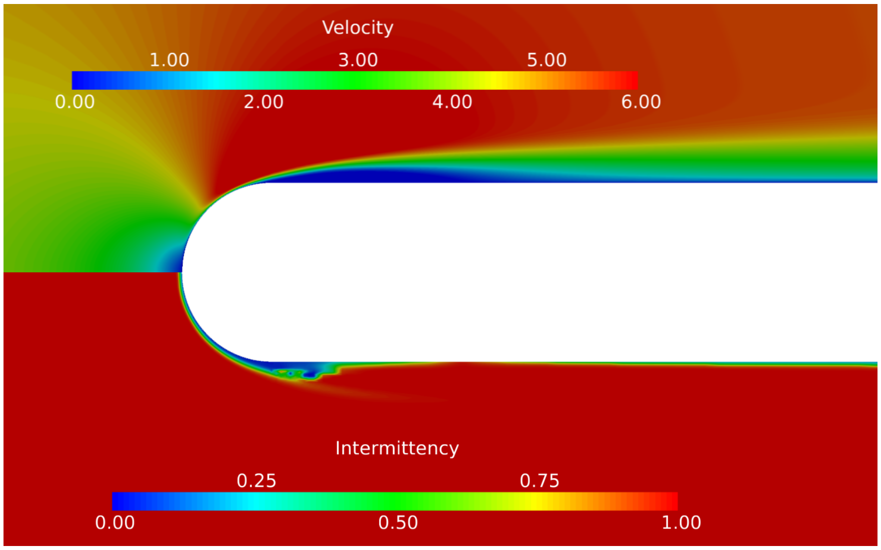

(c) T3LD, $Ti = 5.34\%$

Figure 5.6 (cont.): Flat-plate streamwise velocity and LM turbulence intermittency

tion location and skin friction which sits between the limits of laminar and fully-turbulent solutions. The skin friction from the current implementation match Langtry's data and both asymptotically approach experimental data downstream.

The S809 airfoil is a widely-adopted blade in wind energy industry, the 2D simulation result is compared with Langtry's data [39] and also the extensive experimental data by Somers [90]. Two angle-of-attack are tested at $Re_c = 2 \times 10^6$, the flow features laminar separation, transition and turbulent reattachment, which makes this case a comprehensive test of the transition model. It was found that at low AoA, where the flow separation and transition initiated at $\sim x/c = 0.5$, the transition model was very accurate at predicting the transition location and also aerodynamic forces acting on the airfoil. At higher AoA (9°), the discrepancy in transition location on suction side increases compared with the case of $AoA = 1°$.

In summary, the transition model in current implementation provides accurate transition prediction compared with original implementation and experimental data, it is thus integrated with hybrid formulation and further tested in circular cylinder flow.

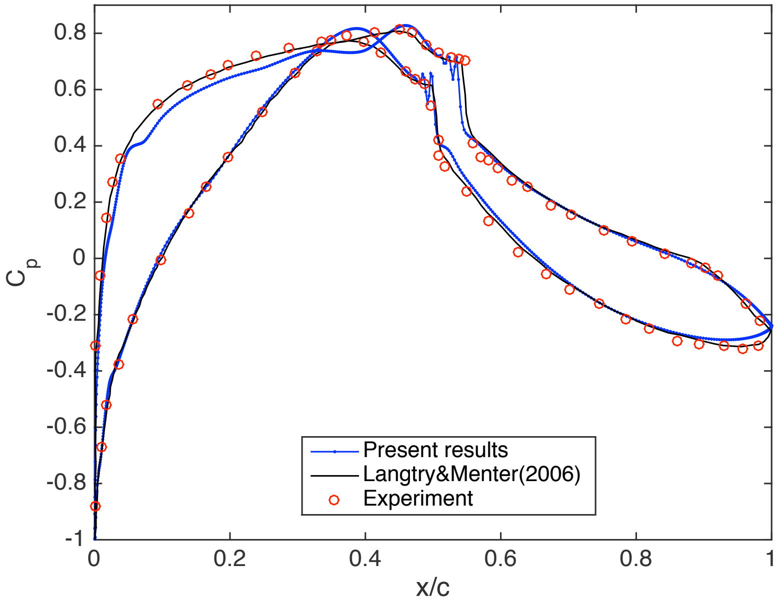

(a) $AoA = 1^\circ$

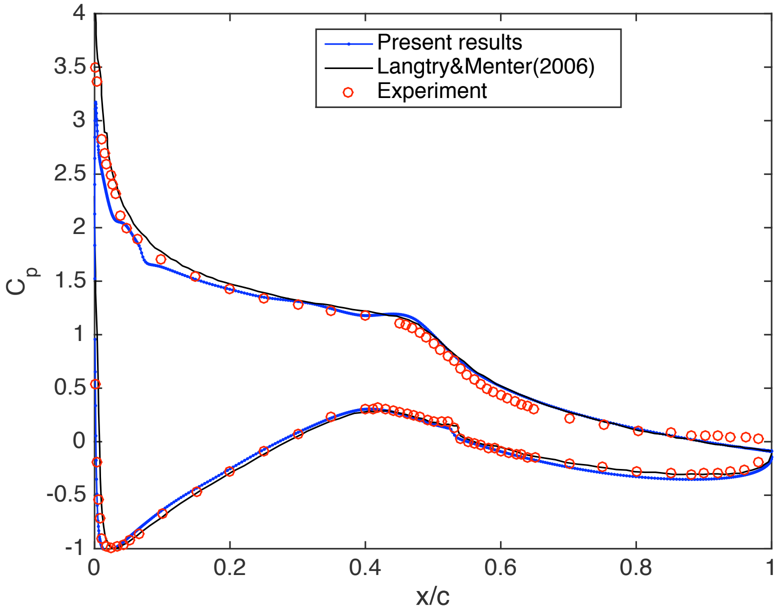

(b) $AoA = 9^\circ$

Figure 5.7: Pressure Distribution (C_p)

Table 5.2: Transition location and force coefficient of current implementation

		Suction side	Pressure side	C_d	C_l
$AoA = 1^\circ$	CFD(Zhang)	0.51	0.46	0.007	0.25
	CFD(Langtry) [39]	0.51	0.47	0.007	0.27
	Experiment [90]	0.56	0.50	0.007	0.27
$AoA = 9^\circ$	CFD(Zhang)	0.06	0.53	0.02	1.02
	CFD(Langtry) [39]	0.10	0.52	0.02	1.08
	Experiment [90]	0.03	0.53	0.02	1.04

Chapter 6

Simulation of Turbulent Wake of Subcritical Circular Cylinder

Flow over circular cylinder is a well-studied problem, abundant experimental and numerical data is available from low-Reynolds number laminar flow up to supercritical high-Reynolds number turbulent flow. In our test, the circular cylinder Reynolds number $Re_D = 6.4 \times 10^4$, which corresponds to subcritical flow regime. Cylinder experiences laminar separation and flow bursts into turbulence inside the shear layer. Alternative vortices are formed from shear layer roll-up and shed downstream with constant Strouhal number St. Beyond the subcritical regime, the cylinder boundary layer transition initiates before separation and delays the separation points, which significantly reduces the pressure drag and total drag, it is named the "drag crisis".

In this chapter, the 3D numerical result from our transition hybrid model is presented and compared with experimental data acquired in our wind tunnel tests. Section 6.1 introduces the simulation setups including computation mesh, numerical schemes and boundary conditions. Section 6.2 presents the analysis of instantaneous, mean fields and flow statistics from simulations and experiments, the comparison shows good agreement which further confirms the performance of our transition hybrid model in predicting unsteady aerodynamics.

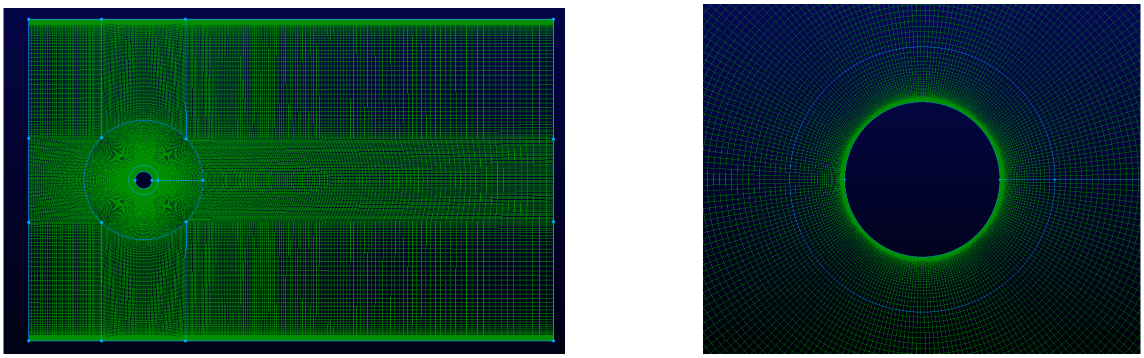

Figure 6.1: Computational domain and refined mesh around circular cylinder

6.1 Problem Setup

The hybrid model flow simulation requires refined boundary layer mesh and high-order differencing schemes. This section introduces the computational grid and simulation setups, including boundary conditions and numerical schemes.

6.1.1 Computation Mesh

The computation domain (figure 6.1) extends $6.67D$ upstream and $37D$ downstream of the circular cylinder, the transverse dimension measures $\pm 13D$, which matches the test section dimension. DES and LES studies [70,93,103] of the circular cylinder tested various spanwise dimension λ, although correlation still exists at a minimum of $15D$ at experiments, the test results agreed reasonably well with the experimental data for λ value between $2D$ and $3D$. In current study, the spanwise dimension is fixed at $2.67D$. The height of first layer of mesh in wall-normal direction is refined to $y^+ \sim 1$, which conforms to the transition model grid requirements [89].

Grid convergence study was conducted on three systematically-refined mesh, the one used in current study has total cells of approximately 2.77 million and was decomposed into 64 subdomains for parallel computation, approximately $43k$ cells per processor.

6.1.2 Boundary Conditions and Numerical Schemes

The boundaries of computational domain include *cylinder, tunnelWall, inlet, outlet, front* and *back*, table 6.1 summarizes the boundary conditions and corresponding values for flow fields velocity(U), pressure(p), TKE(k), specific dissipation(ω), subgrid eddy viscosity(ν_{sgs}), LM turbulence intermittency(γ) and transition momentum thickness Reynolds number($\tilde{Re}_{\theta t}$).

Table 6.1: Boundary conditions of cylinder flow simulation

	cylinder	**tunnelWall**	**inlet**	**outlet**	**front**	**back**
U	fixedValue (0 0 0)	fixedValue (0 0 0)	fixedValue (26 0 0)	zeroGradient	cyclic	cyclic
p	zeroGradient	zeroGradient	zeroGradient	zeroGradient	cyclic	cyclic
k	fixedValue 1e-12	fixedValue 1e-12	fixedValue 6.8e-4	zeroGradient	cyclic	cyclic
ω	zeroGradient	zeroGradient	fixedValue 3400	zeroGradient	cyclic	cyclic
ν_{sgs}	calculated	calculated	calculated	zeroGradient	cyclic	cyclic
γ	zeroGradient	zeroGradient	fixedValue 1.0	zeroGradient	cyclic	cyclic
$\tilde{Re}_{\theta t}$	zeroGradient	zeroGradient	fixedValue 494	zeroGradient	cyclic	cyclic

The TKE is 0 at walls, in order to maintain numerical stability the value of k is fixed at 1e-12 at cylinder and tunnelWall. Study [86] found the turbulence intensity measured in wind tunnel usually cannot be directly used in simulation, since the turbulence spectrum content length scale is irrelevant to boundary layer length scale and large eddies should be felt as unsteadiness. For $k-\omega$SST turbulence model the freestream value of k and ω are calculated as:

$$\begin{aligned} k &= 1 \times 10^{-6} U_\infty^2 = 6.8 \times 10^{-4} m^2/s^2 \\ \omega &= 5U_\infty/L = 3400/s \end{aligned}$$

where L is the characteristic length of the model, which in this case is the cylinder diameter.

The inlet value of $\tilde{Re}_{\theta t}$ is calculated through empirical correlation [82]. The boundary condition *calculated* uses other flow field value at the boundary to calculate the current flow field, the eddy viscosity is calculated by $\nu_{sgs} = k/\omega$. Periodic boundary condition *cyclic* is imposed on patch *front* and *back*.

OpenFOAM does not provide default discretization scheme for differential operators in transport equations. User has to specify both temporal and spacial discretization schemes for each term. The Gauss's theorem is applied to the volume integrals in finite volume method:

$$\int_V \nabla \cdot \mathbf{a} dV = \int_S d\mathbf{S} \cdot \mathbf{a} \tag{6.1}$$

$$\int_V \nabla \phi dV = \int_S d\mathbf{S}\, \phi \tag{6.2}$$

$$\int_V \nabla \mathbf{a} dV = \int_S d\mathbf{S}\, \mathbf{a} \tag{6.3}$$

Second-order central differencing scheme is used for all gradient terms. The divergence terms adopt a hybrid algorithm named Linear-Upwind Stabilized Transport(LUST) scheme defined as [94]:

$$q_{LUST} = bq_c + (1 - b)q_u \tag{6.4}$$

where q_u and q_c are interpretations from linear upwind and central schemes respectively. The LUST scheme in OpenFoam use a fixed blending factor of $b = 0.75$, i.e. 75% central scheme and 25% linear upwind scheme. LUST provides second order accuracy while maintaining numerical stability in case of low-quality mesh in LES simulations.

The temporal scheme uses *CrankNicolson* algorithm with an off-centering coefficient ψ, which enables the flow solver seamlessly switches from first-order Euler scheme($\psi = 0$) to second-order CrankNicolson($\psi = 1$). $\psi = 0.9$ is used for both boundedness and stability. For diffusion term in the form of $\nabla \cdot (\nu \nabla U)$ the central differencing is used for the diffusion coefficient ν and *corrected* for surface normal gradient term.

6.2 Results and Analysis

The cylinder flow is analyzed extensively, this section categorizes the results into instantaneous, mean and flow statistics. The experimental results are also presented and compared with the simulation data.

6.2.1 Grid Convergence Study

The simulation is conducted using three systematically refined mesh (2× in all three dimensions). Grid statistics of the coarse, medium and fine mesh is summarized in table 6.2.

Table 6.2: Grid statistics for circular cylinder of $Re_D = 6.4 \times 10^4$, mean drag coefficient $\overline{C_D}$ and root mean square of lift coefficient C_L

Grid	**Average y^+ on surface**	**Cells around cylinder**	**Total cell**	$\overline{C_D}$	C_L'	St
Coarse	$\approx 2 (y = 2 \times 10^{-5} m)$	120 ($AR = 50$)	328,680	0.64	0.16	0.256
Medium	$\approx 1 (y = 1 \times 10^{-5} m)$	240 ($AR = 50$)	2,768,566	1.31	0.67	0.193
Fine	$\approx 0.5 (y = 5 \times 10^{-6} m)$	480 ($AR = 50$)	21,790,080	1.35	0.71	0.190

All three simulations use the Transitional-$k-\omega$ SST-DDES model as introduced in chapter 3, same numerical schemes are applied to solve the equations. The time step is fixed at $3 \times 10^{-6} s$ in all cases, which corresponds to maximum Courant number of approximately 2 in the case of finest mesh, it is a good compromise between numerical stability and simulation time. From the table above, the mean drag $\overline{C_D}$ and lift fluctuations C_L' of the Coarse mesh is only 49% and 24% respectively compared with results from Medium mesh. The Fine mesh barely improves the force and vortex shedding frequencies compared with medium mesh, the differences are within 5%.

The mesh outside the boundary is designed to resolve part of the turbulence energy by the hybrid model, the resolved fluctuations are measured by the Reynolds stress. Compare the resolved Reynolds stress field across the cylinder wake at $1D$ downstream illustrates the

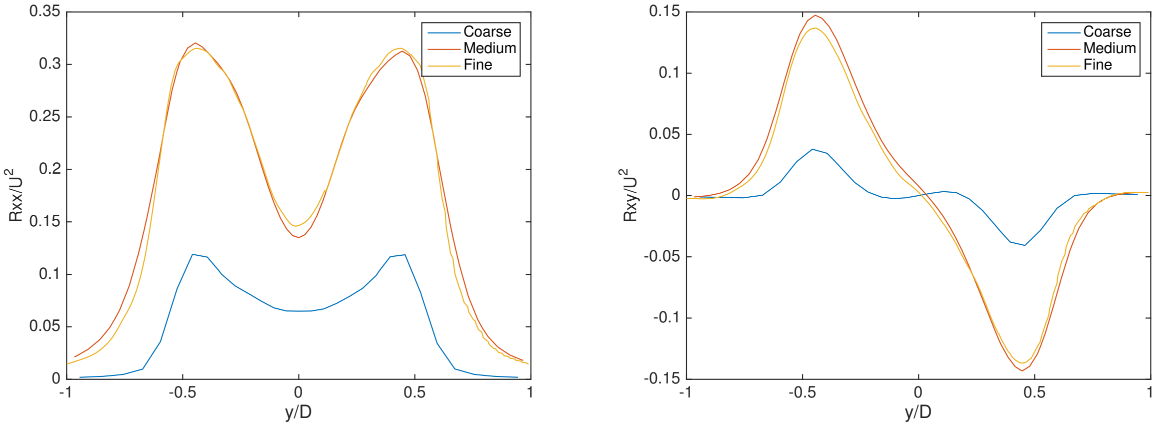

(a) Normalized $\overline{u'u'}$

(b) Normalized $\overline{v'v'}$

Figure 6.2: Normalized Reynolds stress components from three grids

amount of turbulence that is resolved by the mesh. From figure 6.2, it is clear that the Coarse mesh cannot support resolving as many fluctuations as the other two grids, and the Medium and Fine mesh resolves similar amount of fluctuations and the distribution meet the experimental data as shown in later section.

Considering significantly more computing resource is required in the Fine mesh case (8×) compared with the Medium case and the good agreement of the flow physics they predict, the Medium mesh is chosen as the main running case, and the similar resolution is applied to the downstream airfoil as shown in next chapter.

6.2.2 Instantaneous Flow Field

The circular cylinder flow is highly unsteady at subcritical Reynolds number, the cylinder flow experiences laminar separation, transition in shear layer and periodic vortex shedding. This section examines the instantaneous flow field.

Cylinder lift and drag

Cylinder lift and drag forces oscillate with vortex shedding, the corresponding force coefficients are giving by:

$$C_l = \frac{l}{\frac{1}{2}\rho U_0^2 D\lambda_z} \tag{6.5}$$

$$C_d = \frac{d}{\frac{1}{2}\rho U_0^2 D\lambda_z} \tag{6.6}$$

Due to the symmetrical nature of vortex shedding, the drag force oscillates at twice the frequency of lift force. From figure 6.3 the drag coefficient C_d oscillates around 1.3 and the lift coefficient C_l averages at 0. Both force coefficients are plotted against non-dimensionalized time $T = tU_0/D$, the first 0.2s history is neglected to exclude any transient effects on the cylinder and $T = 700$ equals to $1s$ time. As in the grid study simulations, the simulation time-step is fixed at $3 \times 10^{-6}s$, which corresponds to sampling rate of $333,333Hz$. The spectrum of the oscillatory force on circular cylinder (figure 6.4) shows a dominant lift frequency at 132Hz, which corresponds to Strouhal number $St = \frac{fD}{U_0} = 0.193$. The wake shedding frequency from our PIV experiment is approximately $126Hz$ and $St = 0.185$. Complied experimental data of St for circular cylinder at Reynolds number around $64,000$ is in the range of $0.186 - 0.196$ [95], the simulation data lies in the middle of the range.

Pressure distribution

From the analysis of oscillating force the shedding period is $T_s = 1/132 = 0.00758s$, the variation of the pressure distribution is studied by dividing one shedding cycle into 8 phases as shown in figure 6.5. The instantaneous pressure fluctuates around the mean pressure distribution, which is symmetrical about 180°. The motion of the pressure distribution indicates two eddies are shed from cylinder top and bottom. The instantaneous pressure between two separation points on the upwind side of the cylinder generally matches mean value at any time, the status of the boundary layer and transition will be examined further by the LM turbulence intermittency field.

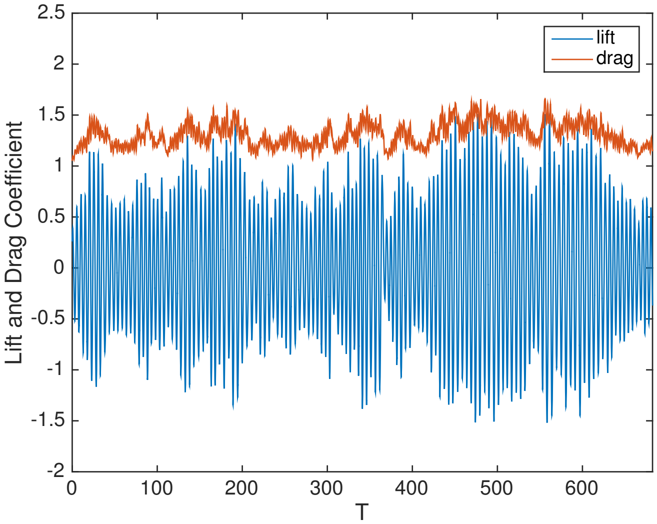

Figure 6.3: Cylinder lift and drag force over non-dimensionalized time T

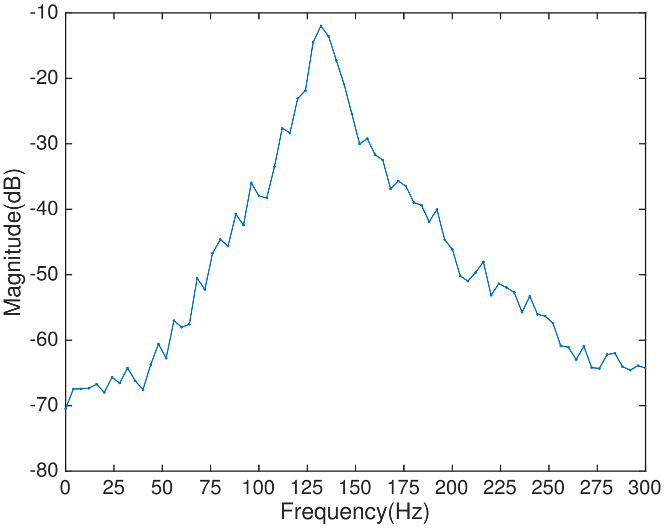

Figure 6.4: Cylinder lift force spectrum

From the figure 6.5, the front stagnation line (azimuthal angle $\theta = 180°$) oscillates with the eddy shedding, same phenomena was observed in experiments from hot-wire signals [96]. The separation points on both sides oscillates with amplitude of approximately $\pm 4°$ with the mean separation angle of $\theta = 95°$, which corresponds to 85° from the front stagnation point. Various experiments were conducted in the range of subcritical Reynolds number, study found the separation angle oscillates between 78° and 90° from the front stagnation point for circular cylinder with $Re_D = 65,000$ [56].

Eddy viscosity and vortex structures

The Boussinesq approximation simplifies the modeling of Reynolds stress as an analogy to molecule viscosity, the modeled Reynolds stress is calculated as the product of the eddy viscosity ν_t with the strain rate tensor S. Most of the RANS and LES turbulence models solve turbulence quantities for calculating the eddy viscosity, which is then used to close the Navier-Stokes equations. Due to the nature of the hybrid model, outside the boundary layer, the production of turbulence kinetic energy is decreased according to local-grid refinement and part of the turbulence motion is resolved rather than modeled. As a result, the eddy viscosity in our simulation is termed as subgrid eddy viscosity ν_{sgs} as in LES models.

The eddy viscosity around circular cylinder is carried downstream by shedding vortices. Figure 6.6 shows the intensity of eddy viscosity reaches maximum inside the separated boundary layer ($\sim \nu_{sgs}/\nu = 30$), flow shear generates turbulence energy in boundary layer and the hybrid model prohibits the transition to LES mode further maintains the high level of eddy viscosity. It rapidly decreases outside the recirculation zone, which is $0.7D$ behind the rear stagnation point.

The spanwise vorticity is a measure of flow shear in the streamwise-transverse flow plain. Normalized spanwise vorticity $\tilde{\omega}_z = \omega_z/(U_0/D)$ as shown in figure 6.7 illustrates the formation of Karman vortices as the shear layer rolls up and sheds alternatively behind cylinder.

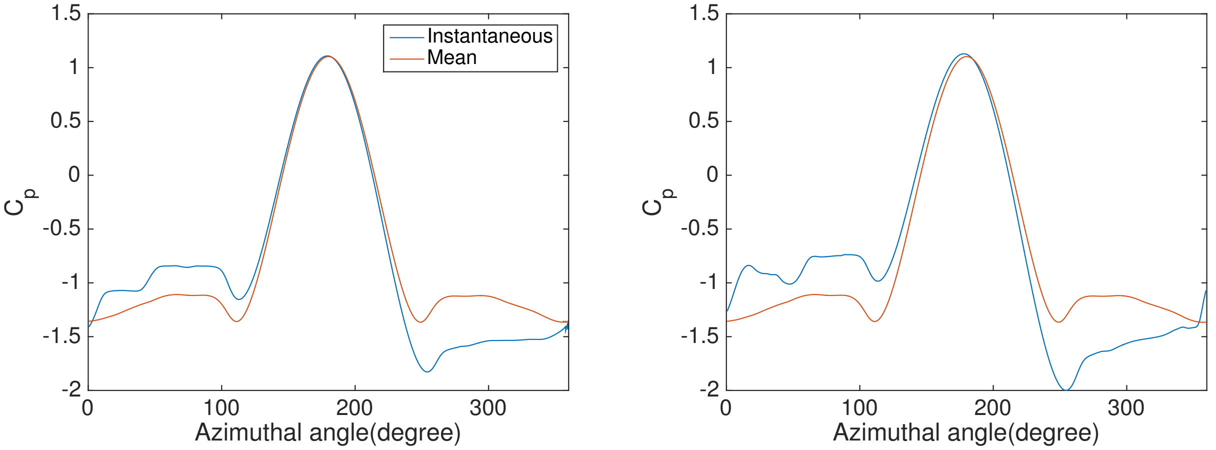

(a) Phase 1

(b) Phase 2

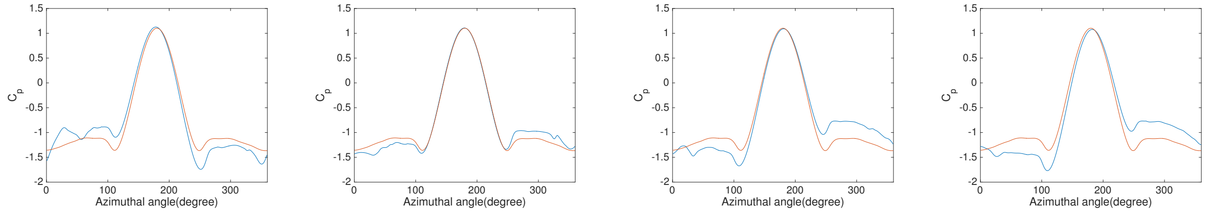

(c) Phase 3

(d) Phase 4

(e) Phase 5

(f) Phase 6

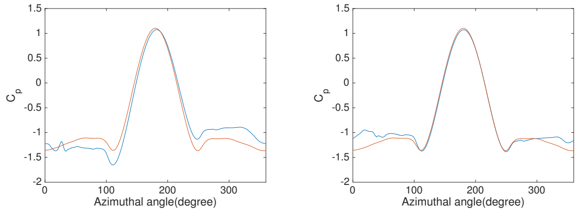

(g) Phase 7

(h) Phase 8

Figure 6.5: Pressure distribution on circular cylinder over one shedding cycle

The stability of the shear layer is correlated with the intensity of eddy viscosity. Compared with the experimental data, the simulation predicts less stochastic structures in cylinder wake than experiment (figure 6.8), and the shear layer is more coherent in the streamwise direction, which leads to longer recirculation zone.

The Q-criterion is the second invariant of the velocity gradient tensor, which is defined as

$$Q = \frac{1}{2}\left\{[tr(\nabla U)]^2 - tr\left[(\nabla U)^2\right]\right\} \tag{6.7}$$

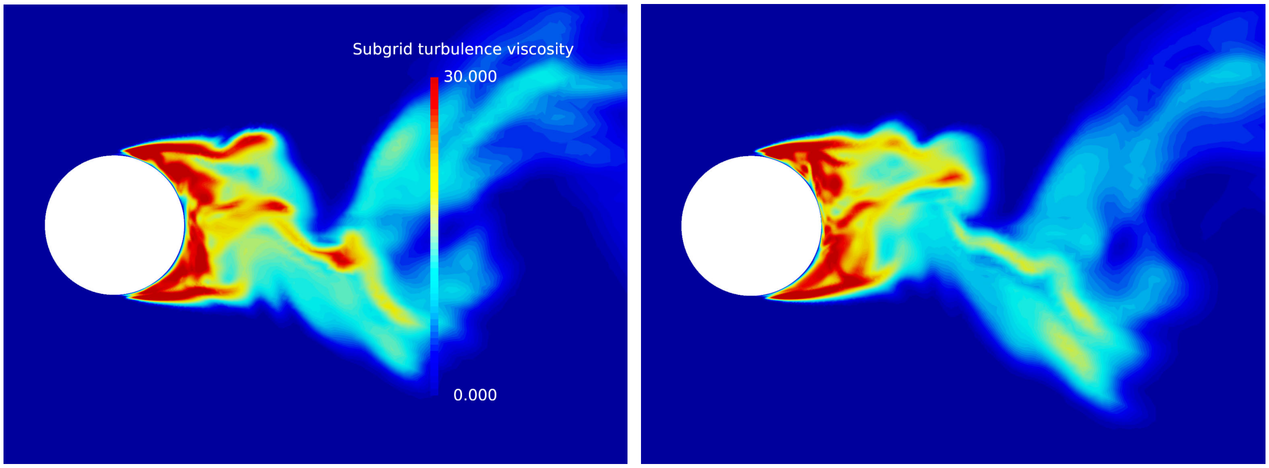

(a) Phase 1

(b) Phase 2

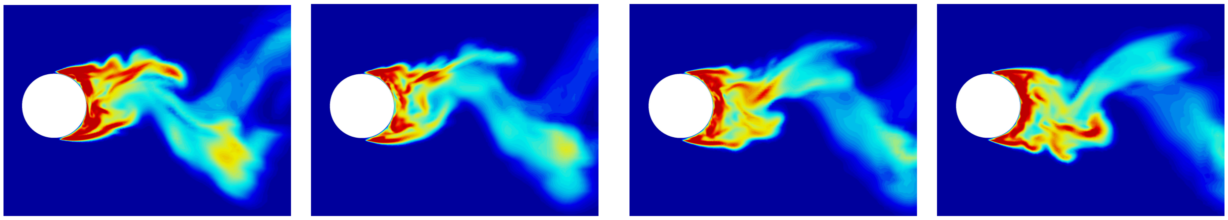

(c) Phase 3

(d) Phase 4

(e) Phase 5

(f) Phase 6

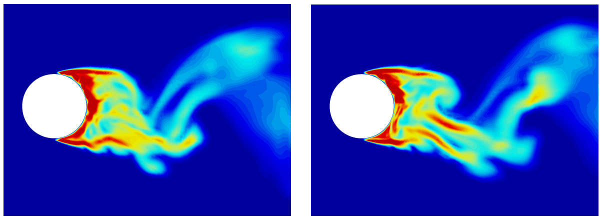

(g) Phase 7

(h) Phase 8

Figure 6.6: Eddy viscosity around circular cylinder over one shedding cycle

Q-criterion gives the spatial region of vortex where the vorticity tensor dominates the rate of strain. Figure 6.9 is a instantaneous iso-surface of Q colored by vorticity magnitude, it outlines the shedding vortices as they travel downstream and diffuse outwards. The spanwise band on circular cylinder before separation indicates uniform separation position. Extensive experiments found significant effects of cylinder aspect ratio on the correlation length in low Reynold number regimes($Re_D < 10^4$). This dependency diminishes beyond $Re_D > 20,000$ and the correlation length $L_c \sim 3D$ [59].

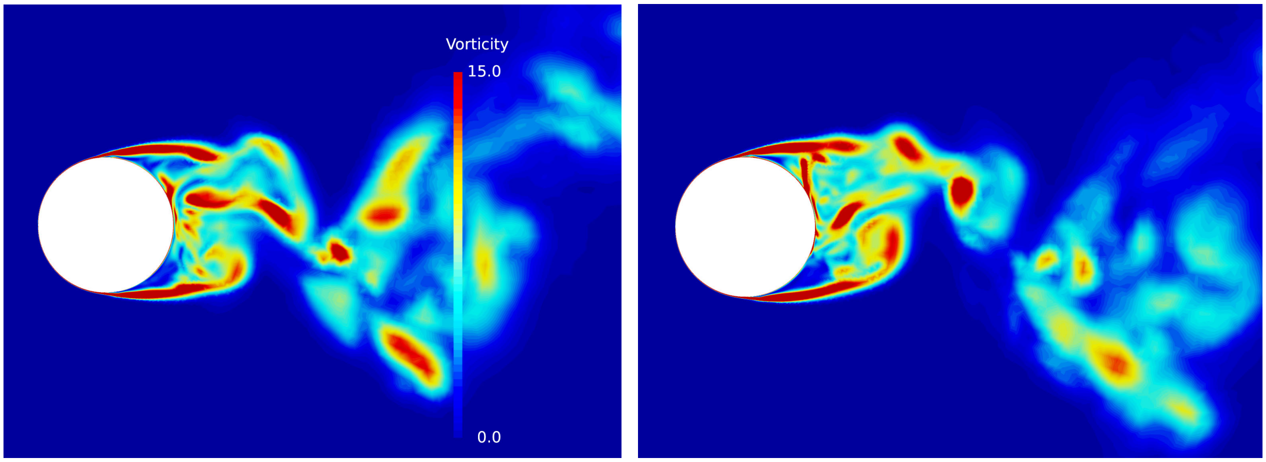

(a) Phase 1

(b) Phase 2

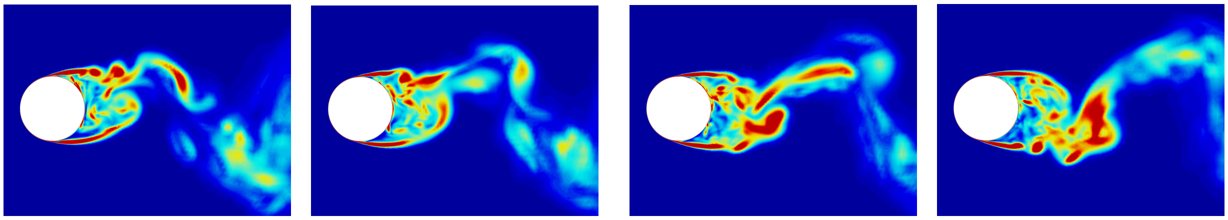

(c) Phase 3

(d) Phase 4

(e) Phase 5

(f) Phase 6

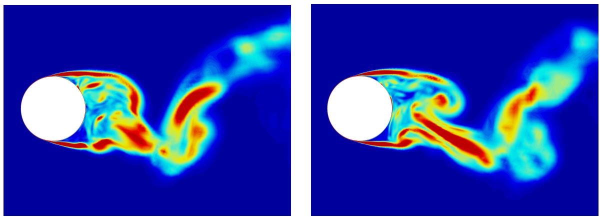

(g) Phase 7

(h) Phase 8

Figure 6.7: Spanwise vorticity magnitude around circular cylinder over one shedding cycle

The 2D transition waves after separation quickly promote the 3D flow development in the cylinder near wake. The shear layer roll-up point varies along the spanwise direction and it soon breaks up and introduces 3D irregularities in the recirculation zone.

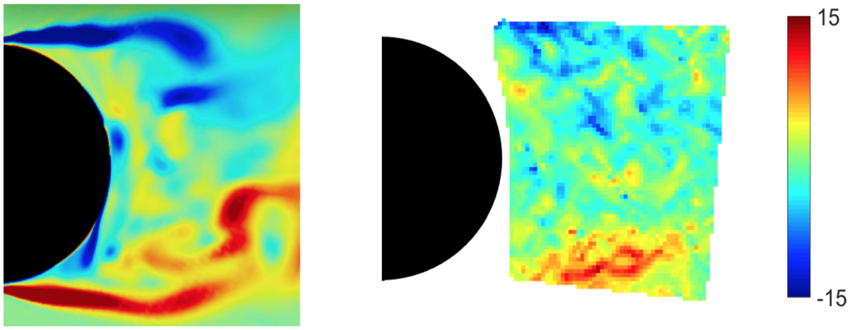

Figure 6.8: Instantaneous spanwise vorticity from left: simulation and right: experiment

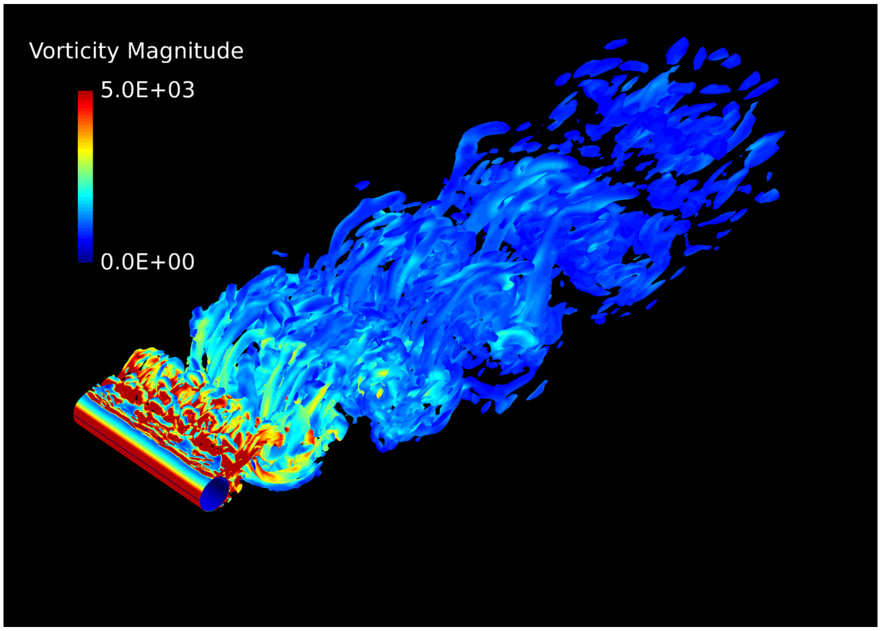

Figure 6.9: Iso-surface of Q criterion of the circular cylinder flow(flow field is mirrored in spanwise direction)

LM turbulence intermittency and skin friction

One key parameter of our transition hybrid model is the LM turbulence intermittency field γ. Physically, the transition is characterized as the eruption of turbulent spots in flow, the definition of the original turbulence intermittency is the proportion of time that the flow is in turbulent state. The turbulence models without transition prediction assumes everywhere in the flow is fully turbulent 100% of time. In $k-\omega$SST model, the production of the turbulence kinetic energy is the product of shear stress and flow strain rate.

Statistically, the turbulence intermittency is the ratio of the total amount of TKE produced over time to the TKE predicted by the turbulence model(fully-turbulent). Therefore, the intermittency filed is multiplied with the TKE production of fully-turbulent prediction. However, in current model, the intermittency field is calculated by a transport equation as other turbulence fields. Instead of representing a statistical state of flow, the LM turbulence intermittency field γ is only served as a measure to reduce TKE production. Two modifications deviates γ from its physical definitions: 1) $\gamma = 1$ in freestream where flow is laminar 2) $\gamma > 1$ in separated flow. The first modification enables the model to predict the effects of large freestream turbulence level on the laminar boundary layer and the later modification helps capturing the separation-induced transition by making TKE grows rapidly after laminar separation.

The LM intermittency distribution on circular cylinder is plotted over one shedding cycle in figure 6.10. The peak near the front stagnation point ($\theta = 180°$) is a numerical artifact which is caused by the diffusion of freestream LM intermittency ($\gamma_\infty = 1$). Between 100° and 260° on circular cylinder, which corresponds to ±80° from the front stagnation point, the distribution of LM intermittency field γ remains low and steady over the entire shedding cycle (figure 6.10), and the boundary layer remains laminar.

There are fluctuations of γ in the range of azimuthal angle $50° < \theta < 100°$ and $260° < \theta < 310°$, the mean separation angles 95° and 265°, as shown in the pressure distribution plots, are inside the transitional regions. However, the value of γ at the mean separation

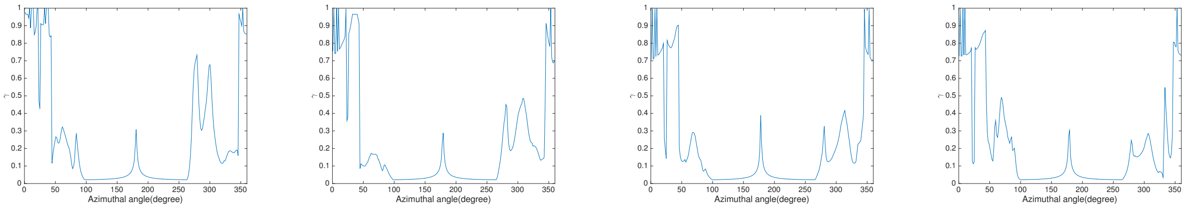

(a) Phase 1 (b) Phase 2 (c) Phase 3 (d) Phase 4

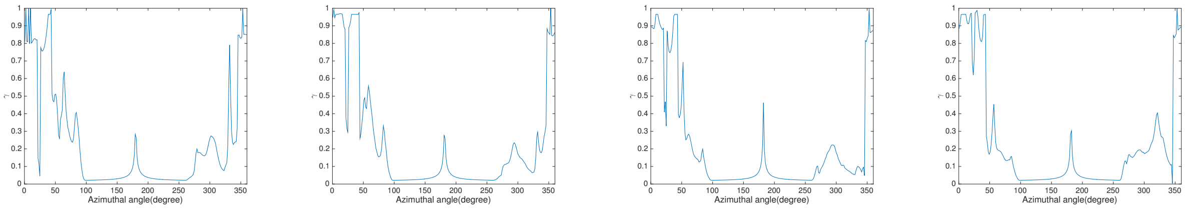

(e) Phase 5 (f) Phase 6 (g) Phase 7 (h) Phase 8

Figure 6.10: LM turbulence intermittency field on circular cylinder over one shedding cycle

locations never exceed 0.1 and we can conclude that the boundary layer experiences laminar separation. The LM intermittency field quickly grows up at $\theta < 50^\circ$ and $\theta > 310^\circ$ and the boundary layer is turbulent over the range of ±50° of the rear stagnation point.

The skin friction coefficient is defined as

$$C_f = \frac{\tau_w}{\frac{1}{2}\rho U_0^2} \tag{6.8}$$

From figure 6.11, the skin friction magnitude peaks at ±50° from the front stagnation point, it then drops rapidly towards 0 at the laminar separation points. The friction peak also alternates as the vortex sheds from upper or lower side. The separation bubbles between $50^\circ - 95^\circ$ and $265^\circ - 310^\circ$ lead to local low skin friction as the reverse flow decreases velocity gradient in normal direction, which is directly proportional to wall shear stress.

Blending function of hybrid model

The blending of the hybrid model is fulfilled by the blending function F_{DDES}, which is directly multiplied with the destruction term in the TKE equation. From equation 3.48 and 3.49 the

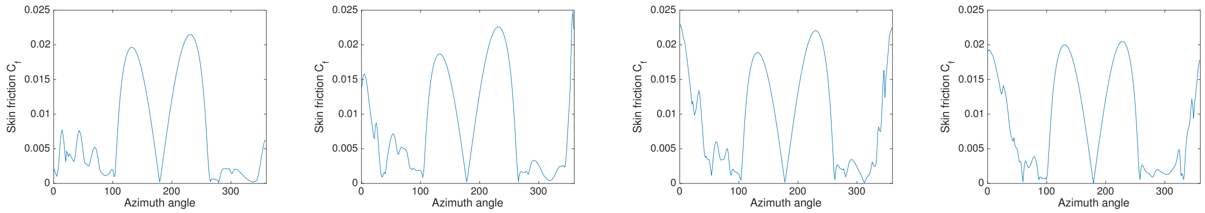

(a) Phase 1 (b) Phase 2 (c) Phase 3 (d) Phase 4

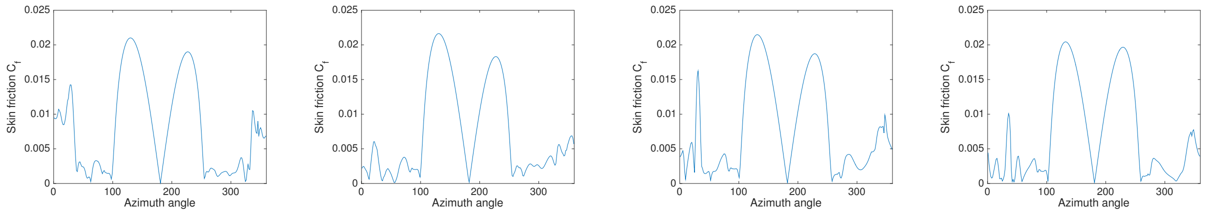

(e) Phase 5 (f) Phase 6 (g) Phase 7 (h) Phase 8

Figure 6.11: Skin friction magnitude on circular cylinder over one shedding cycle

blending function is calculate from RANS destruction term D_k and hybrid destruction term D'_k, viz.

$$F_{DDES} = \frac{D'_k}{D_k} \tag{6.9}$$

According to the definition of D_k and D'_k, we have

$$\frac{D'_k}{D_k} = \frac{L_R}{L_H} = \frac{\sqrt{k}}{\sqrt{k} - f_d max\left(0, \sqrt{k} - C_{DES}\Delta\beta^*\omega\right)} \tag{6.10}$$

Since the new hybrid destruction term is given by $F_{DDES}D_k$, the modeled turbulence is reduced in regions of $F_{DDES} > 1$.

Inside cylinder boundary layer, F_{DDES} remains value of 1 (figure 6.12), which preserves the boundary layer to RANS, it is essential for the the hybrid model to work properly since the boundary layer mesh cannot support resolved turbulence structures. The distribution of F_{DDES} correlates with eddy viscosity (figure 6.6). Outside the cylinder wake, turbulence is close to freestream level, examine the definition of F_{DDES} in equation 6.10, the max function returns 0 as $\sqrt{k} < C_{DES}\Delta\beta^*\omega$, hence $F_{DDES} = 1$.

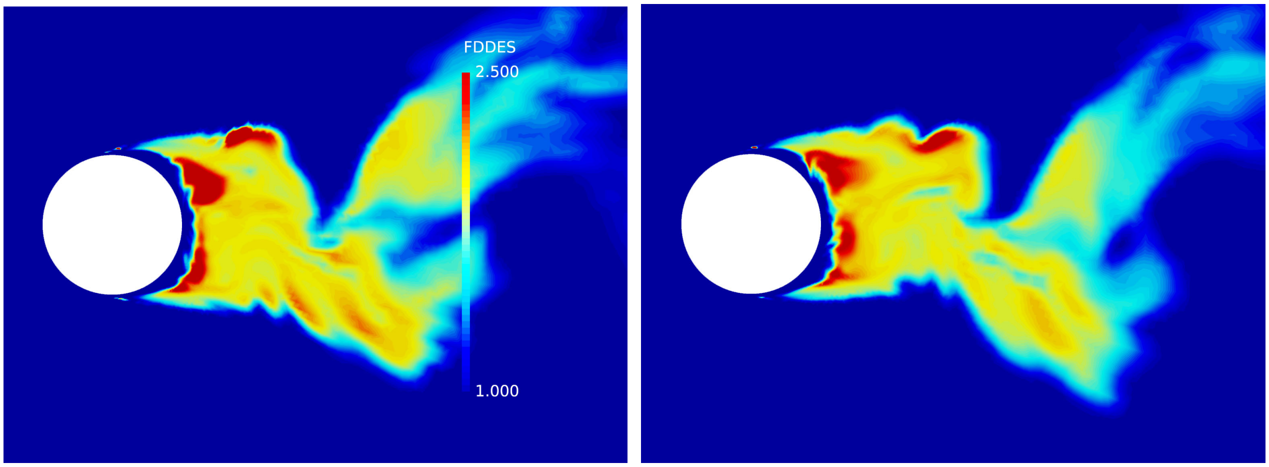

(a) Phase 1

(b) Phase 2

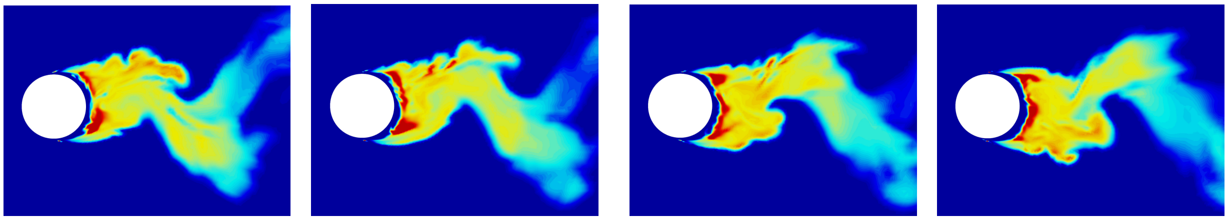

(c) Phase 3

(d) Phase 4

(e) Phase 5

(f) Phase 6

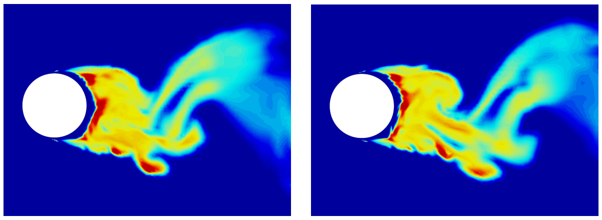

(g) Phase 7

(h) Phase 8

Figure 6.12: Blending function F_{DDES} around circular cylinder over one shedding cycle

Velocity fluctuations along wake centerline

The streamwise and transverse velocity fluctuations u' and v' correlate with the vortices as they are carried downstream by the mean flow. Similar to the lift and drag variations, which are essentially induced by the velocity fluctuations, u' oscillates at twice the frequency as v' (figure 6.13). The spanwise fluctuation is relatively independent from the vortex shedding, the general shape of w' stays relatively stationary over one shedding cycle. The magnitude of u' decays from $\sim 0.5U_0$ in the recirculation zone towards $\sim 0.3U_0$ approximately $2D$ downstream and maintains its level until $10D$, where the airfoil will be placed in the full-model case. The decaying of v' follows similar behavior and $v' \sim 0.5U_0$ from $2D$ to $10D$. The mean v and w components are approximately 0 along the wake centerline and the mean streamwise component u gradually recovers to $0.75U_0$. Notice there is a reverse flow region behind the cylinder.

6.2.3 Mean Flow Field

The mean fields reveal the time-averaged flow behaviors, which are hidden by the periodic nature.

Mean velocity field and streamlines

The comparison of mean velocity components in cylinder wake up to $1D$ downstream is shown in figure 6.14. The shape of PIV interrogation widow limits the acquired data in a rectangular region that is tangent to the cylinder surface, all data is normalized by the freestream velocity U_0. The numerical prediction of the length of recirculation zone and width of the wake as seen in figure 6.14a are within 5% difference compared with experimental data.

The streamlines of mean streamwise velocity from simulation in figure 6.15 shows the recirculating flow extend to $0.725D$ downstream of the rear stagnation point, and the width of the wake, which determines the eddy shedding frequency, is approximately $1.1D$. The transverse component $\bar{v}$ is antisymmetric about the center wake line (figure 6.14b), and the main vortices' form region is centered around $1.3D$ downstream of the cylinder center. Another notable feature from figure 6.14b is the small counter-rotating region near cylinder rear surface, which corresponds to the separation bubbles as seen in experimental data. The spanwise component $\bar{w}$ is about one order of magnitude lower than $\bar{u}$ and $\bar{v}$, no distinct structure is visible from both numerical and experimental data. Since the computational domain is limited to $2.67D$ in spanwise direction and the PIV system is insensitive in the spanwise direction, no decisive conclusion can be drawn.

Mean and RMS pressure distribution

The magnitude of the pressure variations on circular cylinder is measured in terms of RMS (figure 6.16 and 6.17). The RMS value matches the mean pressure in the favorable pressure region on both sides of the front stagnation point, which indicates that the accelerating flow is steady. From figure 6.16, the pressure RMS on cylinder surface reaches maximum right before separation. Beyond the separation points, the boundary layer flow quickly becomes turbulent and the pressure variation remains high towards the rear stagnation point.

The distribution of pressure variations in cylinder wake concentrates in the eddy formation region behind the rear stagnation point(figure 6.17). Distribution of the C_p RMS corrolates with the transverse normal Reynolds stress term $\overline{v'v'}$ as shown in figure 6.20.

Mean vorticity and TKE distribution

Both the mean vorticity and mean TKE peak immediately downstream of the separation points (figure 6.18 and 6.19). The mean vorticity field $\overline{\omega}$ is normalized by U_∞/D and mean TKE $\overline{k}$ by U_∞^2. The generation of TKE activates the blending function F_{DDES}, which leads to decreased TKE generation inside the wake. From figure 6.19, the modeled TKE level is negligible in the wake compared to the separation regions. The peak of mean vorticity is at the same level as instantaneous vorticity (figure 6.7), while the magnitude of the mean field reduces significantly at the streamwise position of rear stagnation point, which indicates the shear layer stability breaks down and starts to roll-up to form the Karman vortices.

6.2.4 Flow Statistics

Flow statistics reveals turbulent flow behavior over time. Turbulence model performance is further assessed in terms of resolved energy spectrum and flow oscillations.

Reynolds stress field

Reynolds stress distribution gives the turbulence energy distribution among the fluctuation components (figure 6.20). The streamwise normal component term $\overline{u'u'}$ peaks at approximately $1D$ downstream in both experiments and simulation results. The vertical normal stress $\overline{v'v'}$ reaches maximum at $1.3D$ and $1.4D$ in the simulation and experiment respectively, which indicates the eddy detach point is slightly downstream in the experiments. The shear stress component $\overline{u'v'}$ shows the eddy formation length and its peak is located at the same position as $\overline{v'v'}$. Due to the insensitivity of PIV apparatus to the spanwise component w', the rest three components involving w' shows significant discrepancy between simulation and experiment.

The spanwise correlation length $L_c \sim 3D$ as shown in the previous experiments [59]. The spanwise dimension in simulation is fixed at $\lambda_z = 2.67D$ with periodic boundary condition on opposite sides and the cylinder aspect ratio in experiment is at $18.5D$. The limited spanwise dimension in simulation may lead to more coherent structures and thus higher Reynolds stress due to reduced 3D influence. However, the predicted Reynolds stress field shows good agreement with experimental data on the stress magnitude and some mismatch in eddy formation length of approximately $0.1D$.

Local flow angle in cylinder wake

The local flow fluctuations in cylinder wake determines the boundary layer dynamics on the downstream objects. Instantaneous velocity components are sampled at frequency of $3e6Hz$ and the flow angle is calculated at 4 locations downstream of the cylinder center: $2D$, $4D$,

$8D$ and $10.7D$ (figure 6.21).

At $2D$ downstream of the circular cylinder the flow is dominated by eddies shed from the shear layer, the flow angle ranges from $-180°$ to $180°$ and its distributions reaches peak at $\pm 55°$. The distribution at $4D$ position is plotted in the same scale as $2D$, the flow angle is more evenly distributed and the peak moves to $\pm 45°$, which is caused by the diffusion and break down of turbulence structures. This trends continue developing as moving further downstream, at $8D$, the peak further drops to ~ 0.23 at $\pm 30°$. Finally at $10.7D$, where the airfoil sits in the full surrogate model, the distribution peaks at $\pm 25°$ with extreme value up to $\pm 50°$, further break down of the turbulence structures result in flatter flow angle distribution compared with $8D$.

Flow angle at airfoil position is also extracted from PIV data (figure 6.22). Compared with simulation data of $10.7D$ in figure 6.21d, both peak at $\pm 25°$ with probability density value around 0.23. The experiment shows slightly shallower trough, which indicates more smaller amplitude fluctuations.

Turbulence energy spectrum

The turbulence energy spectrum is inspected on the same cylinder wake center line as the local flow angle distribution. Only the transverse velocity component is analyzed due to its high correlation with flow structures across the centerline. The probes are placed $0.55D$, $0.75D$, $1D$, $1.25D$ and $1.5D$ downstream of the cylinder center.

The velocity is sampled after approximately 50 shedding cycles from the initial transient, the sampling rate is fixed at $3e6Hz$, total sampling time is $1s$. Each group of samples are subdivided into 4 segments with 50% overlap. Figure 6.23 is the compensated power spectrum density of the transverse velocity component v at five probe locations, the horizontal axis is normalized by cylinder shedding frequency $f_{vs} = 132Hz$. The peak at $f/f_{vs} = 1$ indicates that the shedding vortices contains the dominant fluctuating energy in each location.

The hybrid model resolves part of the turbulence energy outside the boundary layer. The compensated PSD shows the range of the frequency that follows the universal Kolmogorov $-5/3$ law and indicates the section of inertial subrange that is resolved by the local mesh. As the turbulence structures decrease below the local mesh size, the compensated PSD curve drops below level and the corresponding mesh cutoff frequency is inversely proportional to the local grid size. Over $1.25D$, the grid size is kept as constant in streamwise direction till far wake, the corresponding resolved turbulence frequency is up to $f = 4f_{vs}$ from figure 6.23d and 6.23e.

6.3 Conclusion and Summary

As the preliminary study, our hybrid transition turbulence model was applied to the circular cylinder flow at subcritical Reynolds number. Systematic grid dependency study was conducted and the grid used in the current study is in the asymptotic range and relatively computationally affordable.

As a well-studied problem, the experimental data of circular cylinder flow is available in literature across all the Reynolds number range. The vortex shedding frequency and flow separation locations agree with our experiments and previous tests in literature. By inspecting the distribution of eddy viscosity and blending function F_{DDES}, the mode switching between RANS and LES occurs outside cylinder boundary layer as expected. Compared with experiment, simulation predicted less stochastic structures within immediate cylinder wake, the stability of the shear layers from separation points was maintained further downstream, which results in slightly longer recirculation zone. The spanwise dimension of $\lambda = 2.67D$ is the possible cause of this discrepancy, research found that the instability acts in the spanwise direction spans over $10D$. We also found that the distribution of local flow angle at airfoil leading edge position follows normal distribution with peaks at $\pm 25^\circ$ and extreme values up to $\pm 50^\circ$.

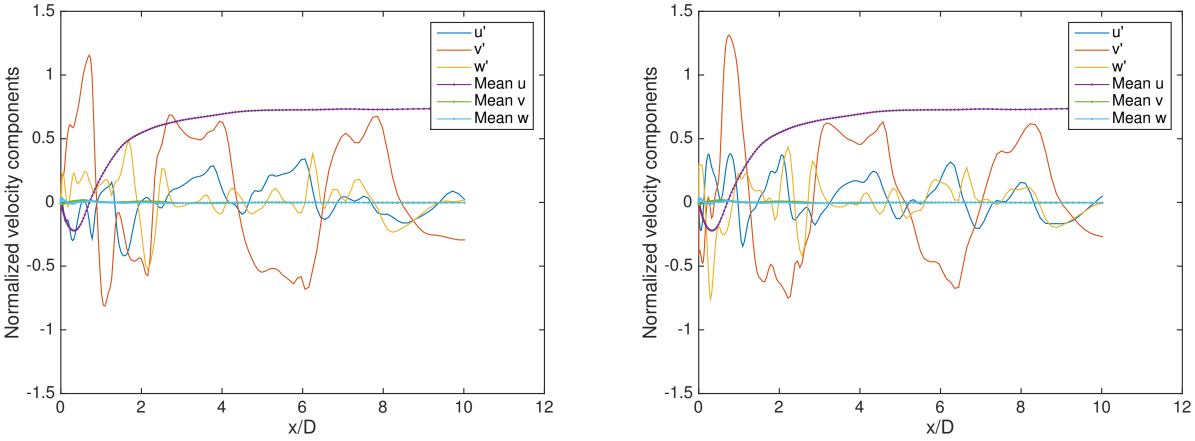

(a) Phase 1 (b) Phase 2

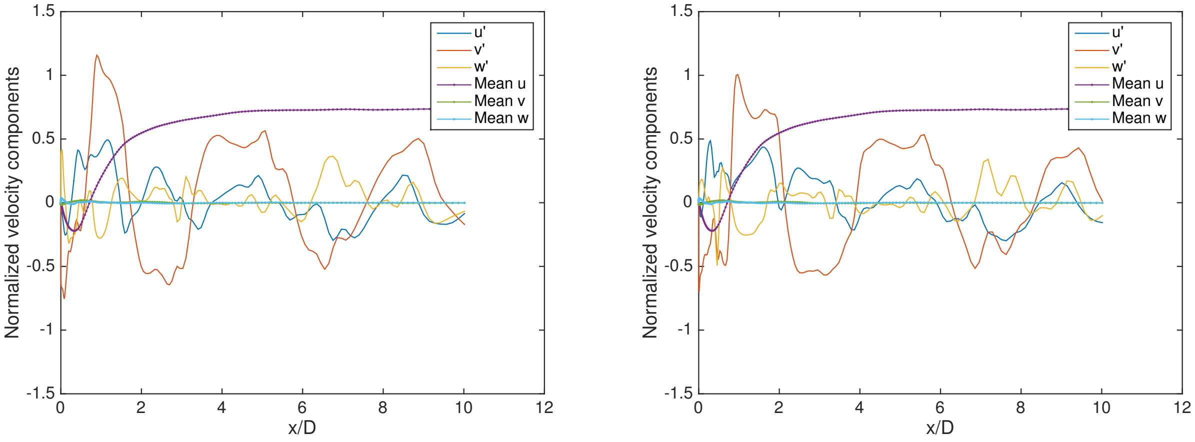

(c) Phase 3 (d) Phase 4

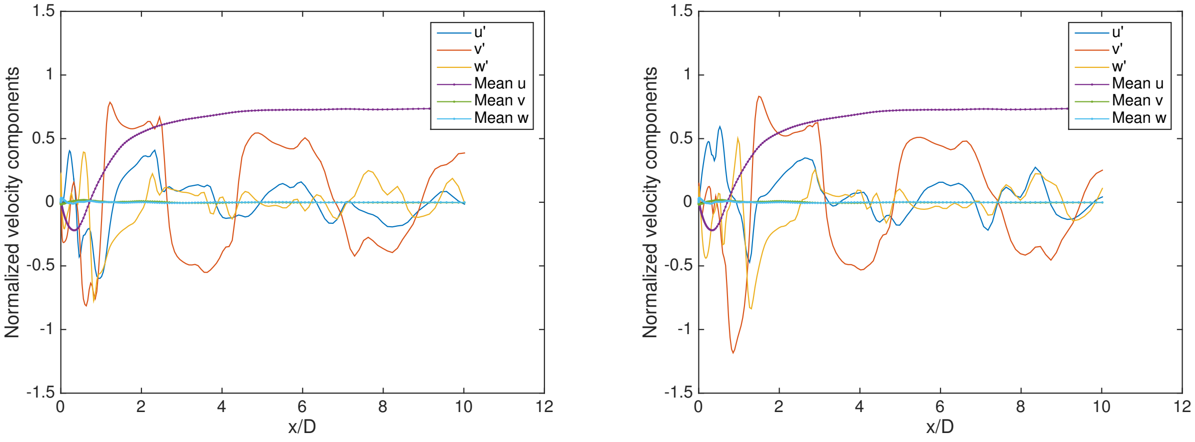

(e) Phase 5 (f) Phase 6

Figure 6.13: Velocity components fluctuations along wake centerline

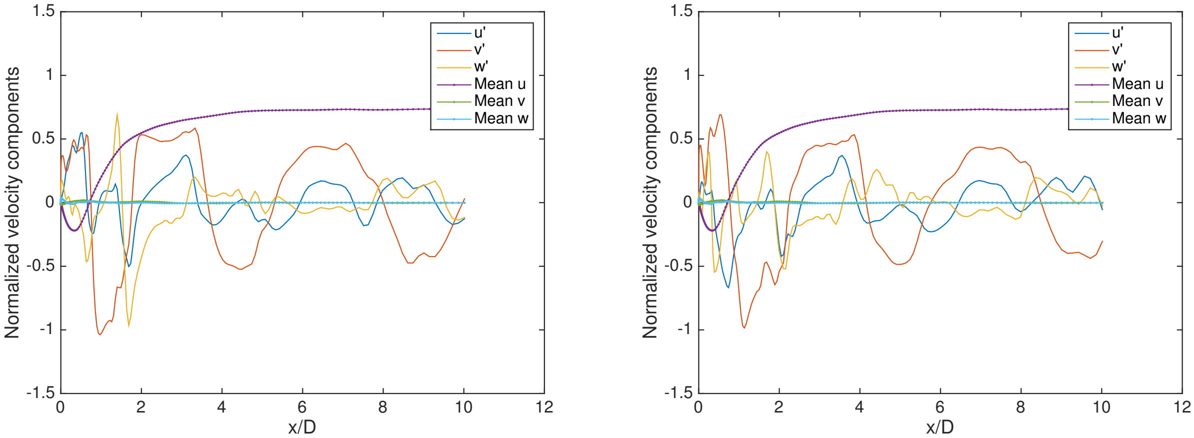

(g) Phase 7

(h) Phase 8

Figure 6.13 (cont.): Velocity components fluctuations along wake centerline

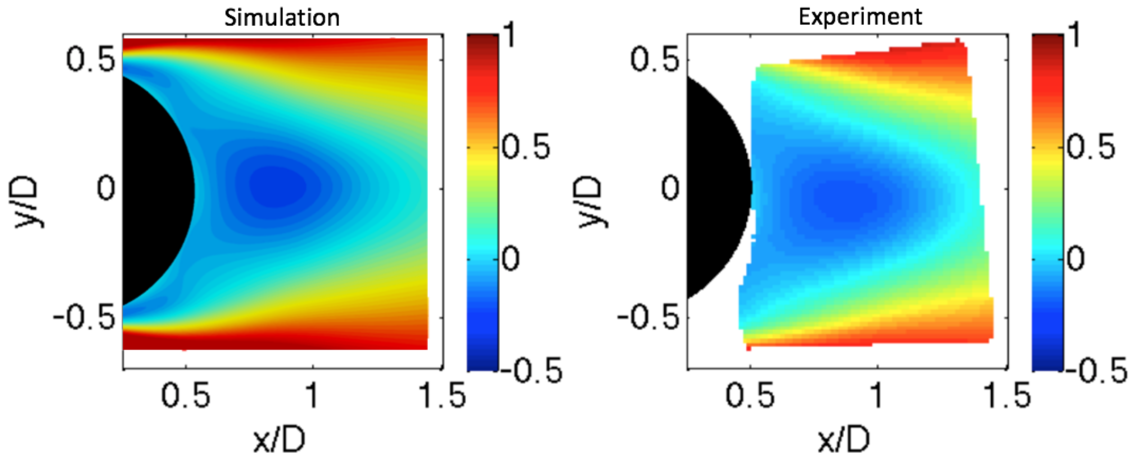

(a) $\bar{u}/U_0$

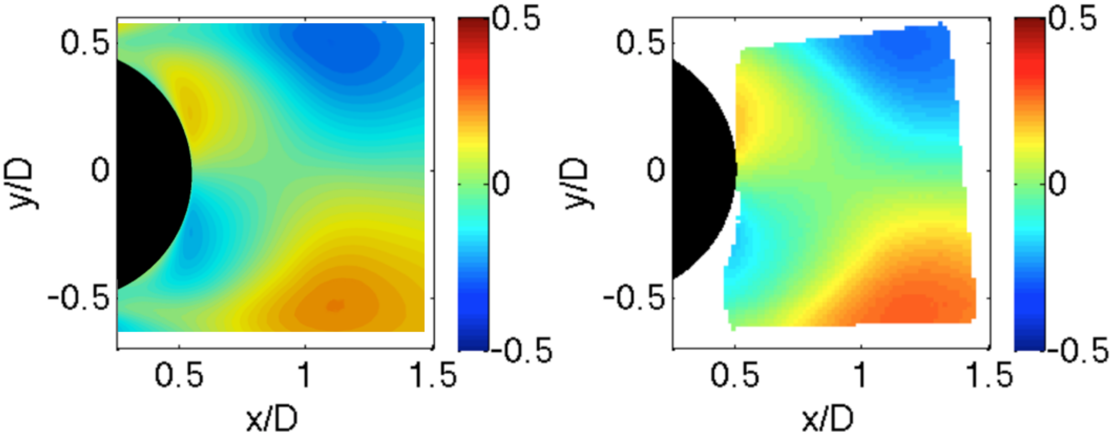

(b) $\bar{v}/U_0$

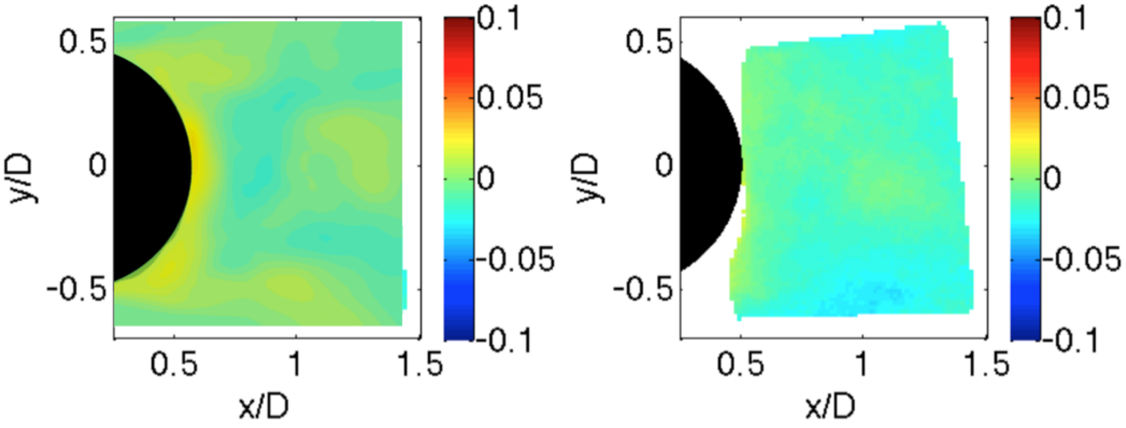

(c) $\bar{w}/U_0$

Figure 6.14: Mean velocity components in cylinder wake

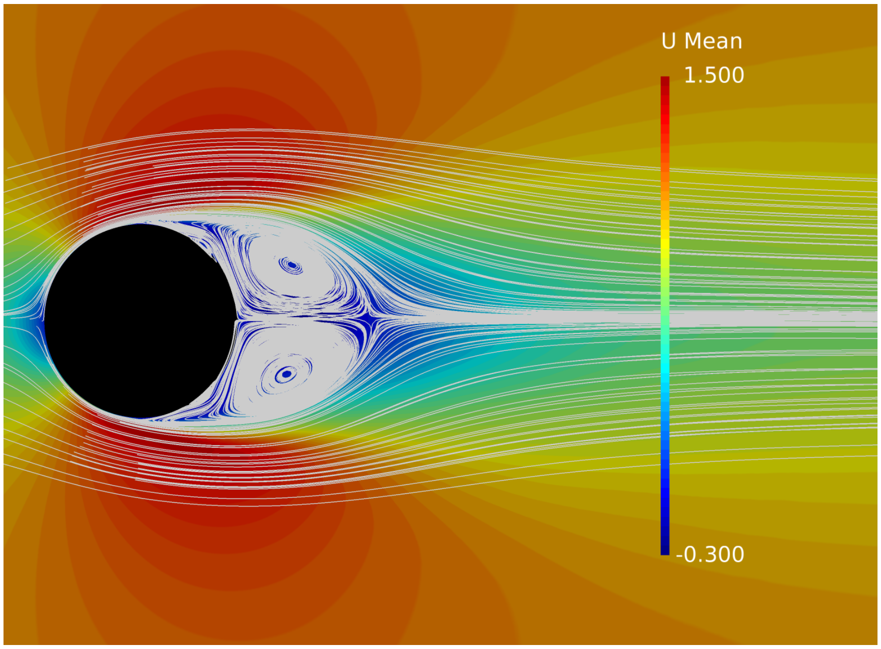

Figure 6.15: Mean streamwise velocity

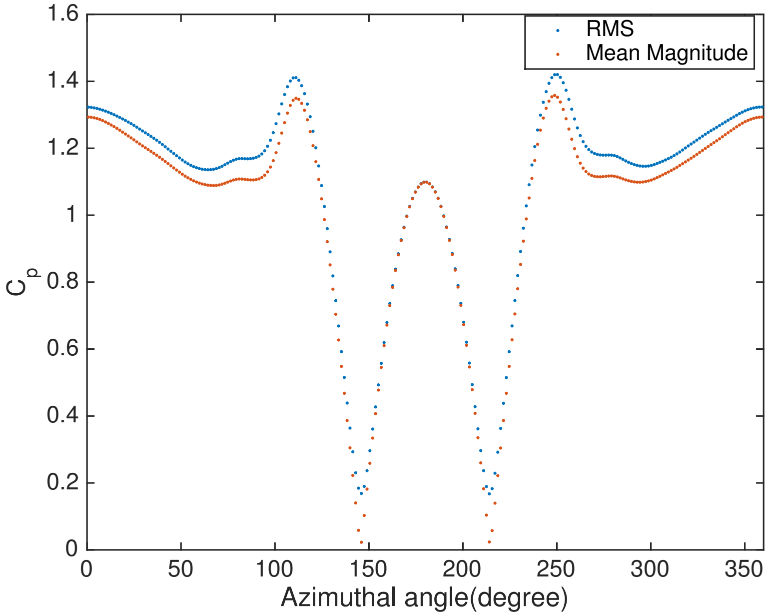

Figure 6.16: Pressure distribution RMS on cylinder surface

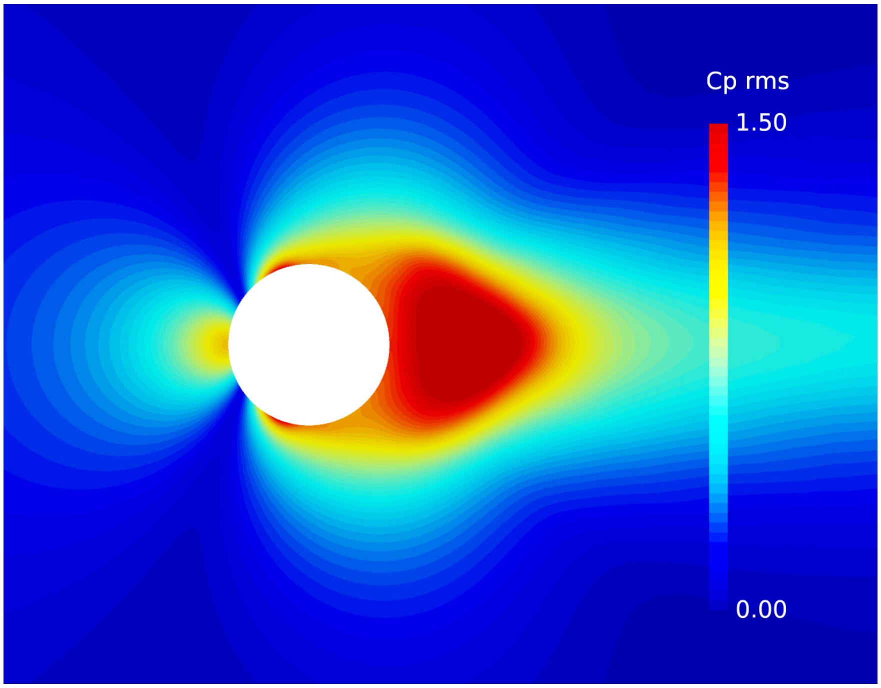

Figure 6.17: Pressure distribution RMS in cylinder wake

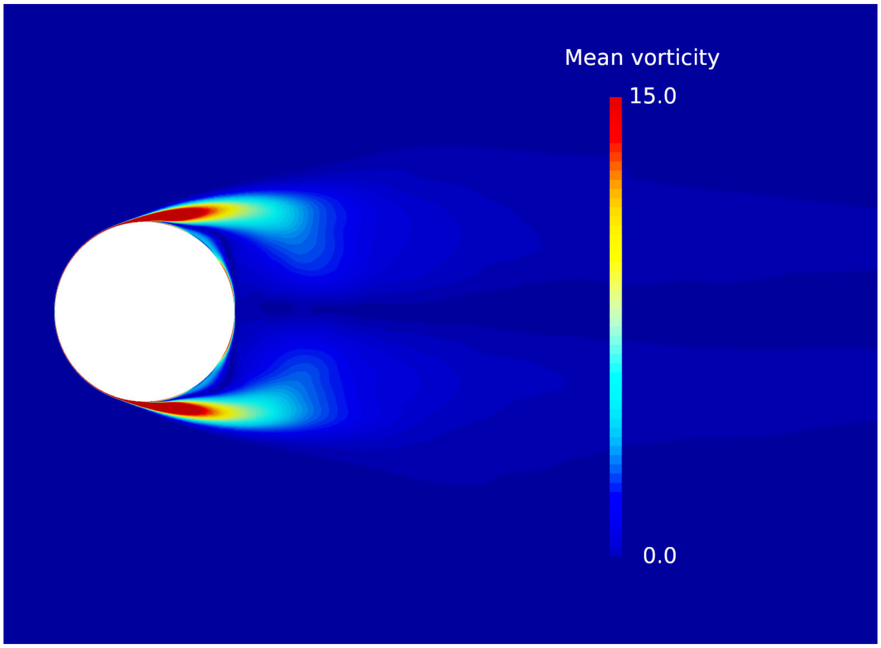

Figure 6.18: Mean vorticity distribution

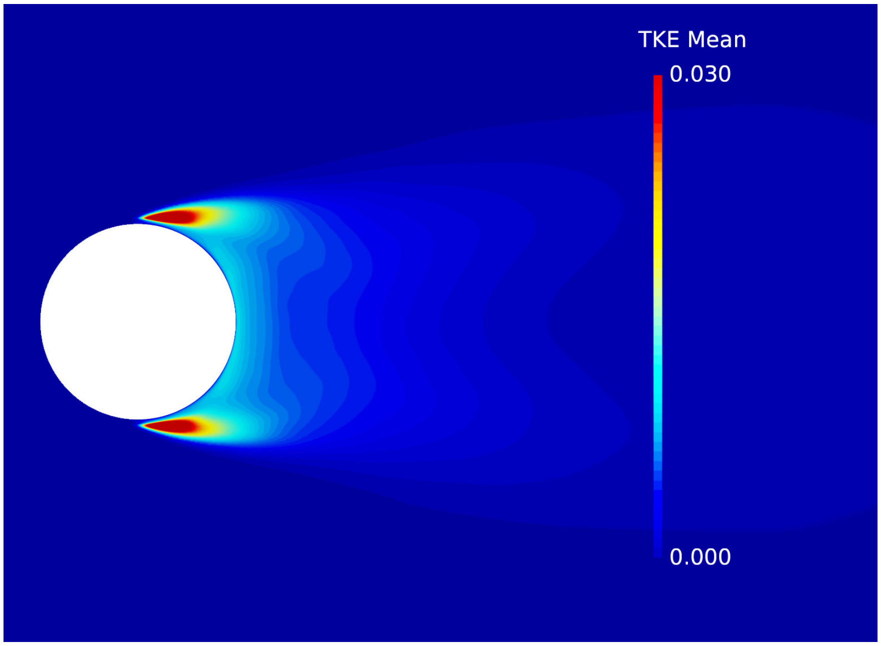

Figure 6.19: Mean TKE distribution

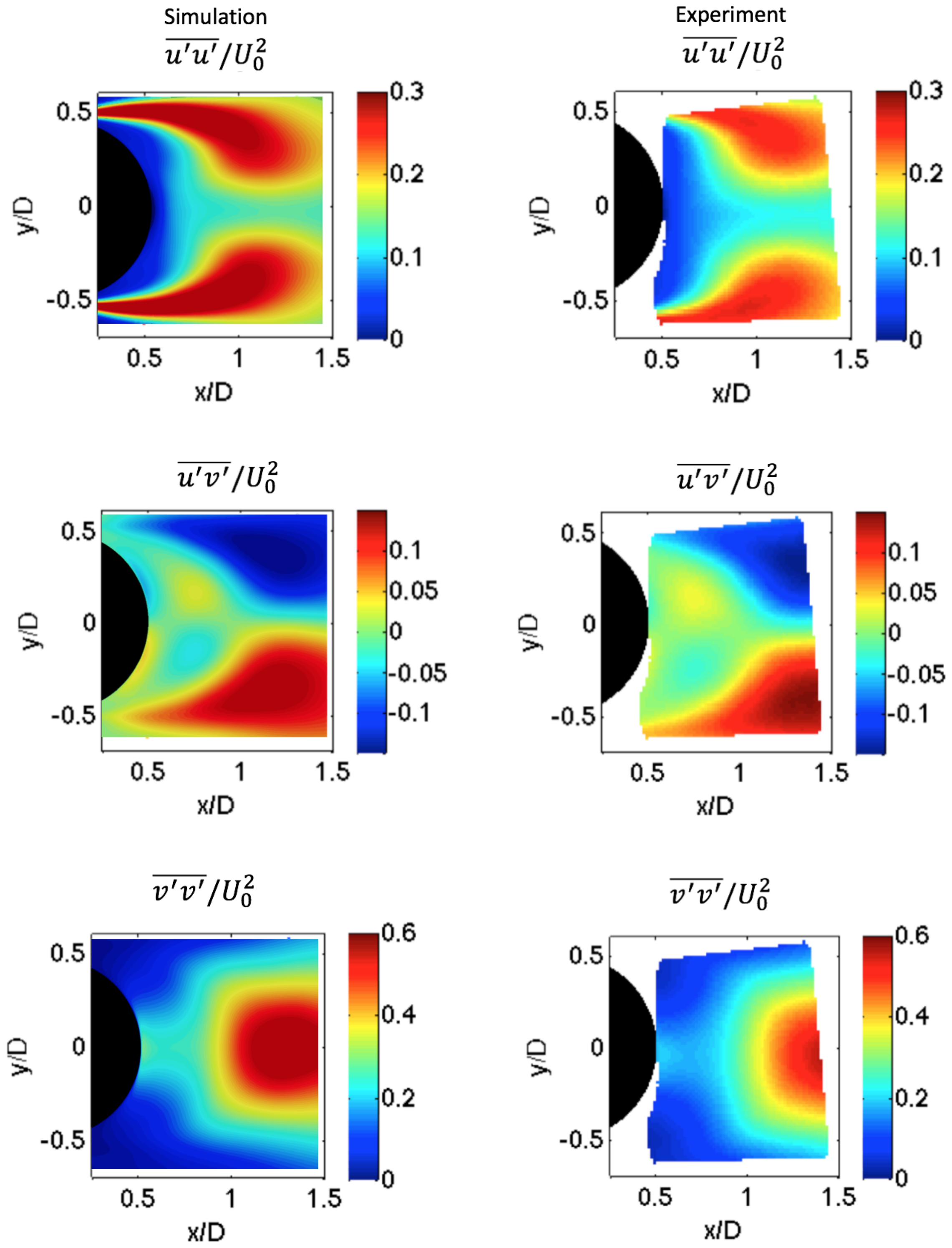

Figure 6.20: Reynolds stress components from simulations and experiments

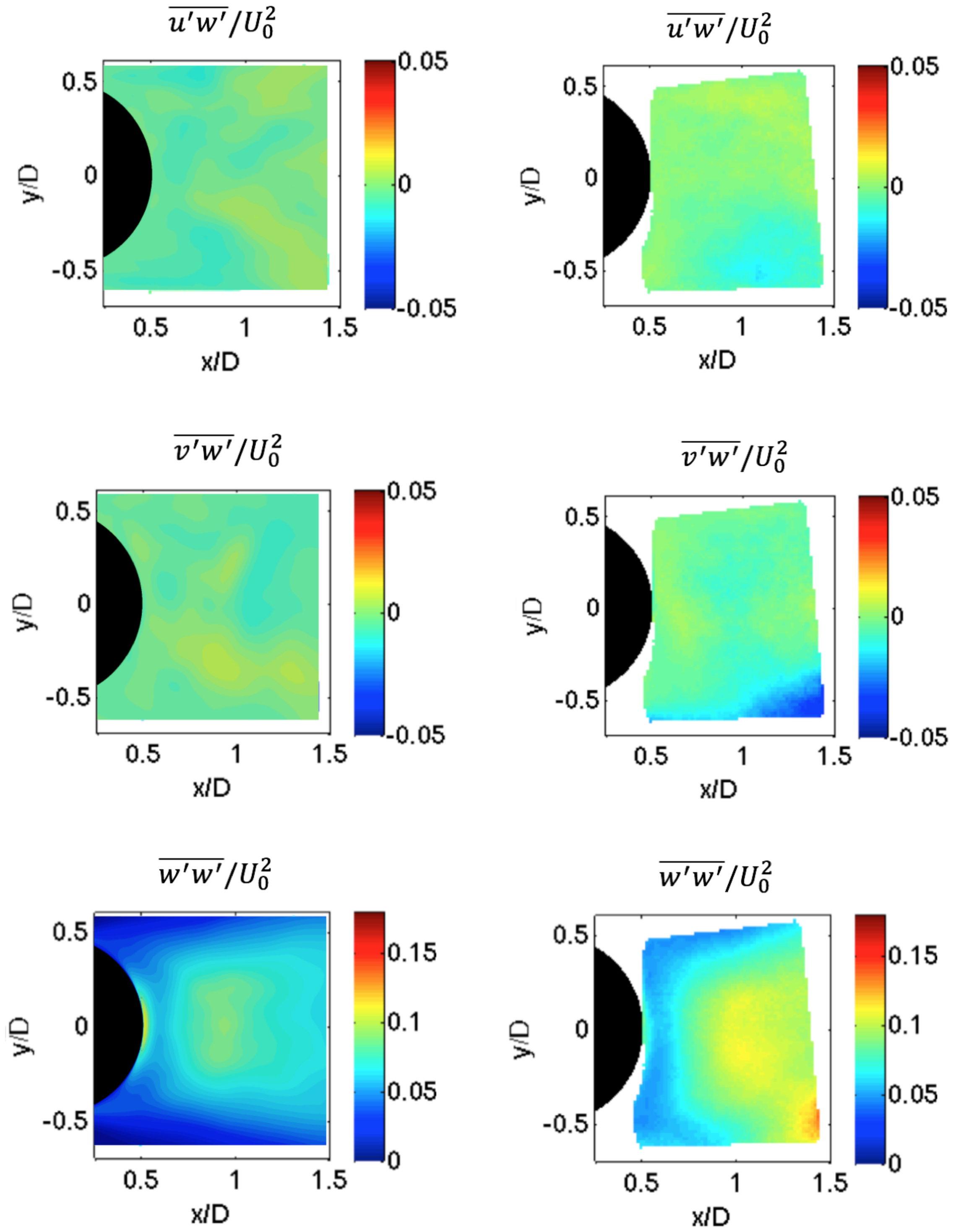

Figure 6.20 (cont.): Reynolds stress components from simulations and experiments

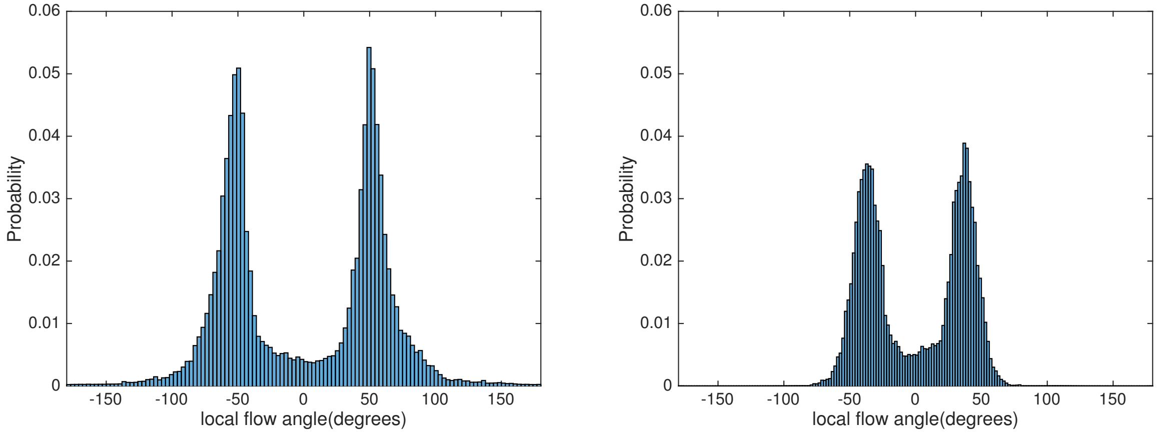

(a) 2D

(b) 4D

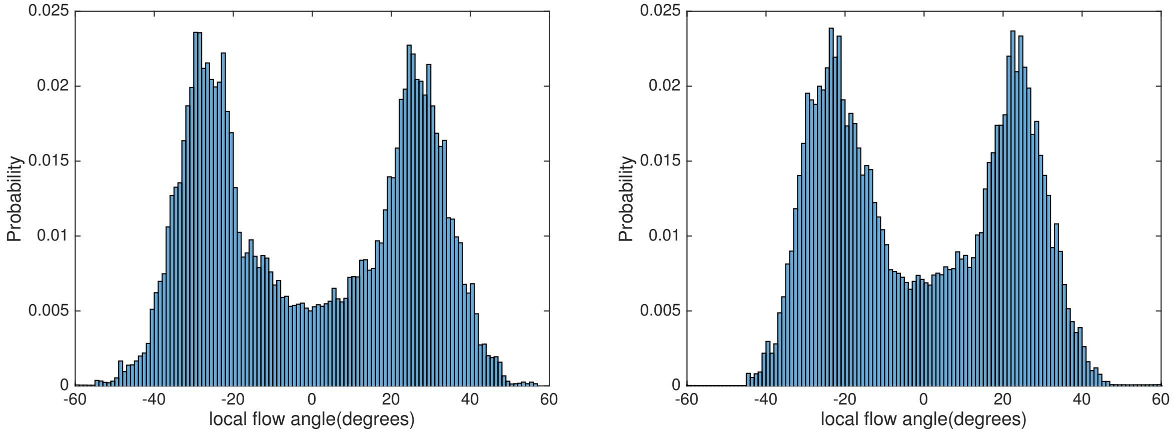

(c) 8D

(d) 10.7D

Figure 6.21: Local flow angle distribution in cylinder wake

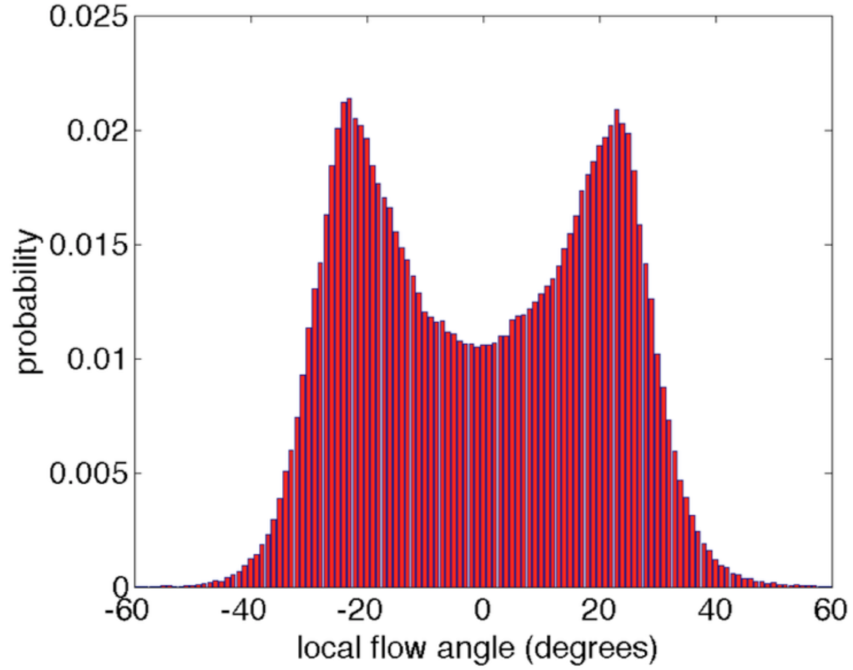

Figure 6.22: Flow angle distribution 10D downstream of cylinder center [76]

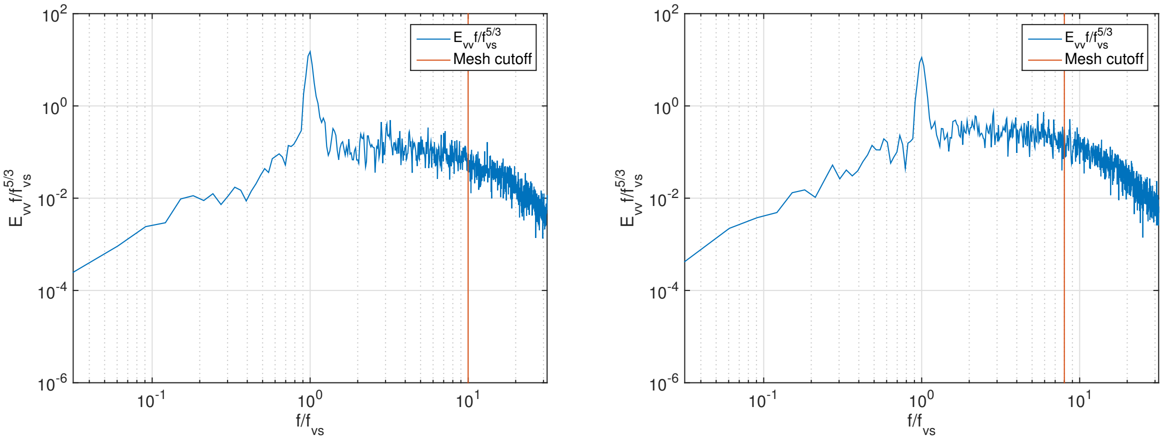

(a) 0.55D (b) 0.75D

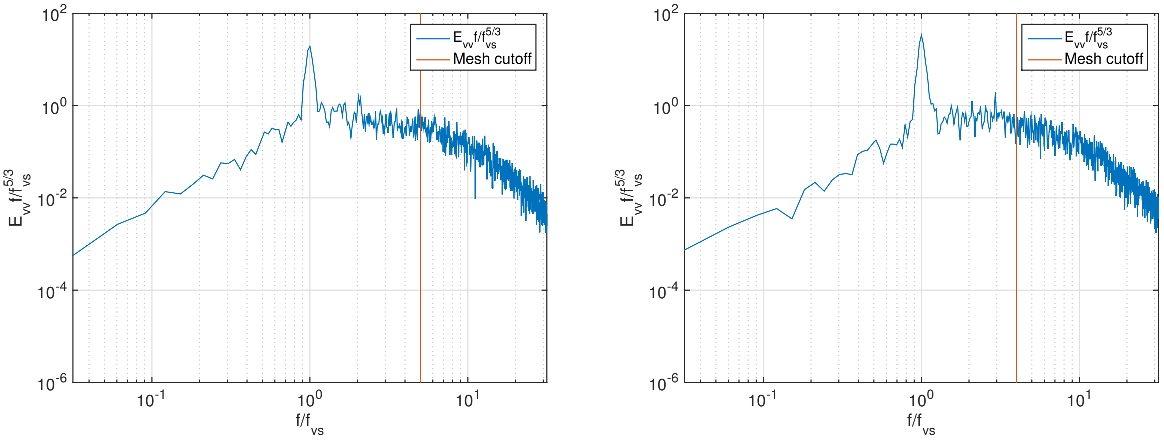

(c) 1D (d) 1.25D

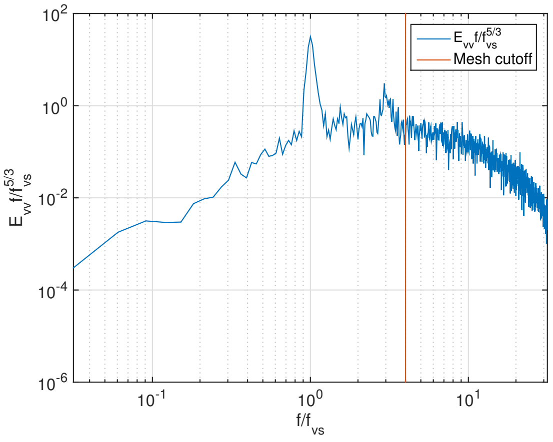

(e) 1.5D

Figure 6.23: Compensated transverse velocity spectrum on cylinder wake centerline

Chapter 7

Numerical Study of Unsteady Boundary Layer of Wind Turbine Airfoils in Cylinder Wake

The cylinder flow analysis presented in last chapter demonstrated the ability of our transition hybrid model in predicting flow features such as laminar separation and transition. With sufficiently refined mesh, the turbulence energy was resolved down to the level of 10 times the eddy shedding frequency and maintained downstream towards the airfoil position.

This chapter presents the unsteady flow dynamics on the downstream airfoil, the features of high blade loading fluctuations due to unsteadiness and transitional boundary layers are of interest in the fluid dynamics of full-scale wind turbine blades, making the surrogate problem a comprehensive test case for model development and validation.

7.1 Problem Setup

The computational domain is modified from the cylinder-only mesh, the NACA63215b airfoil is introduced $10.7D$ downstream from the circular cylinder center. The airfoil is aligned with the flow (0° AoA) and $4in.(10.16cm)$ in chord length c. The domain size is kept the same as the cylinder-only case in transverse (y) and spanwise (z) direction (table 4.2), which also matches the experimental test section measurements. The streamwise (x) direction is further extended by $50cm$, the outlet boundary is thus $9c$ downstream of the airfoil trailing edge, the wake from cylinder and airfoil if sufficiently recovered before reaching the outlet boundary.

7.1.1 Computation Mesh

The mesh around airfoil is refined to keep the wall-normal size at $y^+ \sim 1$. The cusped trailing edge introduces numerical difficulties due to high aspect ratio locally and numerical oscillations in the trailing edge chordwise progression destabilize the simulation. As a result, the airfoil surface mesh in chordwise direction is refined to the same level as wall-normal direction and the local aspect ratio is kept at ~ 1 (figure 7.1b). The leading edge mesh spacing is refined to $4 \times 10^{-4}m$ for improved boundary layer prediction in large pressure gradient (figure 7.1a).

Both the suction and pressure side are discretized by 165 grid points (figure 7.2), mesh in the airfoil wake expands gradually in the downstream direction until $2c$, where the streamwise grid size is $3.8 \times 10^{-3}m$. A second stage expansion starts from $2c$ until the outlet boundary at $9c$ to provide a smooth solution domain. Compare to the cylinder-only case, which has total grid of 2.77M, the total cell counts 9.8M in the full-model case (figure 7.3),

A similar mesh is made for the airfoil in clean flow, the only difference is the removal of the upstream cylinder (9M total cells).

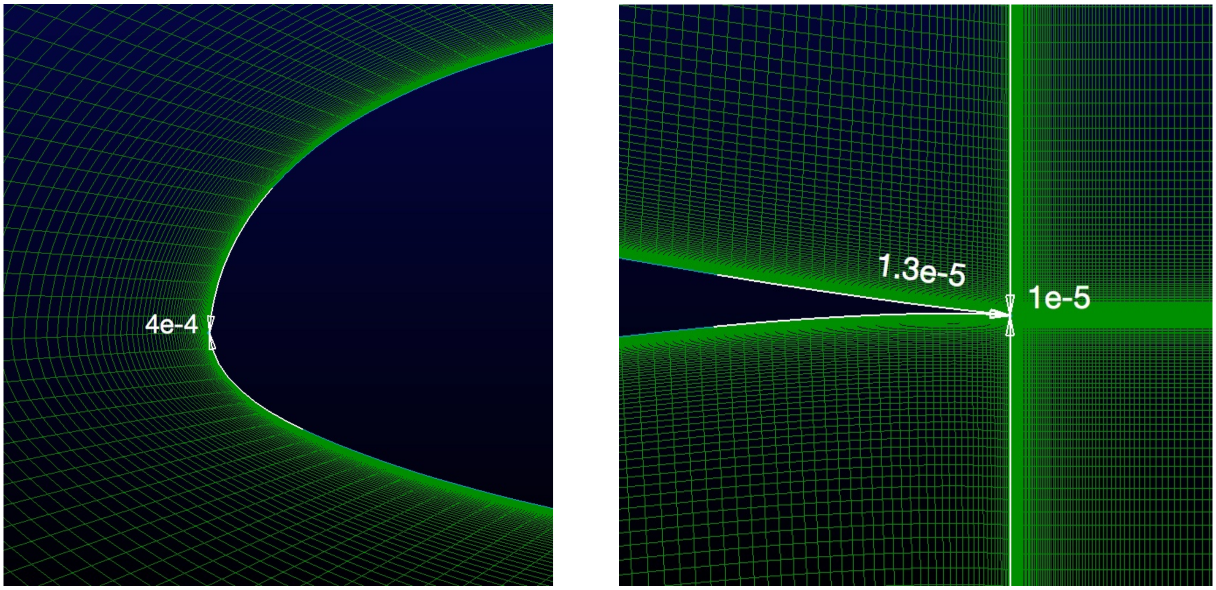

(a) Leading edge grid spacing

(b) Trailing edge grid spacing

Figure 7.1: Airfoil leading and trailing edge grid refinement

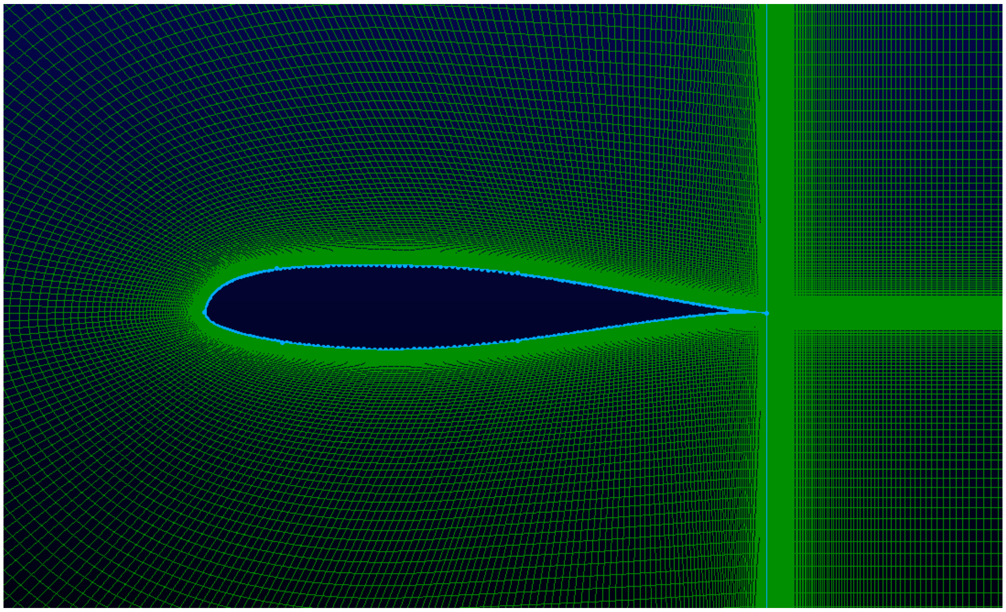

Figure 7.2: Mesh around NACA63215b airfoil

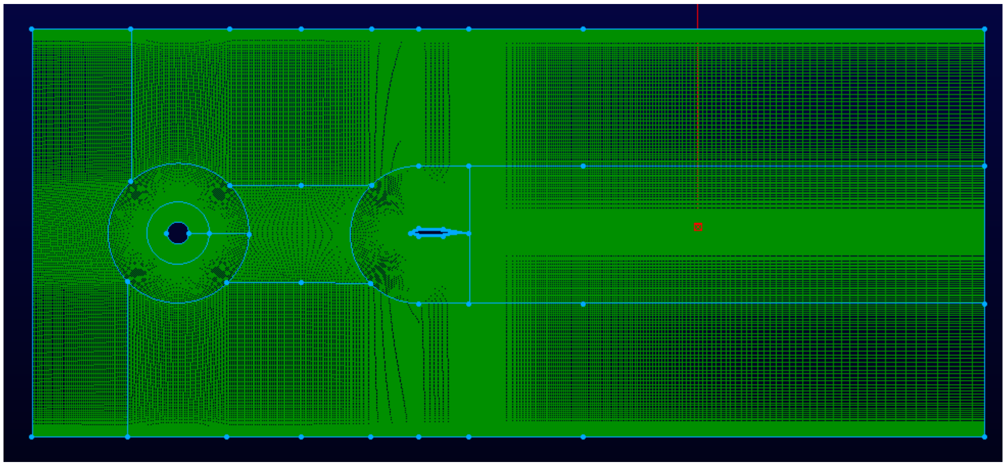

Figure 7.3: Computational domain of full model

7.1.2 Boundary Conditions and Numerical Schemes

All boundary conditions are kept same as in the cylinder-only case, the newly added airfoil is set to have the *wall* boundary condition as the cylinder, the details of the setup in OpenFOAM is shown in table 6.1.

Similarly, the spacial and temporal numerical schemes are identical to the last case, only the convergence criteria inside each time is modified to balance the accuracy and simulation time.

7.2 Results and Analysis

The unsteady airfoil flow is analyzed and presented in this section. The periodic and highly unsteady inflow impinges on the airfoil creates complex boundary layer dynamics which also exist in real turbine blades inside the upstream turbine wake.

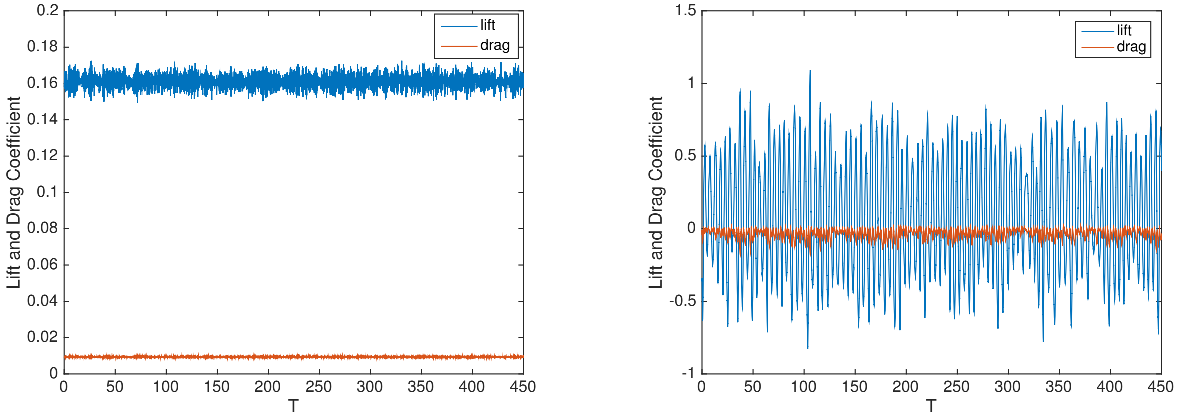

(a) Clean flow

(b) Cylinder wake

Figure 7.4: Lift and drag coefficients of the airfoil in clean flow and cylinder wake

7.2.1 Instantaneous Flow Field

Due to the periodic nature of the cylinder wake, the boundary layer response on the airfoil also shows periodic dynamics. The periods of the boundary layer dynamics is obtained from the lift and drag coefficients and several other flow fields are analyzed at multiple phases within one cycle. With the downstream airfoil, the cylinder shedding frequency increases from $132Hz$ to $137Hz$, the existence of downstream airfoil alters the vortex shedding by 3.6%. Our wind tunnel experiments did not test the cylinder flow in the full-model setup.

Airfoil lift and drag

The lift and drag history on the airfoil in both clean flow and cylinder wake is shown in figure 7.4. The non-dimensionalized time $T = tU_0/D$ and $t = TD/U_0 = 0.66s$ for $T = 450$, the initial transient is neglected from all statistics.

The mean and RMS of C_l and C_d for both cases and xFoil result are summarized in table 7.1. Airfoil in clean flow shows negligible fluctuations in the force coefficient, mean value matches the RMS value. In contrast, airfoil in cylinder flow experiences significant oscilla-

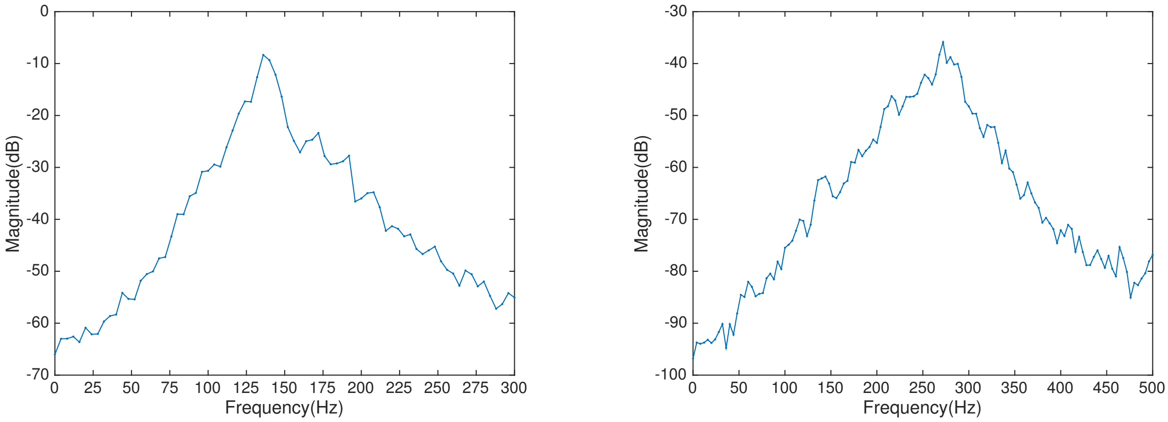

(a) Lift coefficient spectrum

(b) Drag coefficient spectrum

Figure 7.5: Lift and drag coefficients spectrum of the airfoil in cylinder wake

tions, the RMS values of both lift and drag are significantly higher than the corresponding mean value.

Table 7.1: Mean and RMS force coefficient of airfoil

	C_l mean	C_l RMS	C_d mean	C_d RMS
Clean flow	0.16	0.16	0.016	0.016
xFoil	0.17	/	0.015	/
Cylinder wake	0.10	0.43	-0.026	0.042

The spectrum of the lift and drag coefficient is plot in figure 7.5, the lift fluctuation coincide with the cylinder vortex shedding at $137Hz$ and the drag force fluctuation is exactly twice the rate of the lift force. We conclude that the periodic vortex shed from cylinder is the main driver of the unsteady flow around airfoil.

Pressure distribution

Without the cylinder, the simulation predicts the airfoil boundary layer separation at $x/c = 52\%$ and $x/c = 48\%$ on suction and pressure side respectively and flow reattaches at

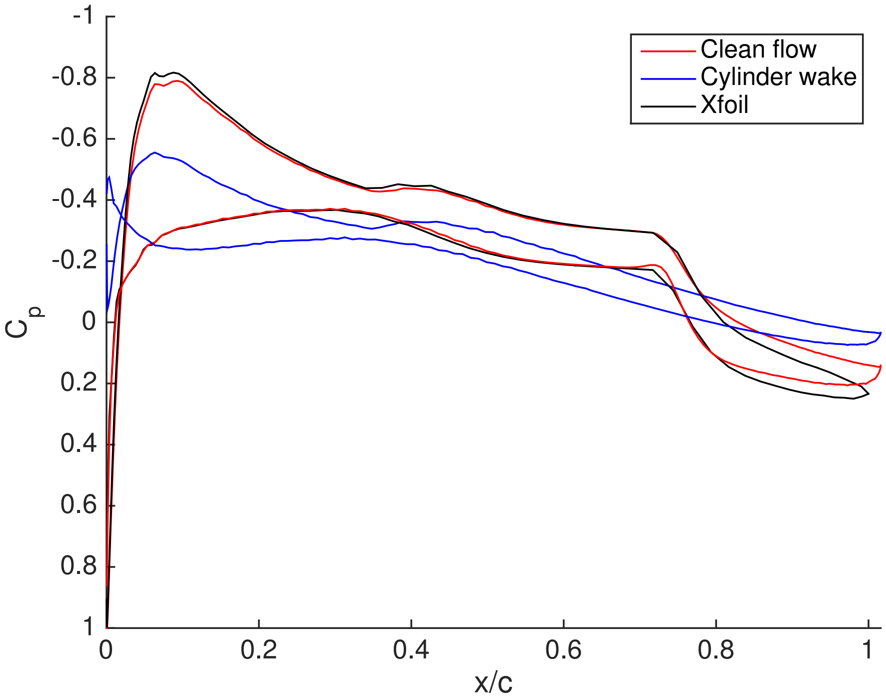

Figure 7.6: Pressure distribution on airfoil surface

$x/c \sim 70\%$ on both sides. Figure 7.6 is the predictions of mean pressure distribution on the NACA63216b airfoil from simulation results of airfoil in clean flow and cylinder wake. The pressure distribution in clean flow agrees with Xfoil data from leading edge to the reattachment locations. The CFD data predicts lower pressure gradient than Xfoil data in the turbulent boundary layer after reattachment.

The instantaneous pressure distribution on airfoil in cylinder wake within one cycle is subdivided into 8 phases (figure 7.7), the variation of the pressure coefficient is at its maximum near the leading edge, the lift variations are dominated by the pressure distribution before quarter chord. In half way within a cycle, the pressure distribution on suction and pressure side switches, which leads to negative lift at the same magnitude as the positive lift.

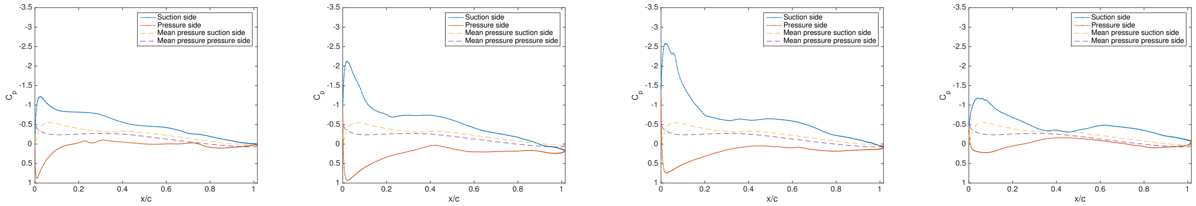

(a) Phase 1 (b) Phase 2 (c) Phase 3 (d) Phase 4

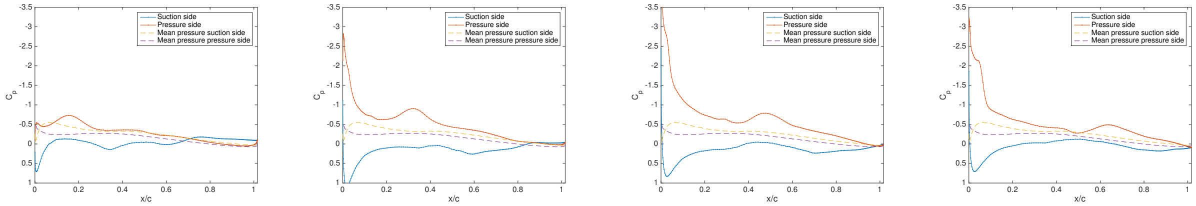

(e) Phase 5 (f) Phase 6 (g) Phase 7 (h) Phase 8

Figure 7.7: Pressure distribution on airfoil in cylinder wake over one shedding cycle

Blending function of hybrid model and eddy viscosity

The blending function F_{DDES} is used to control TKE generation as mentioned in last chapter. Inside the boundary layer, where the specific dissipation ω is high, F_{DDES} remains value of 1 (equation 6.10) and the original RANS formulation is preserved (see figure 7.8). Outside the boundary layer $F_{DDES} > 1$ in the region of fine mesh (i.e. small Δ) and high TKE (inside eddies).

From figure 7.8, the distribution of F_{DDES} is concentrated around the cylinder and airfoil where the mesh is refined for transition prediction. As the grid size expands from cylinder surface to $\sim 1.5D$ downstream of the rear stagnation point, F_{DDES} decreases to ~ 1.4 in the outer regions of the eddies, which indicates extra 40% modeled TKE is destructed compared with RANS model. In the core of the eddies, where local TKE is high, F_{DDES} remains ~ 2. As the vortex interacts with the airfoil, where mesh is refined again, the eddies are stretched around the leading edge and F_{DDES} resumes to the same level as in the cylinder near wake.

Figure 7.9 is the instantaneous eddy viscosity distribution around airfoil in the cylinder wake. The alternating vortex structures are visible on either side of the airfoil, notice there is

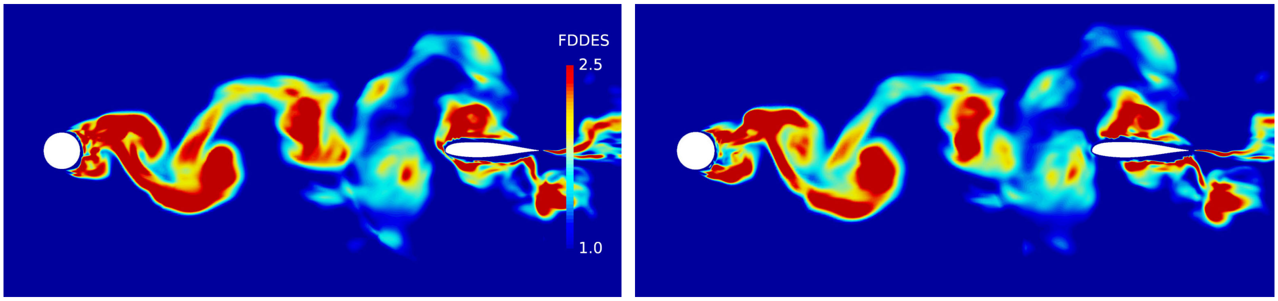

(a) Phase 1

(b) Phase 2

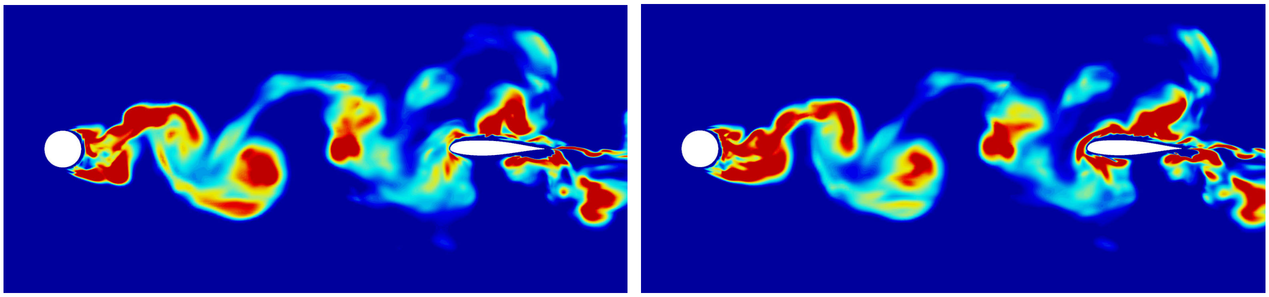

(c) Phase 3

(d) Phase 4

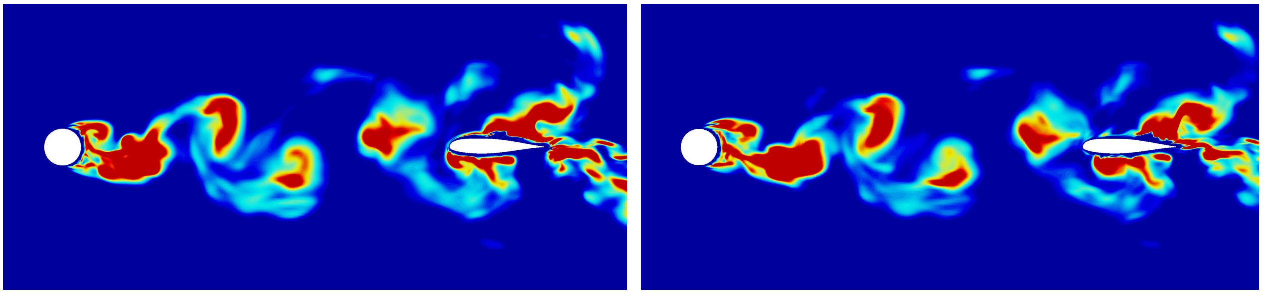

(e) Phase 5

(f) Phase 6

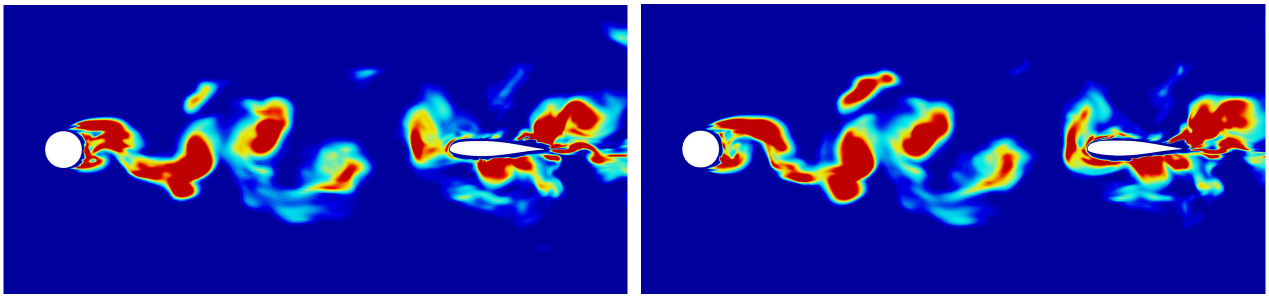

(g) Phase 7

(h) Phase 8

Figure 7.8: Blending function F_{DDES} around airfoil in cylinder wake over one shedding cycle

a shear layer leaving the airfoil trailing edge which interacts with the cylinder vortices. There is a strong correlation between F_{DDES} and ν_{sgs} outside the boundary layer. F_{DDES} reaches maximum in the center of the vortices and the eddy viscosity, which is proportional to TKE, is attenuated (e.g. see suction side of phase 1 and 2 near leading edge). The rotation flow interacts with the airfoil boundary layer and cause local increase in TKE and eddy viscosity (phase 4-6), the blending function F_{DDES} follows the same trend as its definition suggests in equation 6.10. By the time the eddy reaches trailing edge, the attenuation effect of F_{DDES} decreases the eddy viscosity significantly (phase 8).

Vortex structures

Two eddies shed from cylinder with one shedding cycle as show in figure 7.10. Inspecting the fluid force acting on the airfoil, we found the cylinder vortices are the main driver of the airfoil unsteadiness. The normalized vorticity field $\overline{\omega_z} = \omega_z/(U_0/D)$ is concentrated within the Karman vortex and the width of the wake grows as the they travels downstream, the coherent turbulence structure breaks up and stretched as it interacts with the airfoil boundary layer (figure 7.11).

LM turbulence intermittency and skin friction

The LM turbulent intermittency field gives a clear indication of laminar boundary layer separation, the airfoil boundary layer in clean flow remains laminar before separating and the transition location after separation is clearly visible from LM intermittency distribution on airfoil surface as shown in figure 7.12a. From figure 7.12a the flow transition initiates on both sides approximately $x/c = 0.6$, which is confirmed by the skin friction distribution (figure 7.12b). The separation bubble extends $0.1c$ downstream of the transition point and the boundary layer flow reattaches at $x/c = 0.7$ on both sides.

Airfoil boundary layer inside cylinder wake is fully turbulent and attached as shown by the skin friction (figure 7.13). The surface LM intermittency remains low (< 0.1 over 90% of the airfoil surface), which indicates the existence of laminar viscous sublayer in the attached boundary layer. Experiments looked at boundary layer parameters from $x/c = 0.3$ to $x/c = 0.8$ at $0.1c$ interval and found it remained attached and turbulent at all locations, which confirms our observation from simulation.

Boundary layer profiles

The instantaneous velocity profile on airfoil over one shedding cycle is plotted from $x/c = 0.3$ to $x/c = 0.8$ in figure 7.14, 7.15 and 7.16. No reverse flow is observed in the vicinity of the wall at all positions, and therefore no boundary layer separation at all time. Compare the profiles at two extreme positions $x/c = 0.3$ and $x/c = 0.8$, there are larger kinks in the profiles at $x/c = 0.8$ in certain phase than at $x/c = 0.3$, which corresponds to the low-momentum regions outside boundary layer created by the passage of vortices. It is noticeable that the boundary layer has thickened as flow travels downstream. In order to inspect the variation of U_x, the mean velocity is subtracted from the instantaneous profile as shown in figure 7.15. The fluctuation profiles exhibit oscillatory behavior that resembles the Stokes flow, the vertical velocity component U_y shows similar behavior as in figure 7.16. We also noticed a phase lag between each station, which is most discernible between $x/c = 0.3$ and $x/c = 0.8$, it will be inspected further in the section of phase-averaging.

7.2.2 Mean Flow Field

Mean velocity and pressure field of airfoil in clean flow and cylinder wake are presented and compared with experimental data in this section.

Mean velocity field and streamlines

Mean flow velocity around airfoil in clean flow and cylinder wake is extracted from both experimental and simulation data, the PIV data is only available on the suction side of the airfoil. Flow reattaches on both side of airfoil in clean flow at $x/c = 0.7$, which is marked by the sudden change in mean velocity field (7.17).

The mean velocity magnitude reduces in cylinder wake, figure 7.18 gives the mean streamwise velocity profile at one chord length upstream of the airfoil leading edge, both the momentum defect and blockage effects are clearly visible in the case of the cylinder wake. The mean flow rate measured between $\pm 0.1c$ at the same streamwise location are $5.16m^2/s$ and $4.82m^2/s$ per unit span in clean flow and cylinder wake respectively.

The velocity fluctuations are averaged out in the mean field and the from figure 7.19, both cases presents smooth streamline distribution on and around airfoil.

Mean and RMS pressure distribution

The acoustic field from incompressible LES simulation is usually calculated through integral approach, e.g. Lighhill's acoustic analogy. For rigid surface low-Mach-number flow the Curle's equation is derived from simplifying the original Lighthill's equation. The dipole acoustic source is generated from the integration of surface pressure variations, i.e. lift and drag on airfoil. The quadrupole source is calculated from volume integration of the stress tensor, i.e. the unsteadiness. In the low-Mach number cases, the dipole source dominates.

The distribution of RMS airfoil surface pressure coefficient gives the magnitude of the surface pressure variations, which is a direct measurement of the dipole acoustic source strength. From figure 7.20, the leading edge produces the most lift and acoustic source strength, the lift force per chord length remains relatively constant from $x/c = 0.4$ to $x/c = 0.8$. Both the lift and pressure RMS reach zero at the trailing edge.

Figure 7.21 compares the RMS pressure distribution around the airfoil in clean flow and cylinder wake. The RMS field is close in magnitude in two cases, while the strength distribution extends further in transverse direction, and the most intense regions moved further downstream in the case of cylinder wake. Similar behavior is observed in the pressure coefficient fluctuation distribution in figure 7.22. We can conclude that the strength of acoustic field is comparable in two cases, while the distribution of the sources is significantly altered by the cylinder wake.

Mean TKE distribution

The mean modeled TKE in the two cases differs greatly in terms of intensity and distribution as shown in figure 7.23, in both case the TKE field is normalized by U_∞^2. TKE starts to grow downstream of the laminar separation point on the airfoil in clean flow case, the distribution is concentrated inside the separated boundary layer, which confirms that the RANS model is preserved.

For the airfoil in cylinder wake, the boundary layer is the most turbulent at the leading edge, the TKE diffuses outwards the boundary layer as traveling downstream and the peak at the trailing edge is caused by the free shear layer sheds from both sides of the airfoil.

7.2.3 Flow Statistics

Airfoil flow statistics is presented in this section, including boundary layer parameters, Reynolds stress, turbulence energy spectrum and phase-averaged boundary layer profiles.

Mean boundary layer statistics

The mean boundary layer profile is plotted in the wall-normal direction of airfoil surface from $x/c = 0.3$ to $x/c = 0.9$ at $0.1c$ interval (figure 7.24). From figure 7.24a we noticed there is reverse flow in the station $x/c = 0.6$ and 0.7, flow attaches at $x/c = 0.8$ and 0.9. No separation in the mean velocity profile on the airfoil in cylinder wake (figure 7.24c).

The boundary layer thickness δ is defined at the 99% of edge velocity. For the clean flow case, the profile curves show clear turning points where the velocity gradient in the vertical direction is zero (figure 7.24a and 7.24b), it is used as the edge of boundary layer in this study. Figure 7.25 compares δ, displacement thickness δ^* and momentum thickness θ on the airfoil with experimental data. The boundary layer thickness δ grows monotonically in chordwise progression, the difference between experimental data varies from 8% to 50% and the numerical prediction is always higher than experiments. The difference in momentum thickness θ from station $x/c = 0.4$ and 0.7 is within 15%, except at $x/c = 0.3$ and 0.8 where both numerical predictions are over 50% higher. The displacement thickness δ^* from simulation grows rapidly starting from $x/c = 0.4$ and is twice as thick at station $x/c = 0.7$ compared with experiment. The reverse flow as shown in figure 7.24a contributes to fast growth of δ^* and as the flow reattaches the displacement thickness reduces in station $x/c = 0.8$.

In contrary, for the airfoil in cylinder wake, the velocity magnitude continues to increase beyond $Y/c = 0.5$ and finally converged to $26m/s$ outside cylinder wake. Therefore, determine the boundary layer edge requires ad hoc definition of edge velocity and not calculated in this study.

Reynolds stress field

Figure 7.27 is a comparison of three Reynolds stress components around airfoil in clean flow, the inflow in experiment has freestream turbulence intensity of 1%. The experimental data is only available on the suction side and the PIV system resolution limited the measurement only to the flow outside the thin boundary layer. All three components have value near zero as expected in the steady inflow. The most notable feature from simulation is at approximately $x/c = 0.6$ on the pressure side, where boundary layer turns to turbulent, the normal stress components $\overline{u'u'}$ and $\overline{v'v'}$ peak in the shear layer that originates from this location.

The large fluctuations in the cylinder wake lead to significantly higher Reynolds stress around the airfoil. Part of the thicker boundary layer is captured by the PIV measurements on the suction side. The magnitude and distribution of all three Reynolds stress components from simulation agree with experimental data, however the experimental results contain more stochastic structures from the decay of cylinder wake eddies. The shear stress term $\overline{u'v'}$ peaks at leading edge due to high distortion of turbulence structures in cylinder wake, same feature is absent in the case of clean inflow.

The most noticeable features of Reynolds stress field is the redistribution of fluctuation energy between the normal stress components. The streamwise component $\overline{u'u'}$ increases significantly starting from the leading edge while the transverse component $\overline{v'v'}$ reduces at the similar rate. The redistribution of the normal stress as approaching the solid surface is an invisicid effect described by rapid distortion theory (RDT, figure 7.28). The Hunt and Graham(HG)'s results for an instantaneously appearing flat-plate [97] are rescaled with $L_{11} = 0.030m$ and $L_{22} = 0.060m$ to fit the measured data in experiments and simulations. The experimental and simulation results that represented by dot and dash lines respectively follows the same trends as the theoretical prediction with slightly higher gradient in $\overline{u'u'}$ close to the wall. According to [98], the Reynolds stress component is proportional to the correspond strain rate and the pressure fluctuation p', as the strain rate component in transverse direction reduces on airfoil surface, the transverse normal stress $\overline{v'v'}$ is redistributed to the streamwise and spanwise components. The redistribution features is absent from the clean flow case since the p' must present to initiate the mechanism [76].

The redistribution of Reynolds stress has significant effect on turbulence energy of the streamwise and transverse velocity components u and v. Details are inspected in the next section.

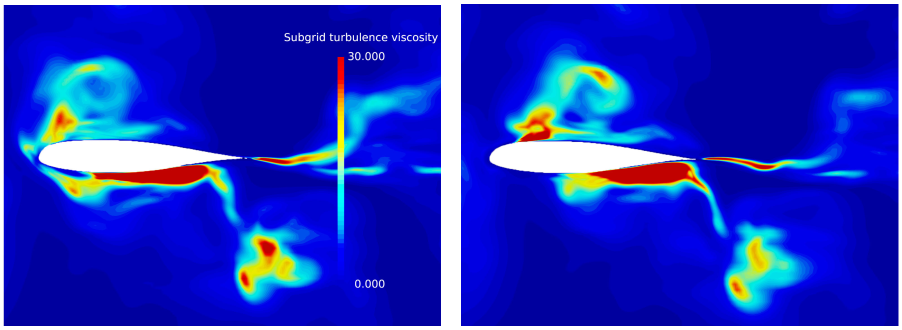

(a) Phase 1 (b) Phase 2

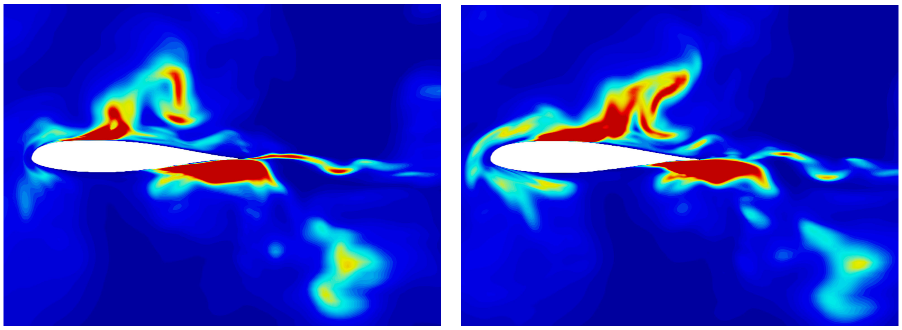

(c) Phase 3 (d) Phase 4

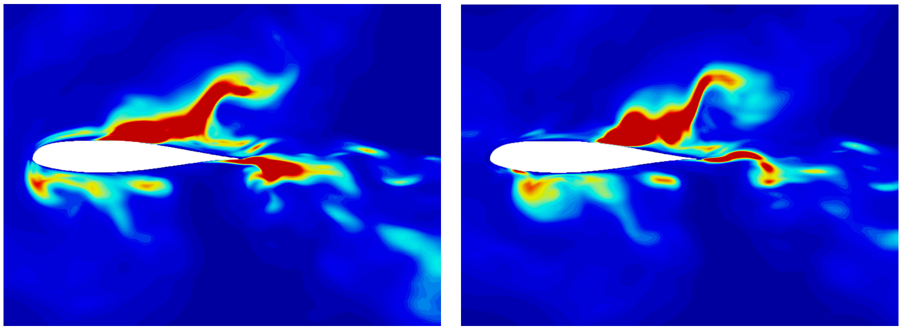

(e) Phase 5 (f) Phase 6

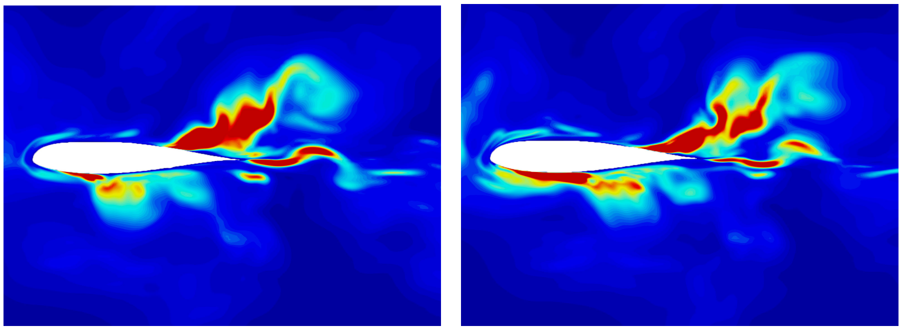

(g) Phase 7 (h) Phase 8

Figure 7.9: Eddy viscosity around airfoil in cylinder wake over one shedding cycle

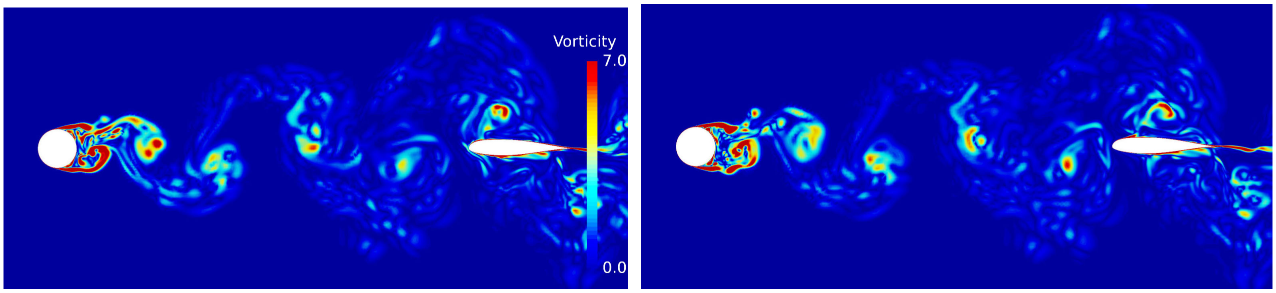

(a) Phase 1 (b) Phase 2

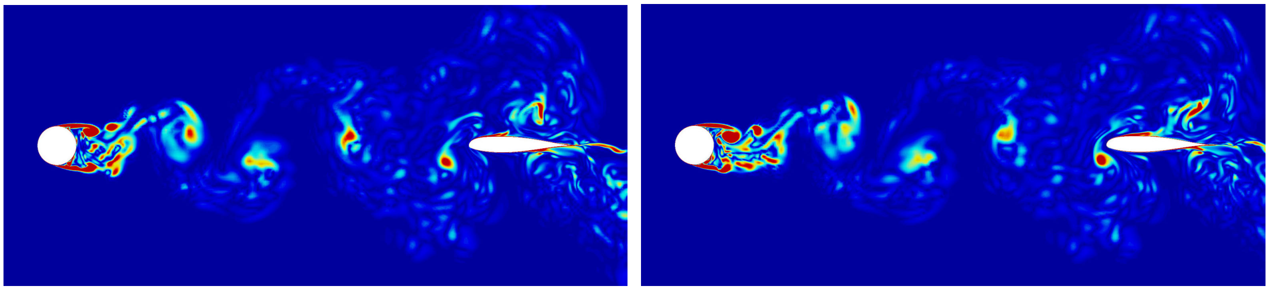

(c) Phase 3 (d) Phase 4

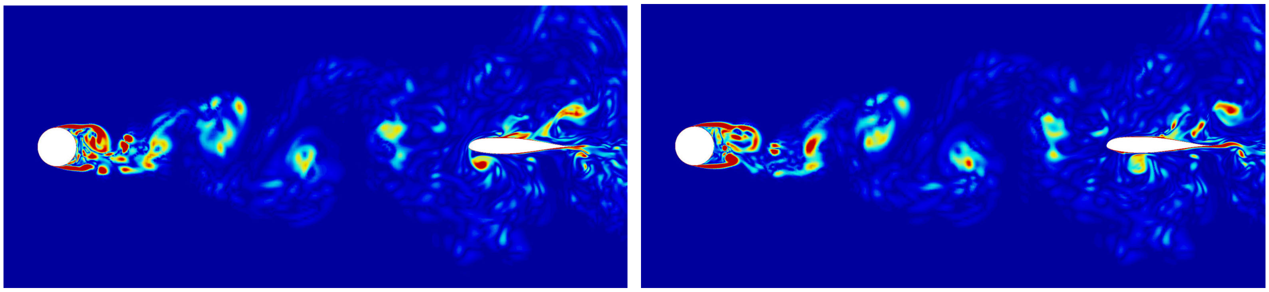

(e) Phase 5 (f) Phase 6

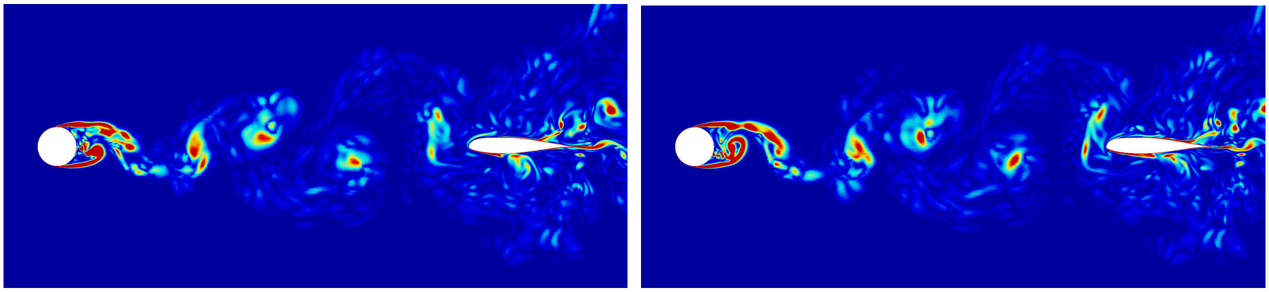

(g) Phase 7 (h) Phase 8

Figure 7.10: Spanwise vorticity from cylinder to airfoil within one shedding cycle

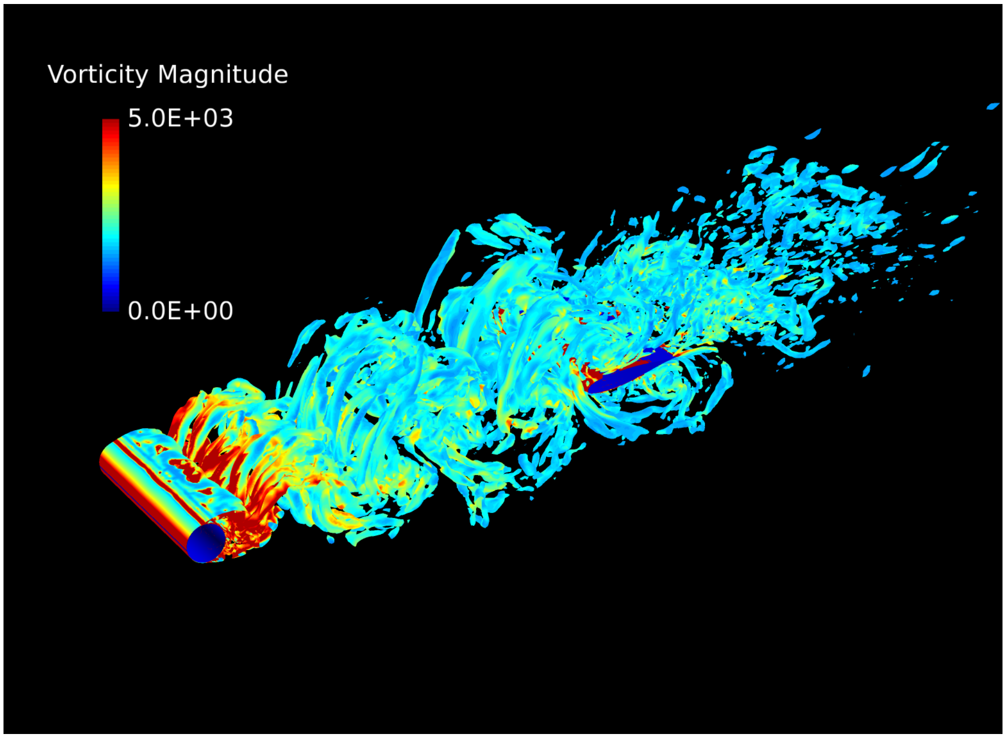

Figure 7.11: Iso-surface of Q-criterion from cylinder to airfoil

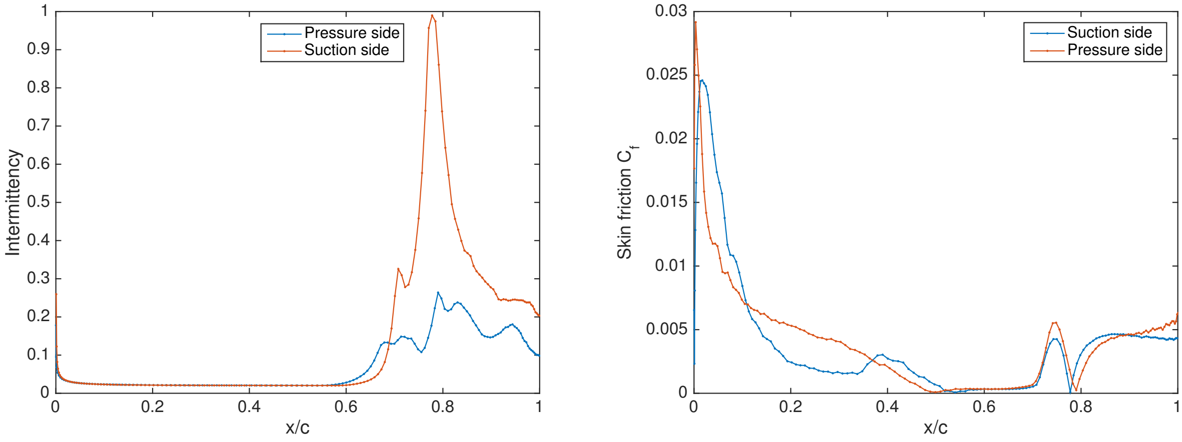

(a) LM turbulence intermittency on airfoil in clean flow

(b) Skin friction coefficient on airfoil in clean flow

Figure 7.12: Airfoil in clean flow

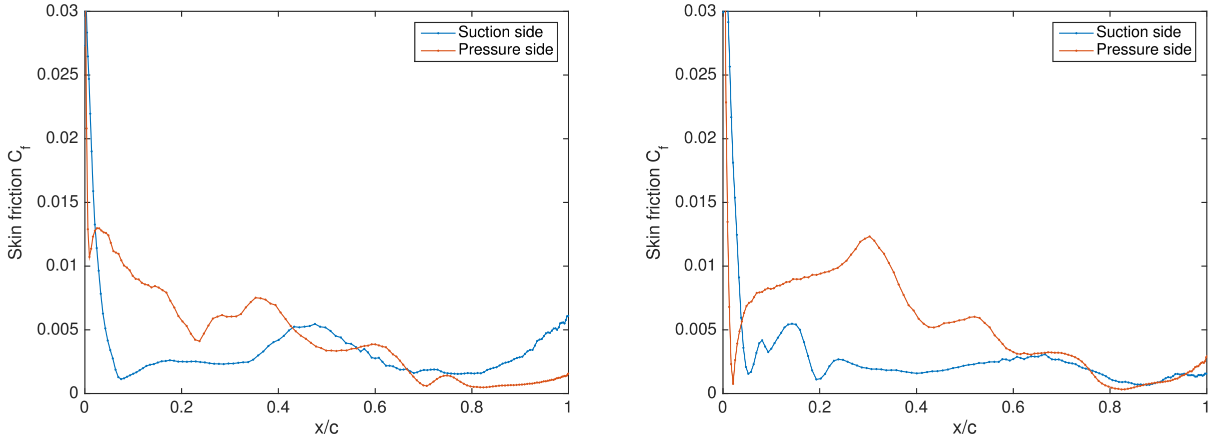

(a) Phase 1 (b) Phase 2

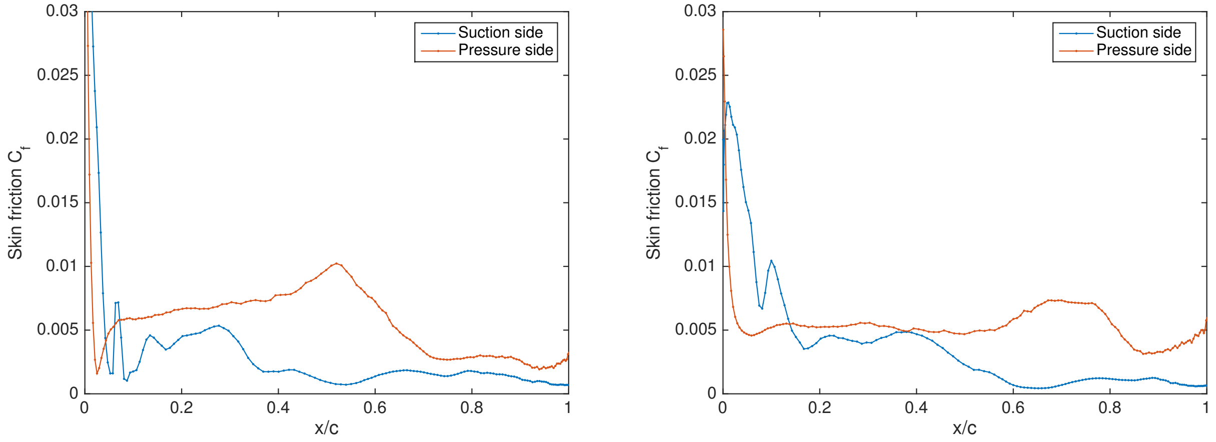

(c) Phase 3 (d) Phase 4

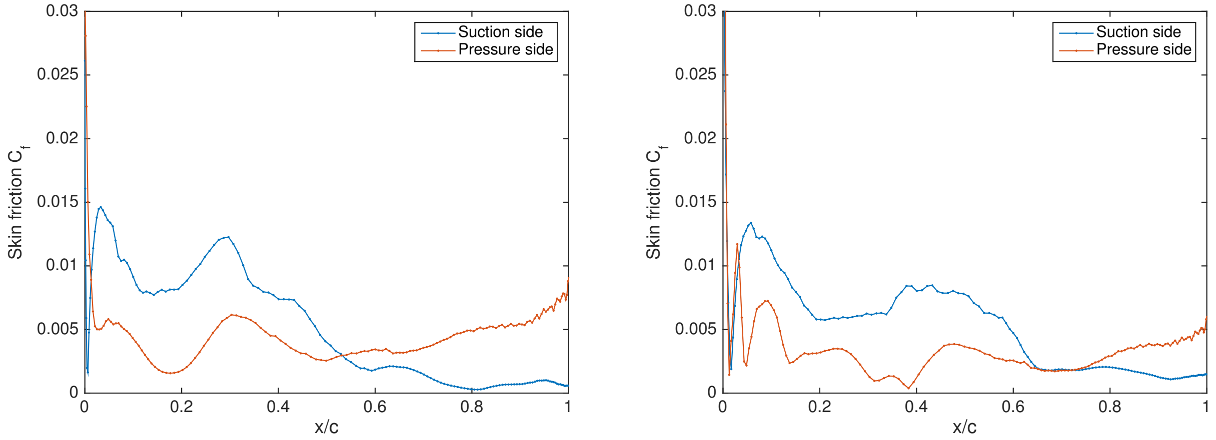

(e) Phase 5 (f) Phase 6

Figure 7.13: Skin friction coefficient on airfoil in cylinder wake within one shedding cycle

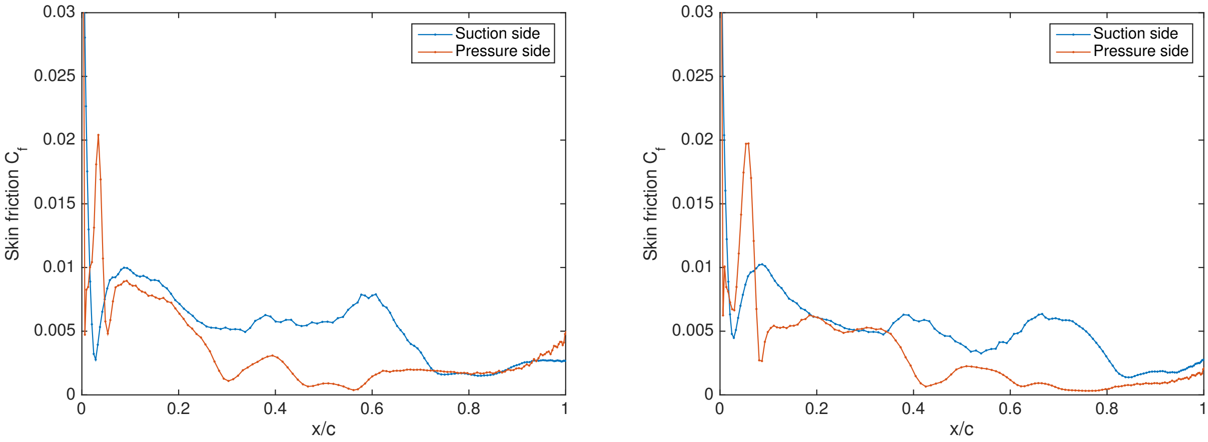

(g) Phase 7

(h) Phase 8

Figure 7.13 (cont.): Skin friction coefficient on airfoil in cylinder wake within one shedding cycle

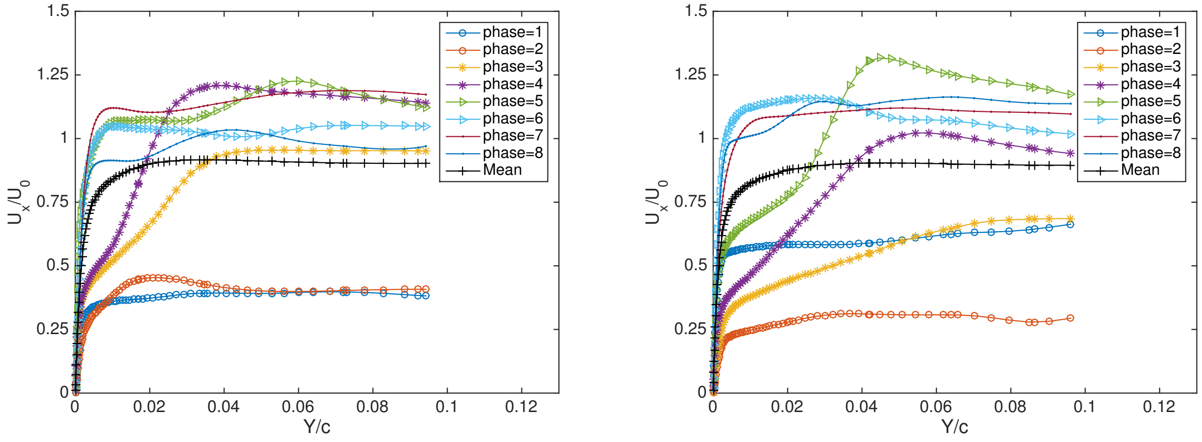

(a) $x/c = 0.3$

(b) $x/c = 0.4$

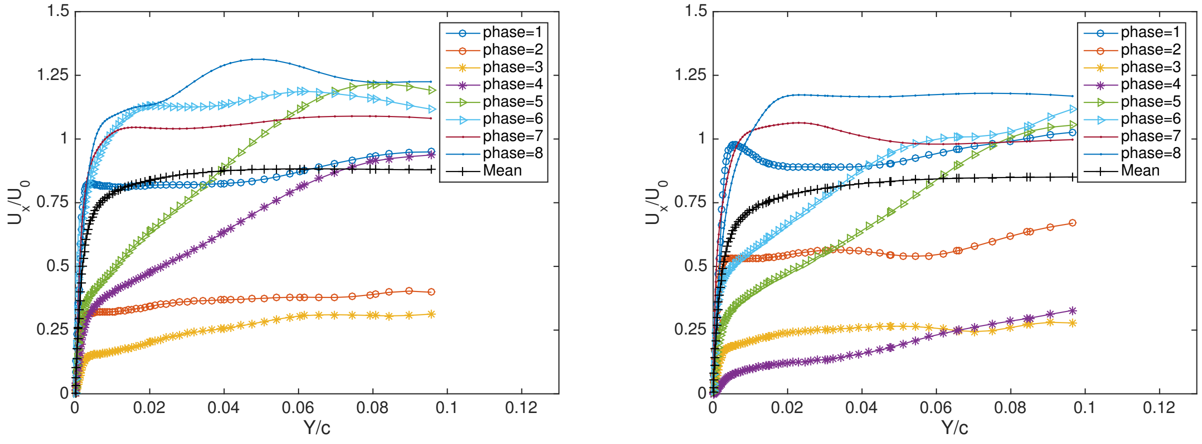

(c) $x/c = 0.5$

(d) $x/c = 0.6$

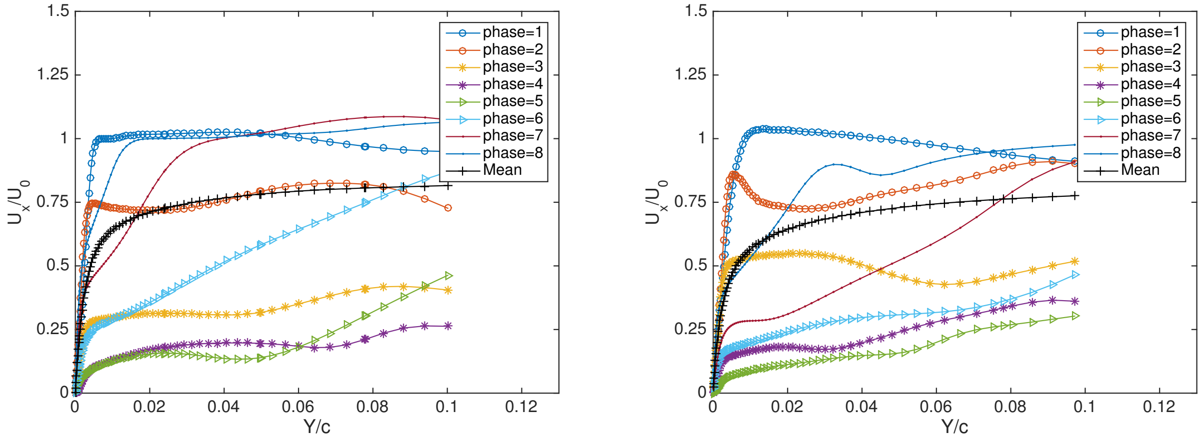

(e) $x/c = 0.7$

(f) $x/c = 0.8$

Figure 7.14: Instantaneous profile of velocity component U_x parallel to airfoil surface

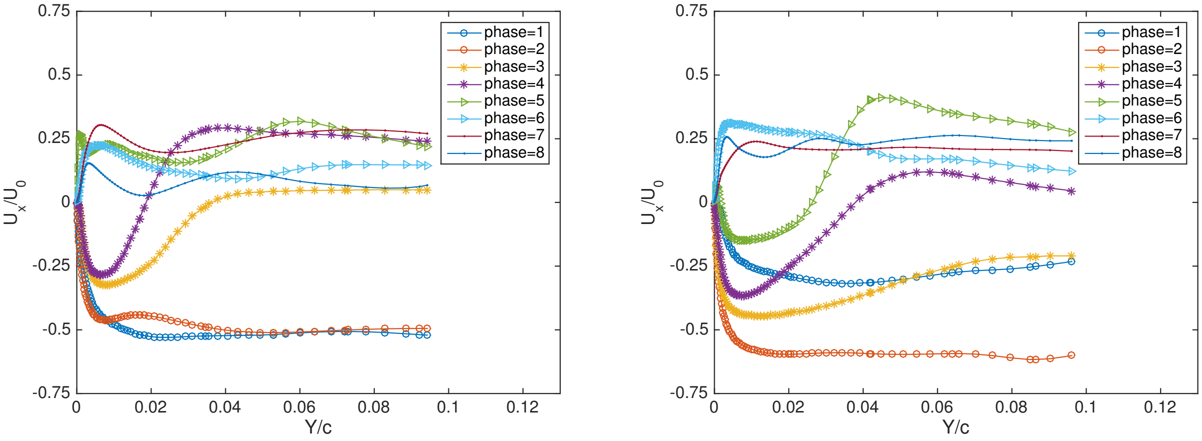

(a) $x/c = 0.3$

(b) $x/c = 0.4$

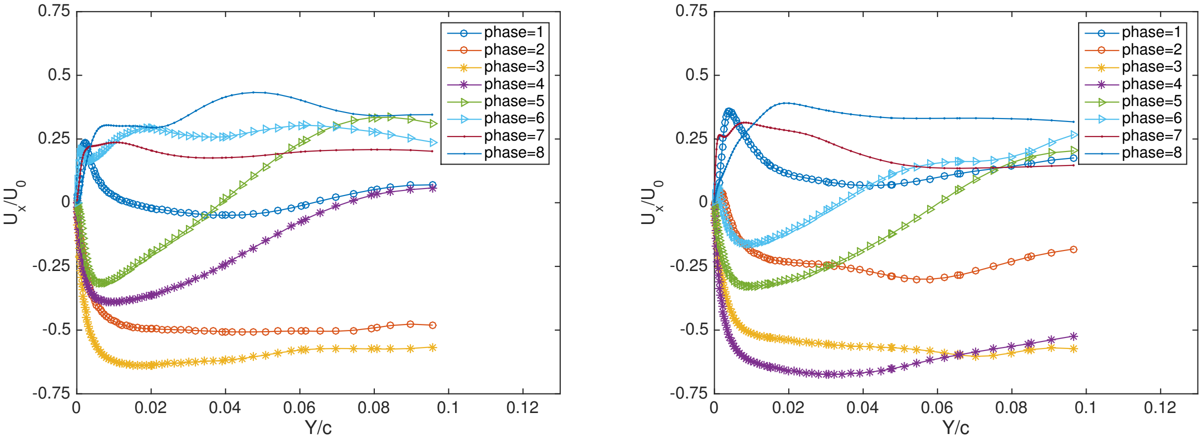

(c) $x/c = 0.5$

(d) $x/c = 0.6$

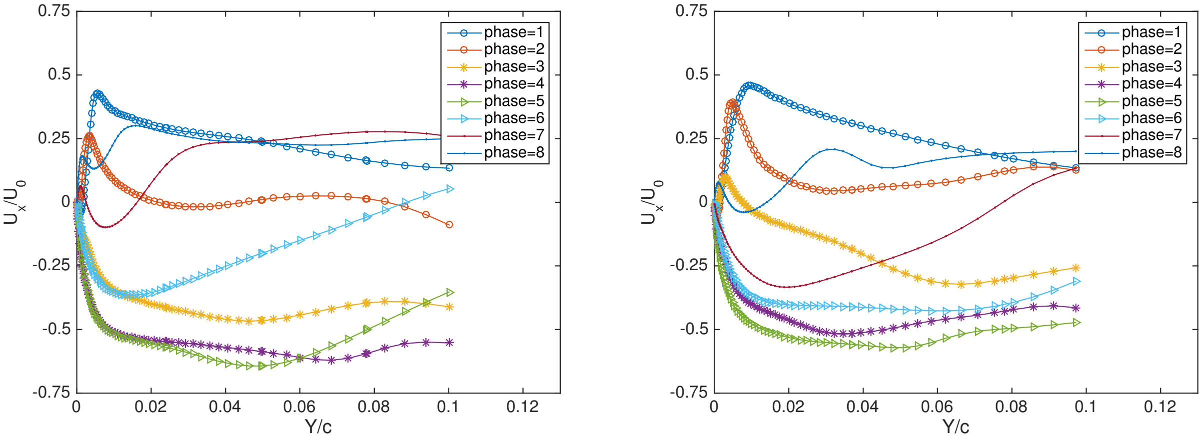

(e) $x/c = 0.7$

(f) $x/c = 0.8$

Figure 7.15: Parallel velocity component fluctuations U'_x

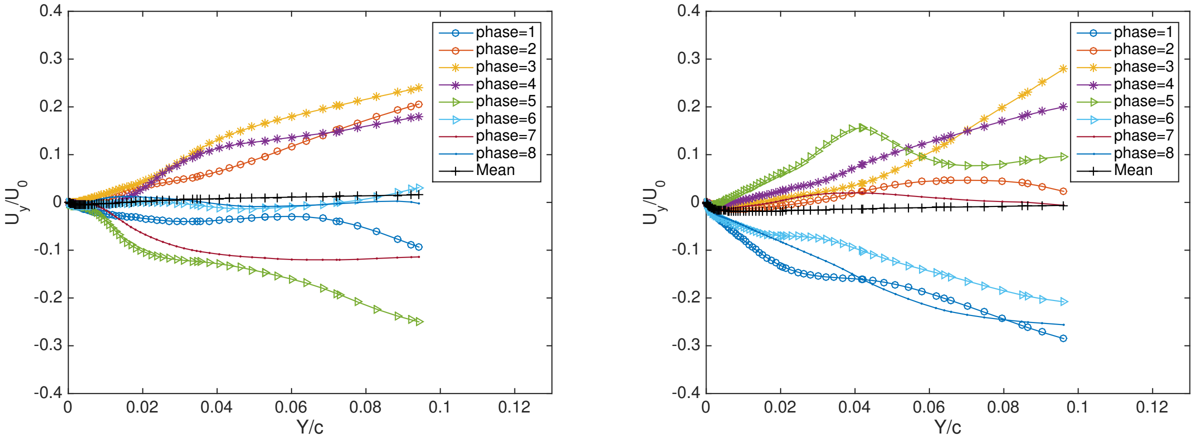

(a) $x/c = 0.3$

(b) $x/c = 0.4$

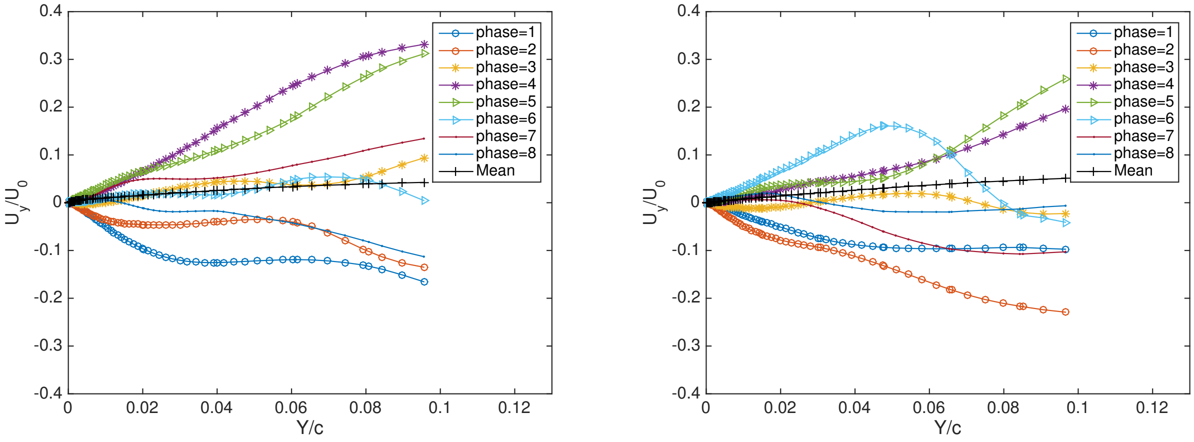

(c) $x/c = 0.5$

(d) $x/c = 0.6$

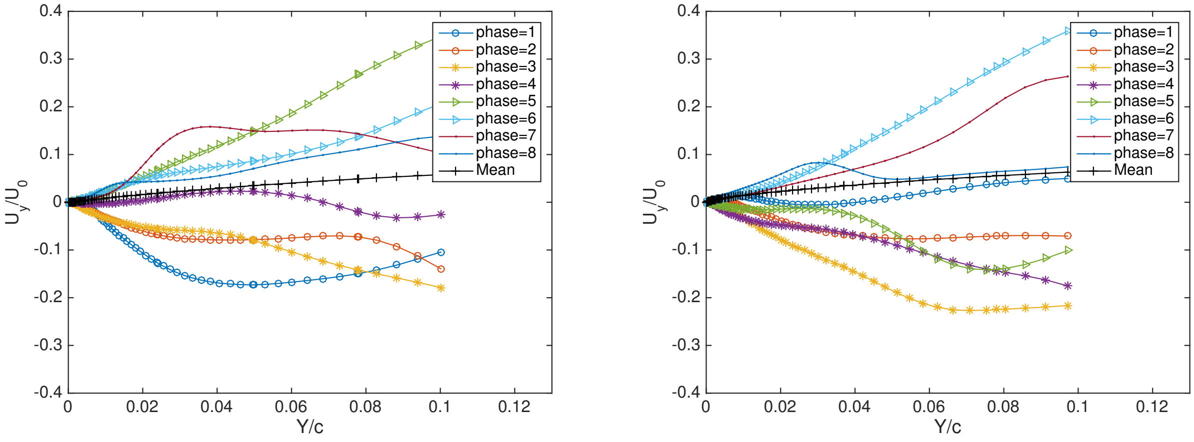

(e) $x/c = 0.7$

(f) $x/c = 0.8$

Figure 7.16: Instantaneous profile of velocity component U_y vertical to airfoil surface

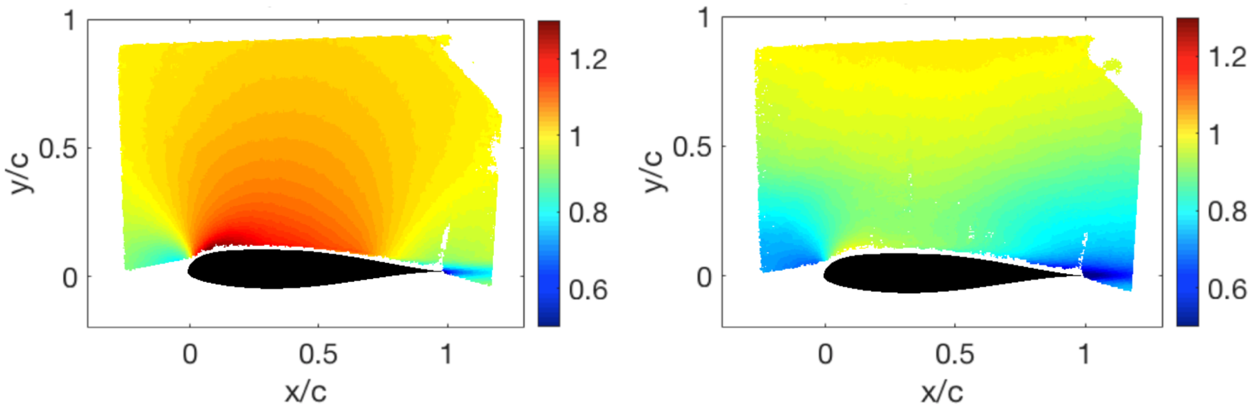

(a) Clean inflow(PIV)

(b) Cylinder wake(PIV)

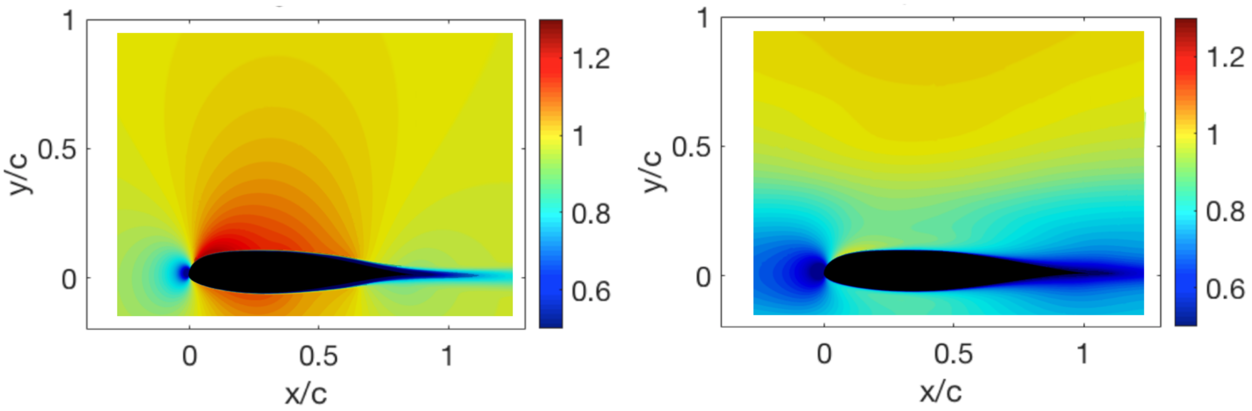

(c) Clean inflow(Simulation)

(d) Cylinder wake(Simulation)

Figure 7.17: Normalized mean velocity magnitude in clean flow and cylinder wake

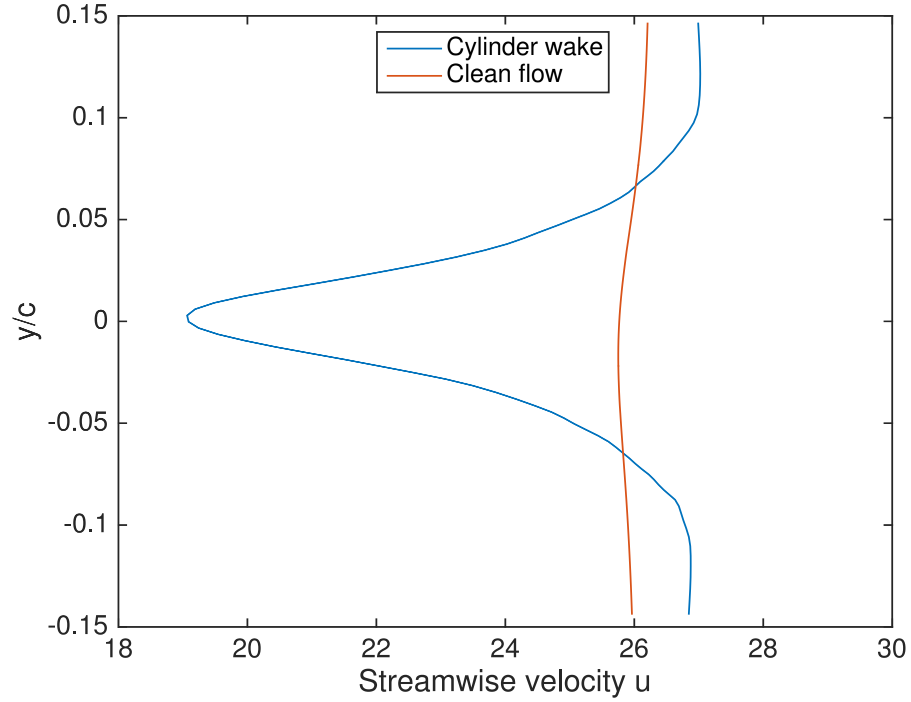

Figure 7.18: Mean streamwise velocity 1c upstream of airfoil leading edge

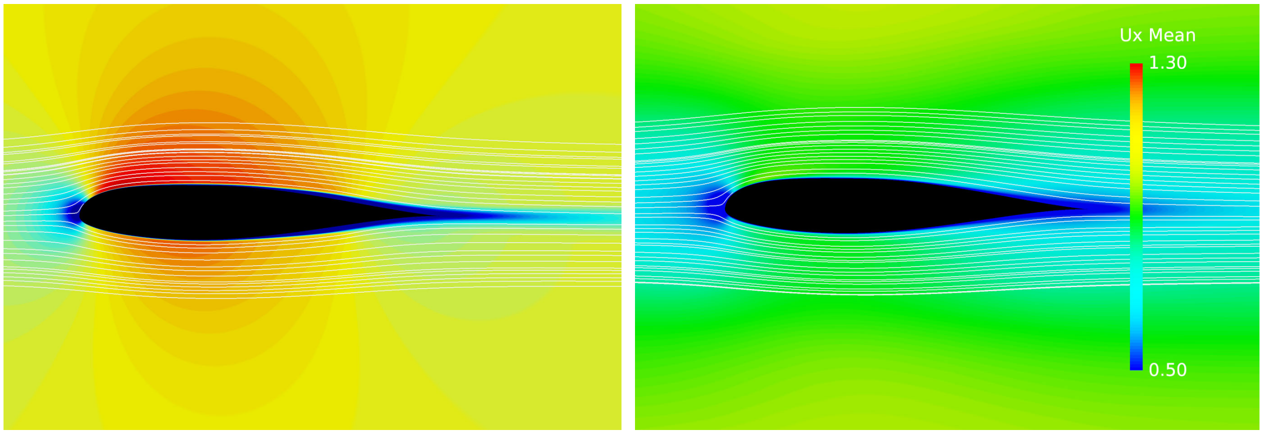

(a) Clean inflow

(b) Cylinder wake

Figure 7.19: Streamline of mean streamwise velocity

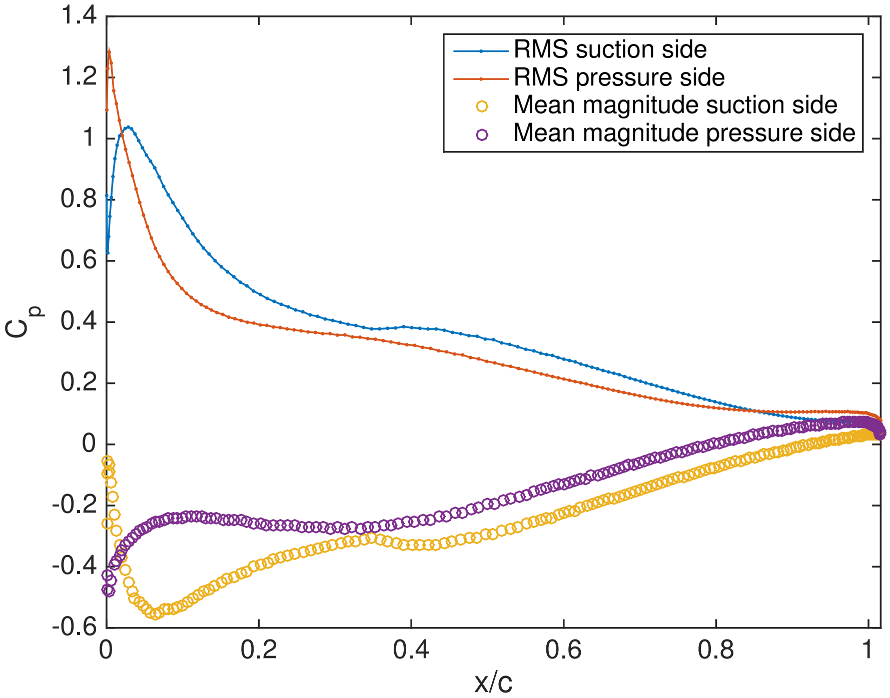

Figure 7.20: Mean and RMS pressure coefficient distribution on airfoil

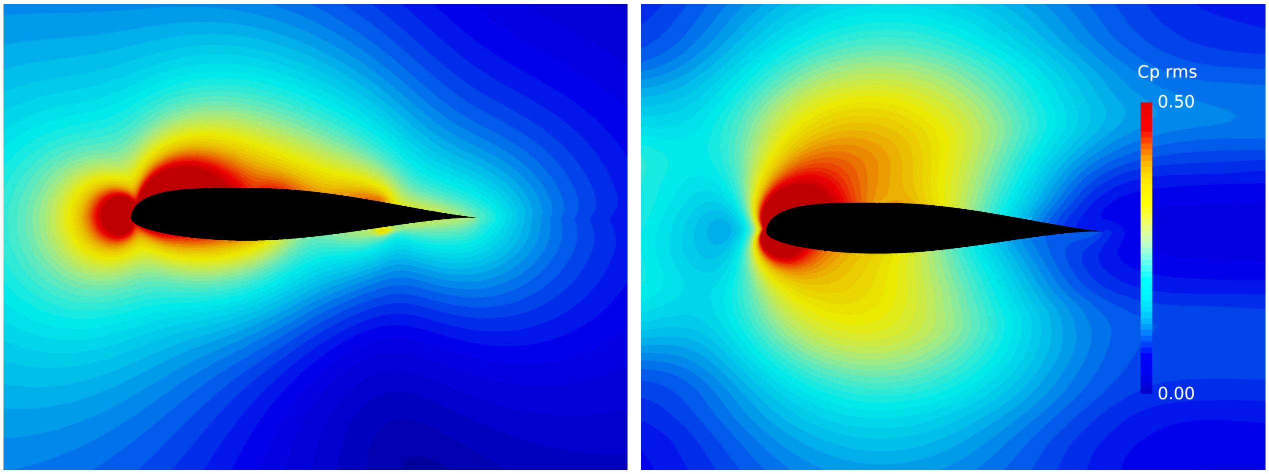

(a) Clean inflow

(b) Cylinder wake

Figure 7.21: RMS Pressure coefficient distribution

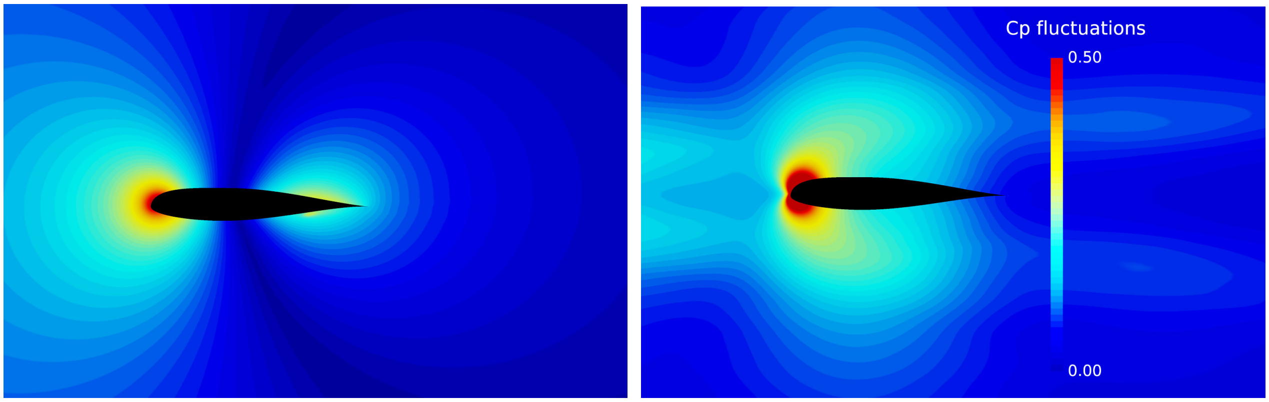

(a) Clean inflow

(b) Cylinder wake

Figure 7.22: Pressure coefficient fluctuations distribution

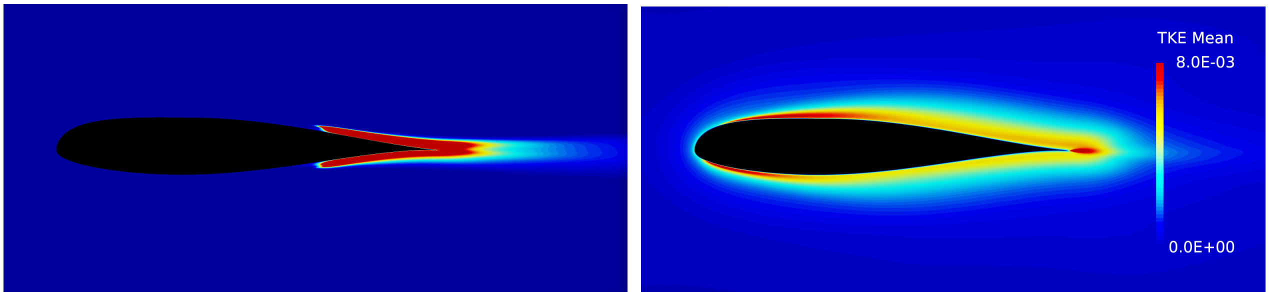

(a) Clean inflow

(b) Cylinder wake

Figure 7.23: Mean TKE distribution

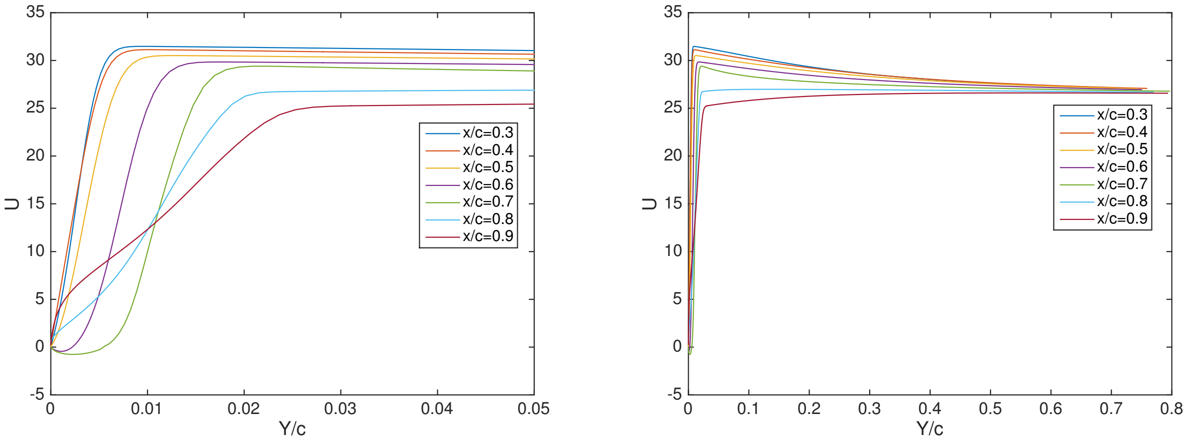

(a) Clean flow (close to surface)

(b) Clean flow (up to Y/c=0.8)

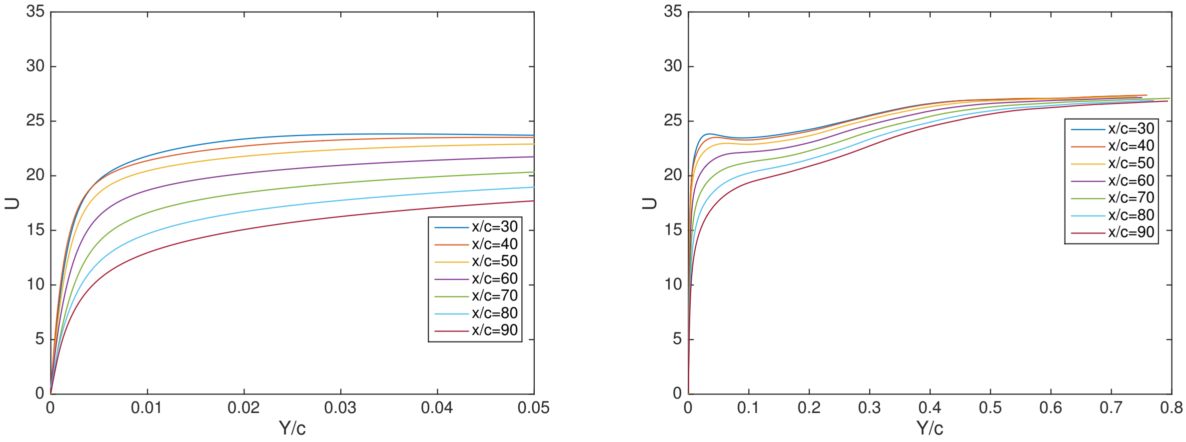

(c) Cylinder wake (close to surface)

(d) Cylinder wake (up to Y/c=0.8)

Figure 7.24: Mean boundary layer profile in chordwise progression

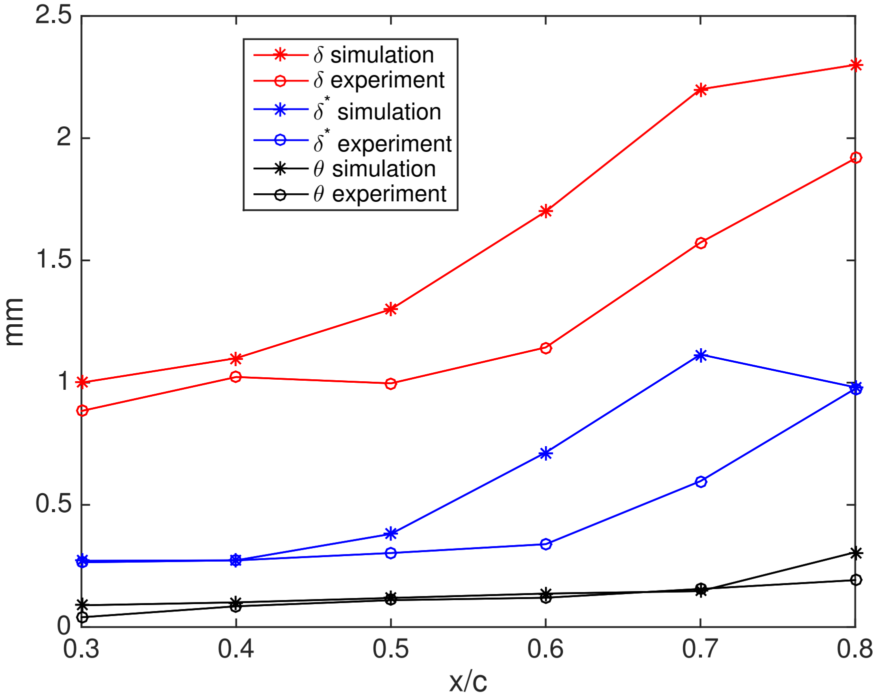

Figure 7.25: Boundary layer thickness of airfoil in clean flow

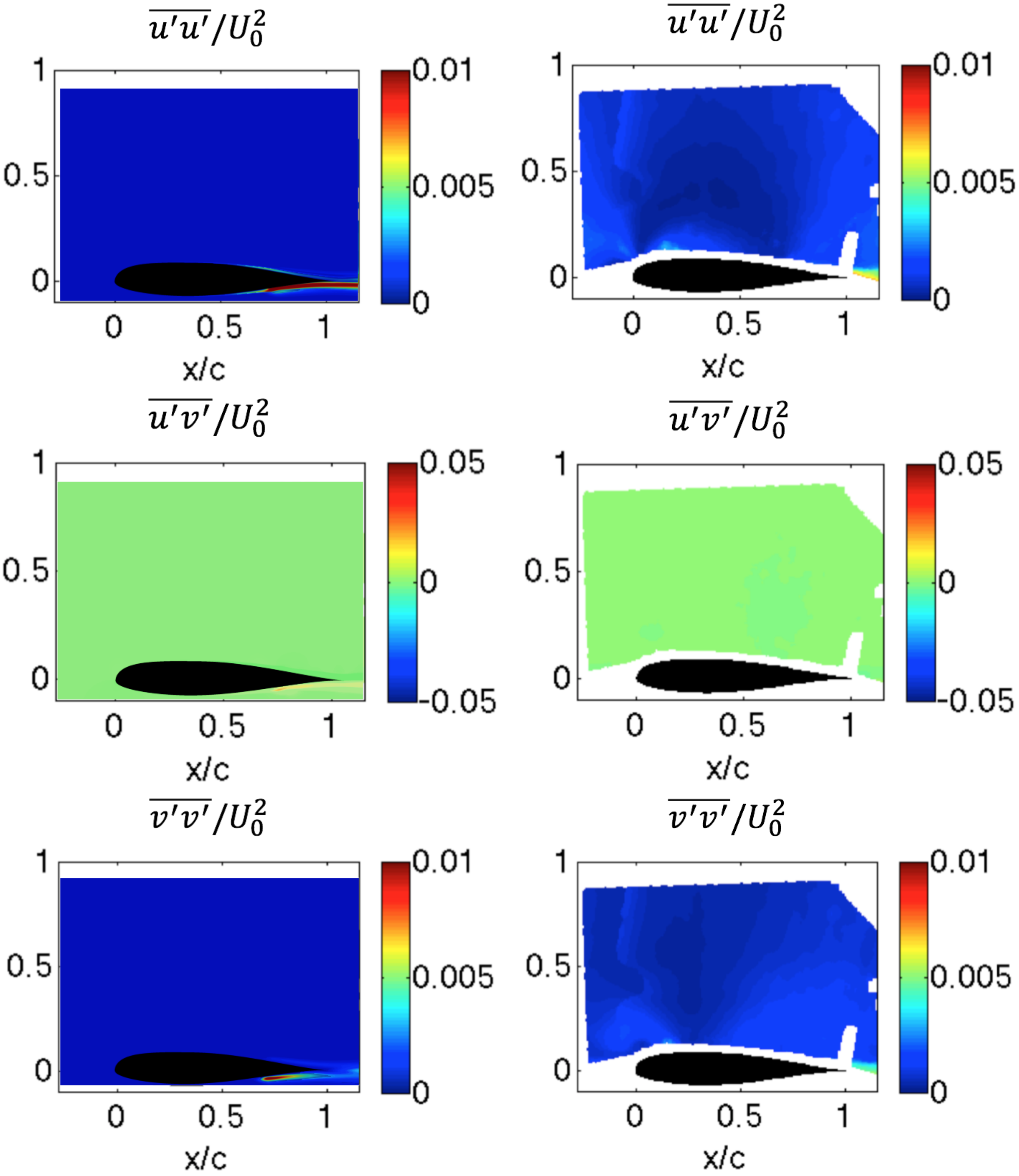

Figure 7.26: Reynolds stress components around airfoil in clean flow

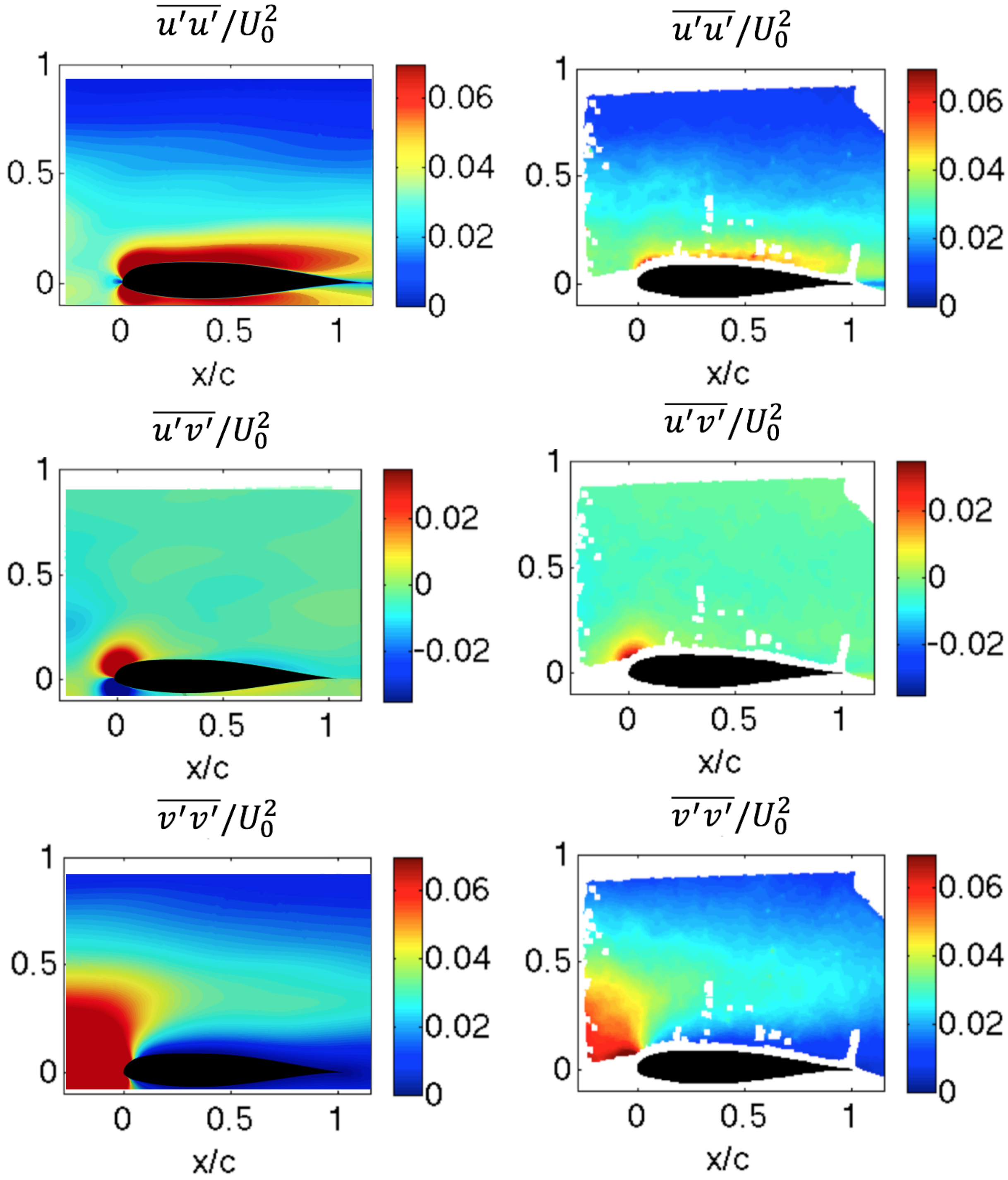

Figure 7.27: Reynolds stress components around airfoil in clean flow

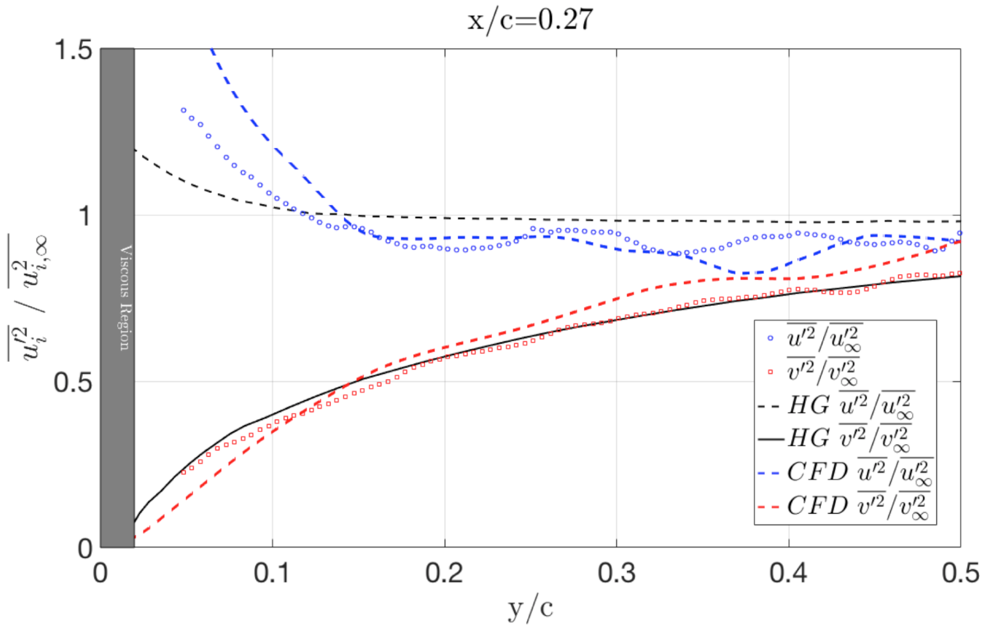

Figure 7.28: Experimental and numerical profiles of the streamwise and transverse Reynolds stress components at $x/c = 0.27$ [76]

Turbulence energy spectrum

Instantaneous flow velocity is sampled at multiple locations upstream and around the airfoil. The velocity components' energy spectra is a benchmark of the local grid refinement level, which is a major criterion for LES-type simulations.

Figure 7.29 is a sketch of the probe locations where the velocity components are sampled. Probes (a-f) are located $0.5c$ above the centerline, probe a is placed half-way between the airfoil and cylinder center, which is $1.9c$ upstream of the leading edge. Figure 7.30 and 7.31 are the corresponding compensated power spectra of the streamwise and transverse velocity u and v respectively for each location. Since all probes sit inside the cylinder wake, the PSD peaks at $f/f_{vs} = 1$ and gradually decreases in magnitude as traveling downstream. The mesh resolution is kept constant across all probe locations and thus all the cutoff frequencies according to the Komolgorov $-5/3$ law are at $\sim 10f_{vs}$.

Another group of probes (A-F) are located at centerline level and inside the airfoil bound-

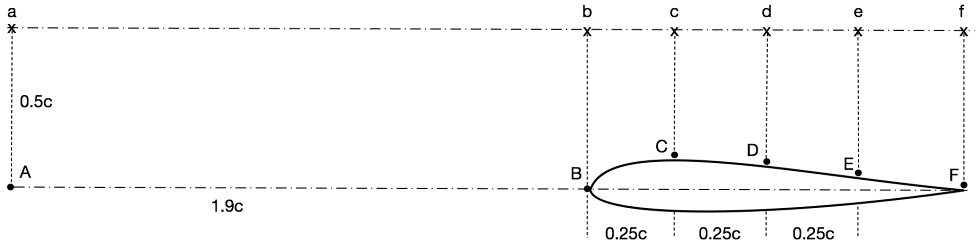

Figure 7.29: PSD probe locations

ary layer (figure 7.32, 7.33). Compare each pair of probes at same streamwise location, the coarser grids outside boundary layer resolves velocity fluctuations to higher frequency even though the grids in the vicinity of the airfoil (probes B-F) are approximately 1/20 of the transverse dimension of the mesh at probes (b-f). This observation confirms that the hybrid model has the ability of resolving more flow structures and the eddy viscosity in RANS region dissipates turbulence energy and more flow fluctuations are modeled.

The PSD of u and v near the leading edge confirms the energy redistribution of the normal Reynolds stress component $\overline{u'u'}$ and $\overline{v'v'}$. Compare plots 7.32b and 7.33b (airfoil leading edge position), the flow fluctuation energy of v is 1.5 orders of magnitude higher than u. While from plots 7.32c and 7.33c (airfoil quarter chord), the energy of u is approximately 1 order of magnitude higher than v.

Phase-averaged boundary layer profiles

Probes are placed from airfoil surface up to $0.1c$ in the wall-normal direction. The phase of a band limited signal $s(\xi)$ is determined by Hilbert transform [77] $h(t)$:

$$h(t) = \frac{1}{\pi}\int_{-\infty}^{+\infty}\frac{s(\xi)}{\xi - t}d\xi \tag{7.1}$$

The phase is calculated as:

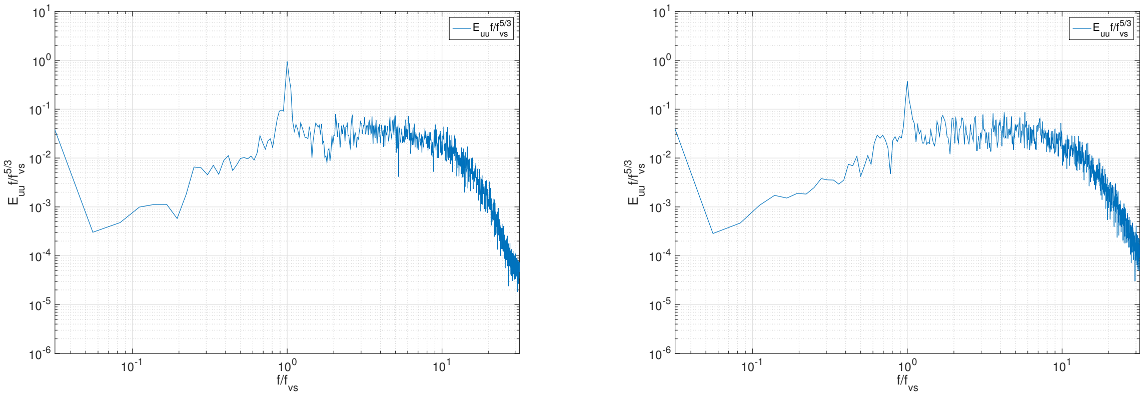

(a) Probe a (b) Probe b

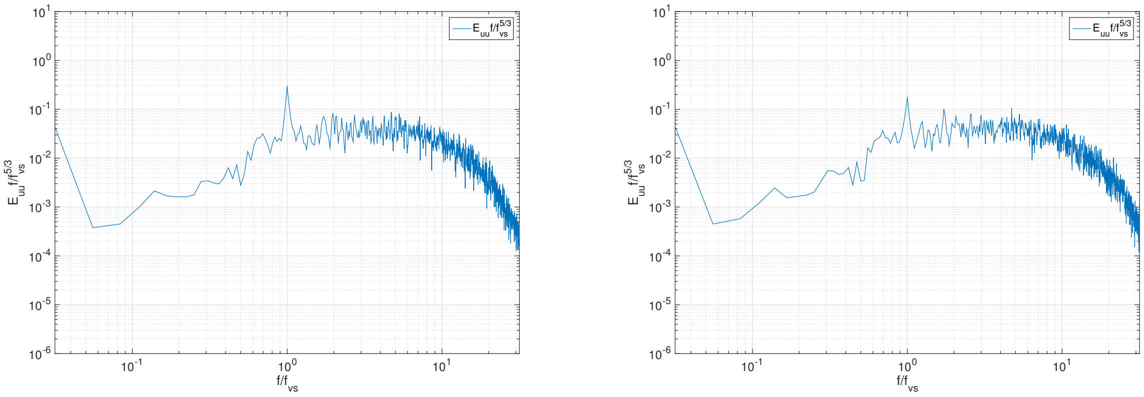

(c) Probe c (d) Probe d

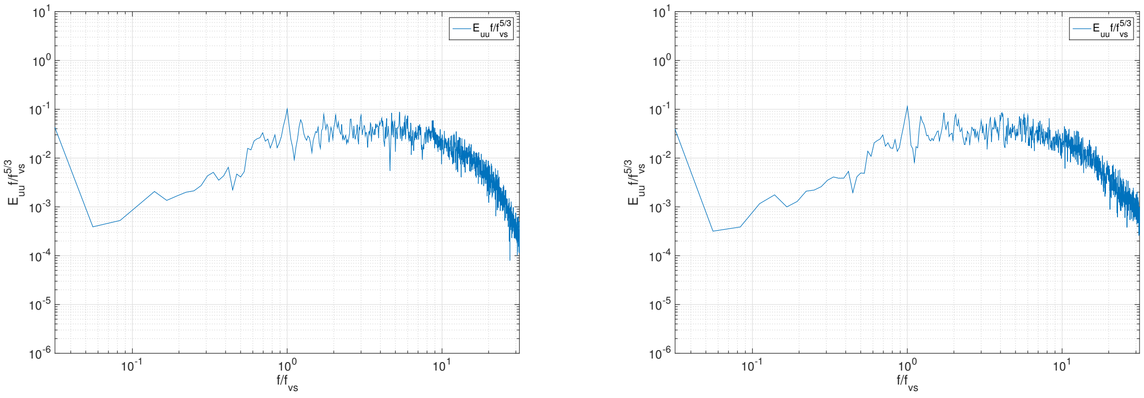

(e) Probe e (f) Probe f

Figure 7.30: Streamwise velocity compensated power spectra of probes (a-f)

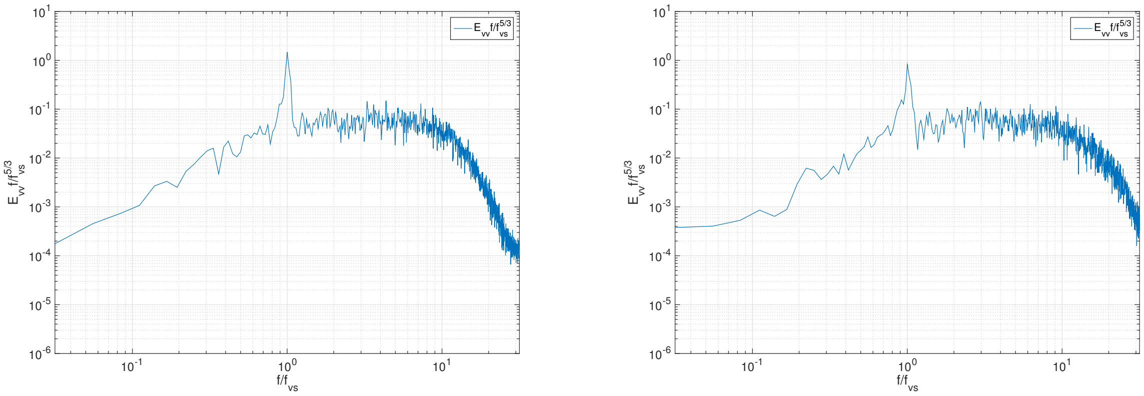

(a) Probe a

(b) Probe b

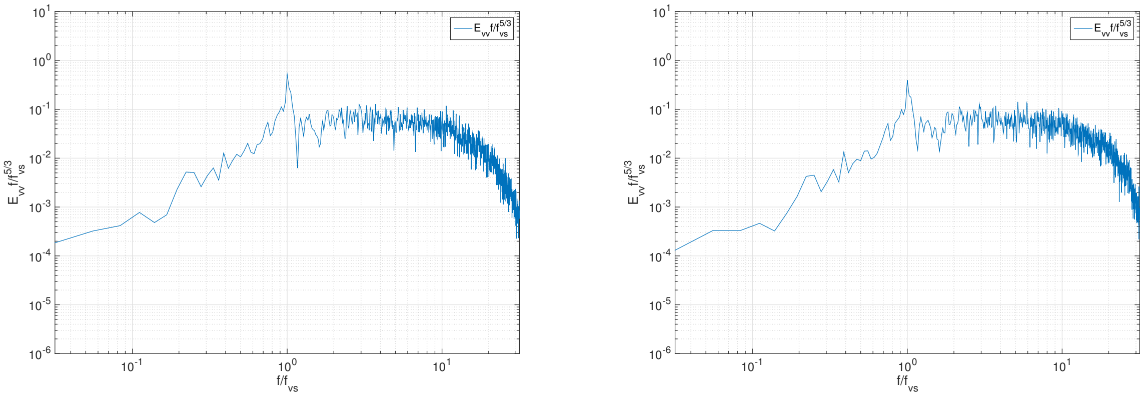

(c) Probe c

(d) Probe d

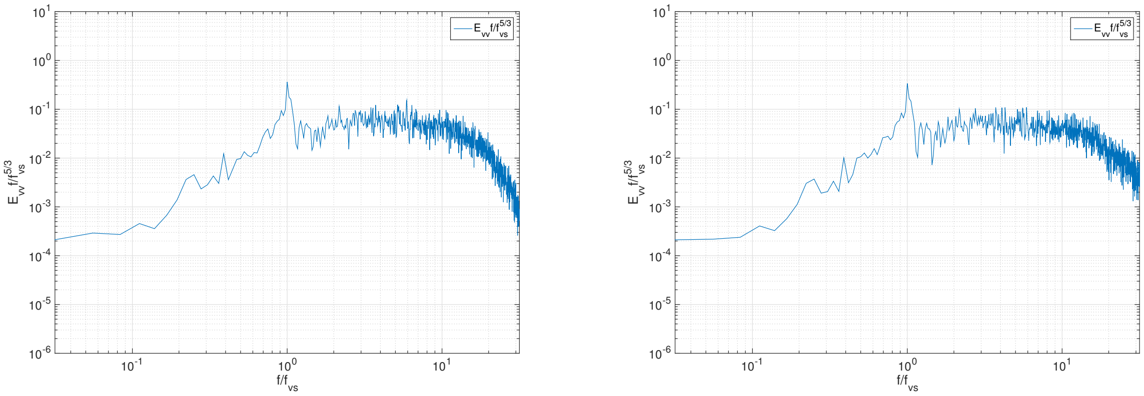

(e) Probe e

(f) Probe f

Figure 7.31: Transverse velocity compensated power spectra of probes (a-f)

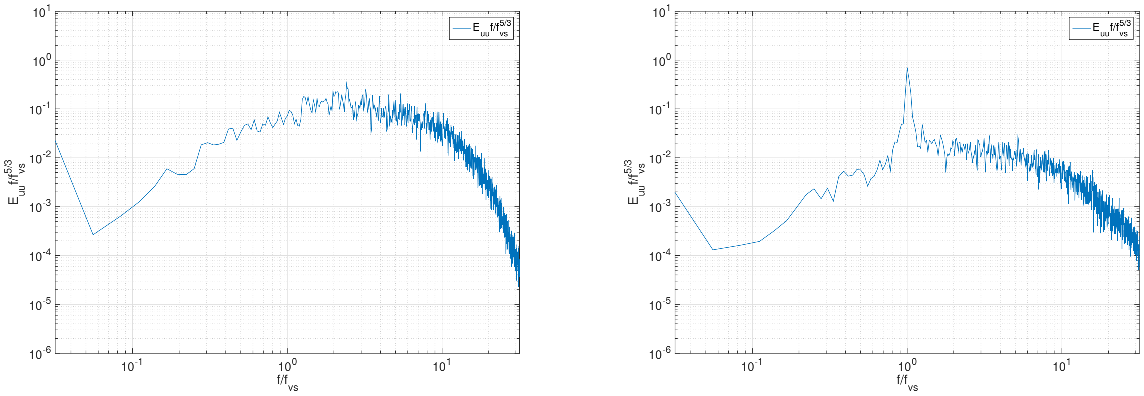

(a) Probe A (b) Probe B

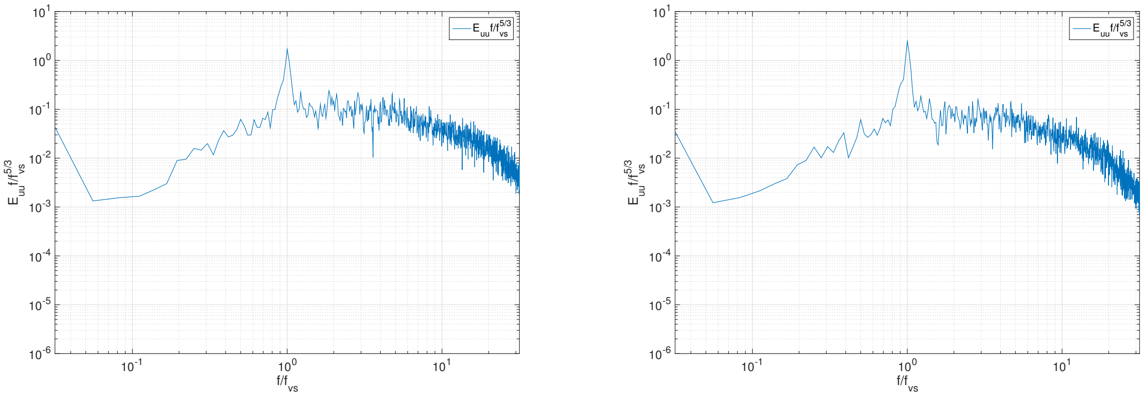

(c) Probe C (d) Probe D

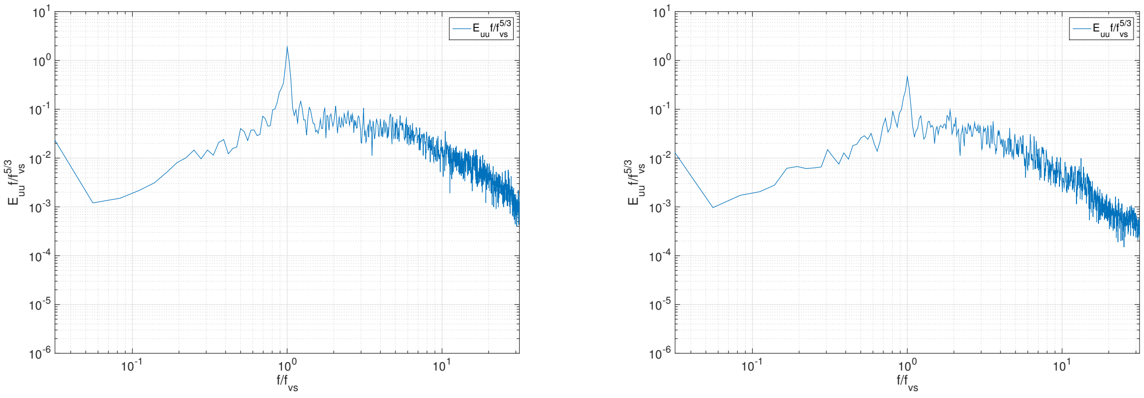

(e) Probe E (f) Probe F

Figure 7.32: Streamwise velocity compensated power spectra of probes (A-F)

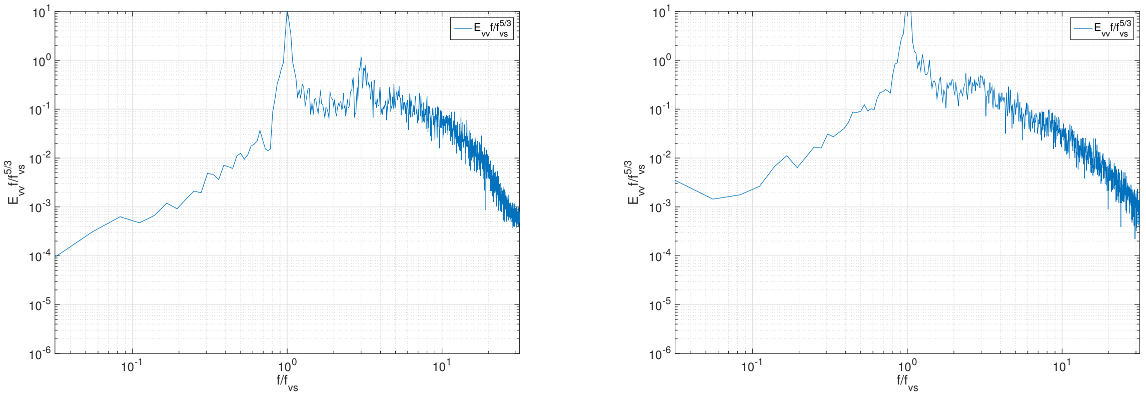

(a) Probe A (b) Probe B

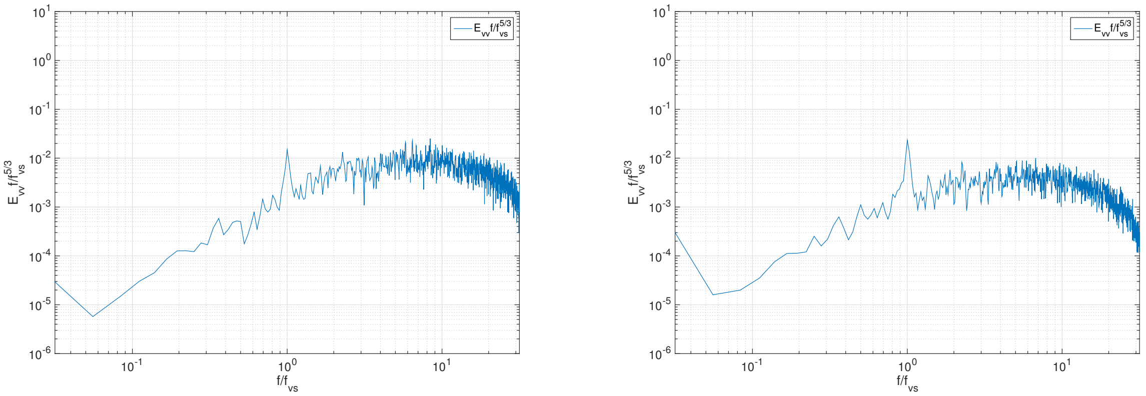

(c) Probe C (d) Probe D

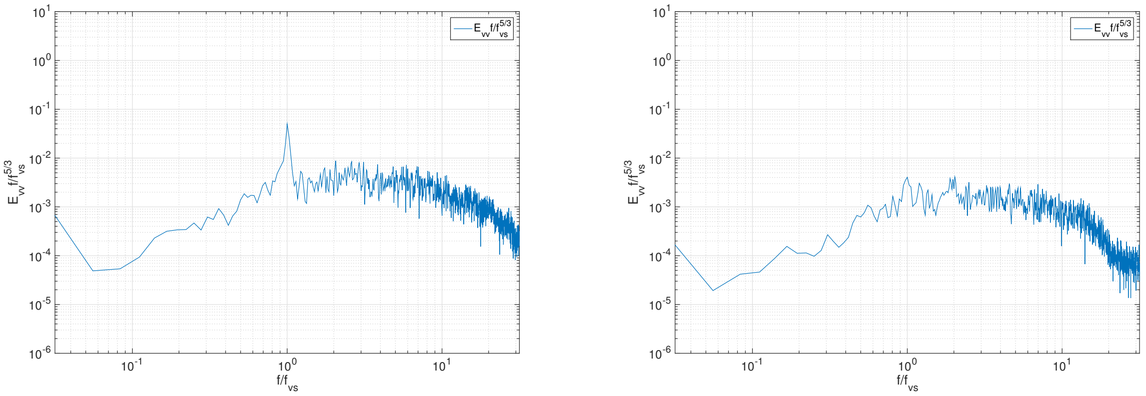

(e) Probe E (f) Probe F

Figure 7.33: Transverse velocity compensated power spectra of probes (A-F)

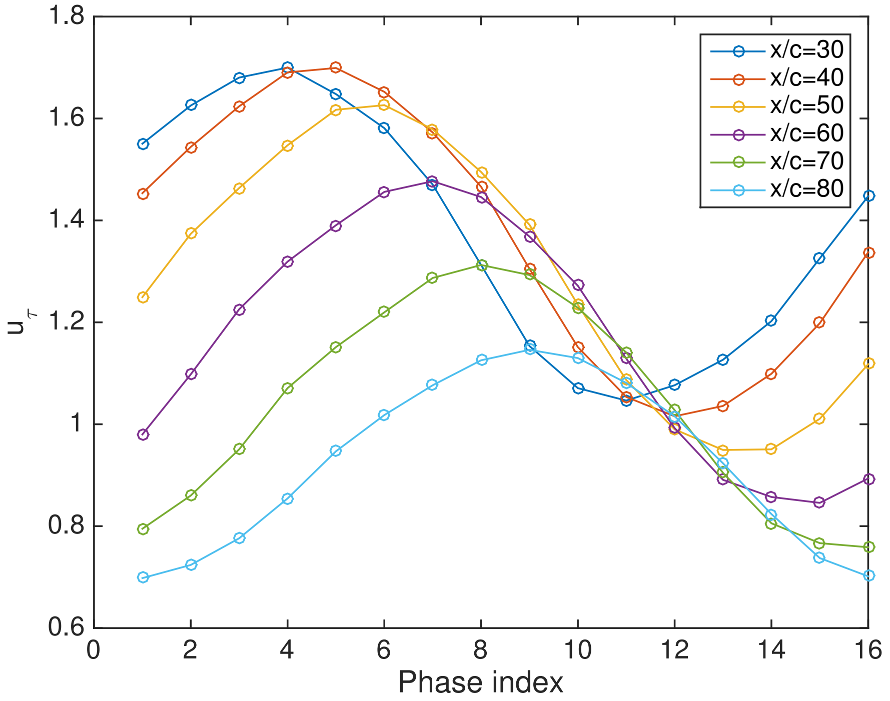

Figure 7.34: Friction velocity for each phase at every chordwise location

$$\phi = \cos^{-1}\left(\frac{real(h(t))}{|h(t)|}\right) \tag{7.2}$$

The simulation data is over 140 periods of the oscillatory flow around the airfoil, each cycle is subdivided into 16 phases with a width of 22.5° phase angles. The velocity profile is then averaged within each phase of all periods. In order to plot the profile in terms of nondimensional parameters u^+ and y^+, a range of the friction velocity u_τ is fitted through least square method to find the best-fit value for the profile in viscous sublayer ($y^+ < 5$) and log layer ($30 < y^+ < 100$). Figure 7.34 is a plot of the friction velocity distribution for each phase at every chordwise positions. We notice a consistent phase-shift and decrease in u_τ as moving downstream, from the amount of phase-shift from station $x/c = 0.3$ to $x/c = 0.8$ together with the flow period, the wave speed is at $22 m/s$.

Phase-averaged boundary layer profiles from simulation and experiments are plotted in figure 7.35 together with the Spalding's single formula for the “Law of the Wall” [99], viz.

$$y^+ = u^+ + 0.1108 \left\{ e^{0.4u^+} - 1 - 0.4u^+ - \frac{(0.4u^+)^2}{2!} - \frac{(0.4u^+)^3}{3!} \right\} \tag{7.3}$$

which is valid through the viscous sublayer and the log layer.

The Log Law curve follows the standard “Law of the Wall” formulation

$$u^+ = \frac{1}{\kappa} \ln y^+ + 5 \tag{7.4}$$

where $\kappa = 0.41$.

The experimental data is available from $y^+ \sim 20$ due to the limited PIV system resolution near surface. Two formulations of “Law of the Wall” converge from approximately $y^+ = 30$ and the mean velocity profile is also plotted on the same figure.

There are several notable observations: although the least square method that fits the curves takes the data between $y^+ < 5$ and $30 < y^+ < 100$ into account, every curve at each chordwise position converges at approximately $y^+ = 50$ and diverges right pass this point, which indicates the cylinder wake dynamics dominate the wake region above $y^+ > 50$. The simulation data shows the magnitude of the oscillation in the wake region gradually grows in chordwise progression, while the experimental data predicted nearly constant variations ($\sim u^{+'} = 5$) of the boundary layer profile at $y^+ \sim 300$. The flow in the boundary layer wake region carries more energy in the simulation results.

Even in the highly-unsteady cylinder wake, the Law of the Wall is still valid in the low-momentum viscous inner regions, which confirms the validity of its adoption is many wall-modeled RANS and LES applications. Finally, the Law of the Wall agrees better with the phase and mean profiles of downstream locations, where the boundary layers are significantly thicker.

7.3 Conclusion and Summary

The full-model added an airfoil $10.7D$ downstream of circular cylinder, mesh around airfoil was again refined to resolve the boundary layer of airfoil with $Re_c = 1.7 \times 10^5$. Same boundary conditions and numerical schemes were applied as in cylinder-only case. For reference purpose, another case with the identical setups except removing the upstream cylinder was also tested.

The LM turbulence intermittency field γ accurately predicted the transition after laminar separation in the foil-only case. The boundary layer thickness δ, displacement thickness δ^* and momentum thickness θ on airfoil suction side also showed good agreement with our experimental data.

By inspecting the lift and drag fluctuations of the airfoil in cylinder wake, we found the dominant unsteadiness is at cylinder shedding frequency f_{vs}, thus as in the cylinder-only case, we examined the instantaneous flow field within one period. The shielding function F_{DDES} showed that the hybrid model switched back to RANS mode inside the airfoil boundary layer, which is essential for evaluating the model performance since the boundary layer mesh is far coarser from supporting LES-type simulation. Despite the large fluctuations in local flow angles at airfoil position as shown in last chapter, the boundary flow remained attached at all time, which was also confirmed by experiments. We noticed a redistribution of turbulence energy between Reynolds stress components $u'u'$ and $v'v'$ at the leading edge of the airfoil, this phenomena was precisely capture by the experiments and explained by Rapid Distortion Theory(RDT).

Due to the periodic nature of the cylinder wake, phase-averaging technique was applied to the airfoil boundary layer. There was a phase-lag in chordwise progression and the wave-like behavior in local skin friction moves at $22m/s$ along the suction side. Despite the variations in the outer boundary layer profile the phase-averaged boundary layer profiles collapsed into Spalding's improved Law of Wall in the range of $0 < y^+ < 50$, which demonstrated that the wall function is still valid in the unsteady boundary layer.

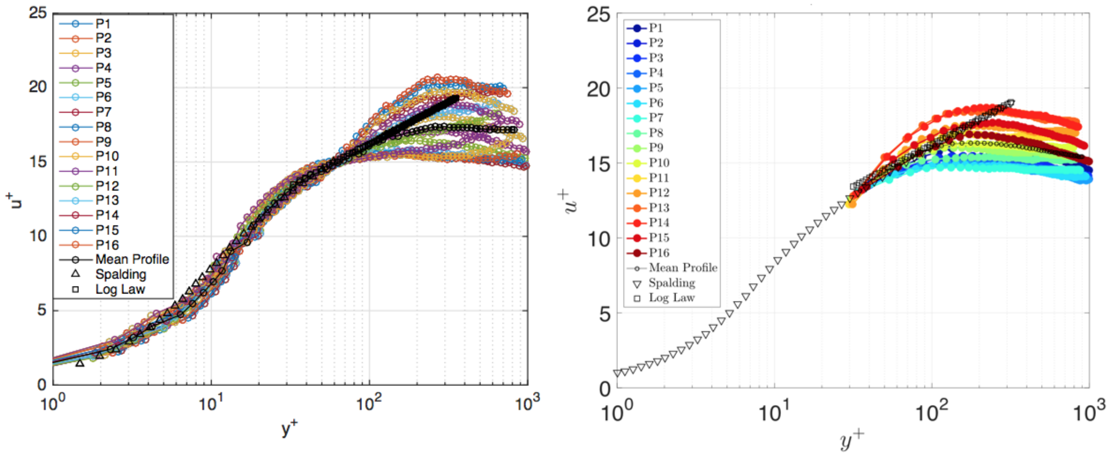

(a) $x/c = 0.3$

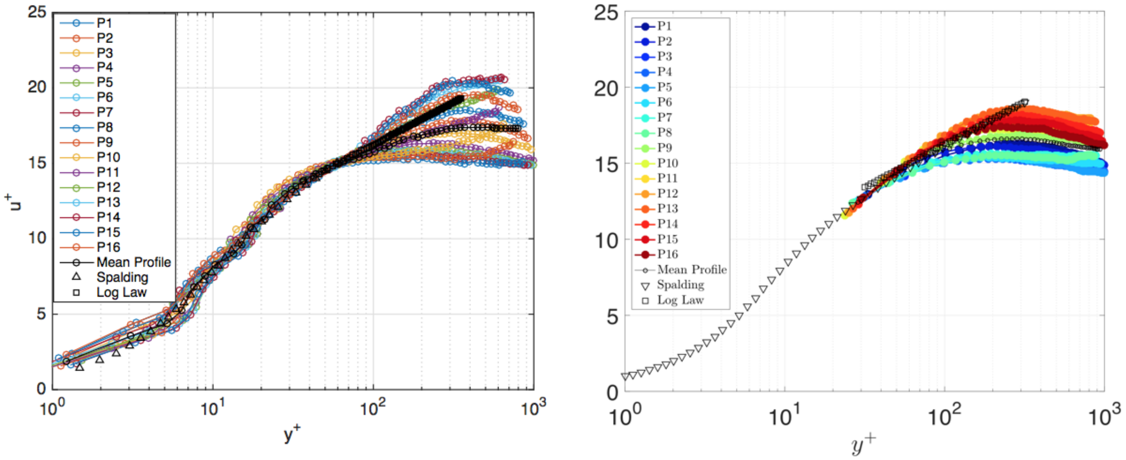

(b) $x/c = 0.4$

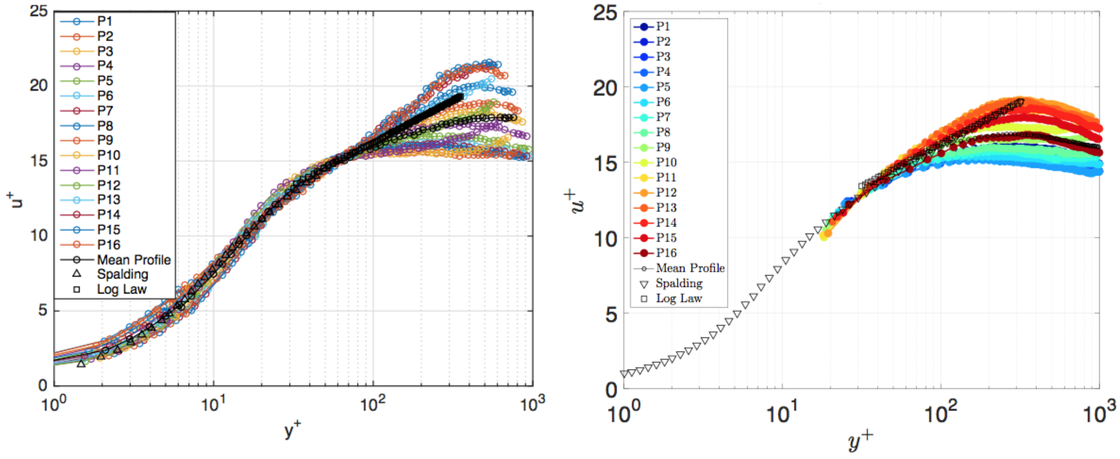

(c) $x/c = 0.5$

Figure 7.35: Phase-averaged boundary layer profiles. Left: simulation, right: experiment

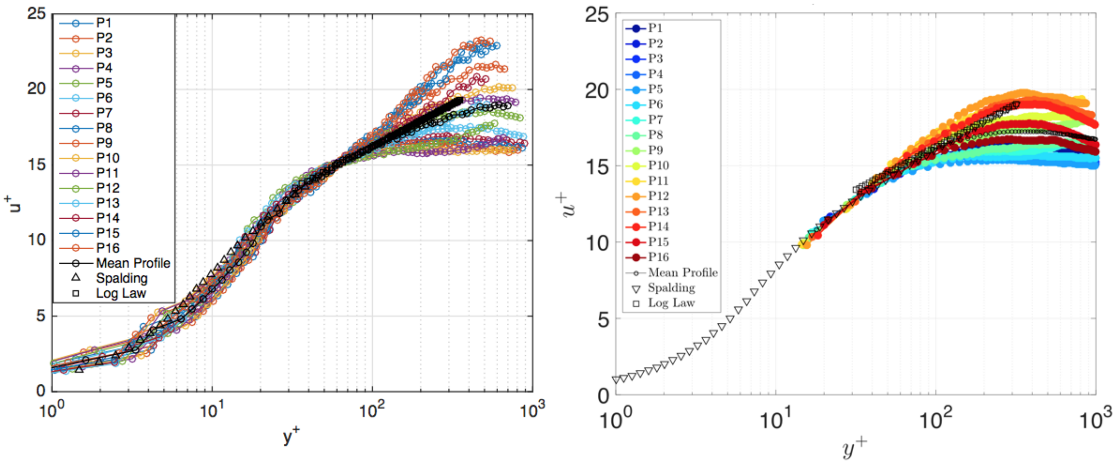

(d) $x/c = 0.6$

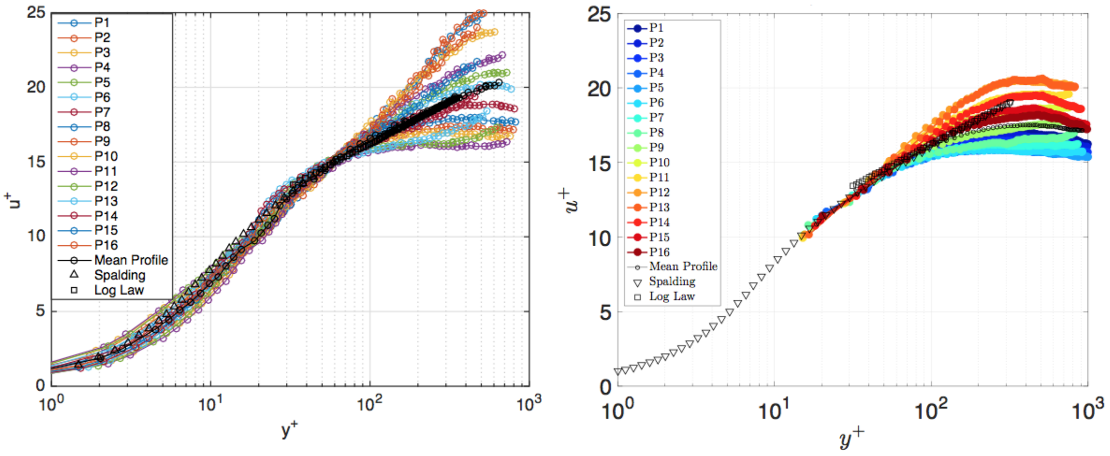

(e) $x/c = 0.7$

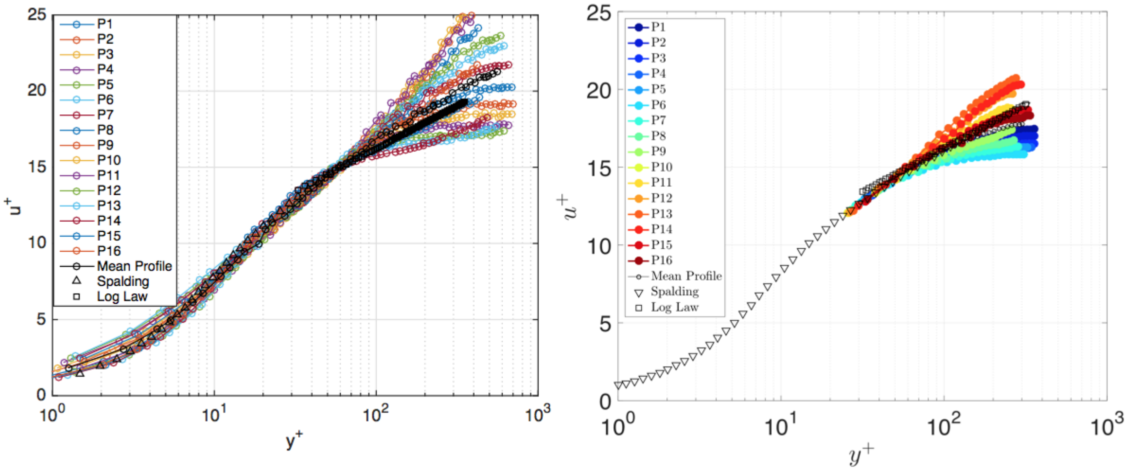

(f) $x/c = 0.8$

Figure 7.35 (cont.): Phase-averaged boundary layer profiles. Left: simulation, right: experiment

Chapter 8

Conclusions and Outlook

The main objective of the this study is to find an improved turbulence modeling approach that can capture the flow physics presented in the boundary layer of wind turbine blade inside Atmospheric Boundary Layer(ABL) and upstream turbine wake. A surrogate model was designed to keep the computational cost manageable while preserving the key flow physics as in the full-scale problem. We realized the pure LES-type turbulence model is beyond the computing power available currently even just for the surrogate model and the previous studies show that the integration of transition formulation in RANS model improved blade physics predictions.

The Delayed Detached Eddy Simulation (DDES) was chosen as the hybrid modeling methodology for its superior performance than RANS in largely-separated flow regions at affordable computational cost. The implementation of the transition model was verified against the simulation data by its original authors and validated using well-established experimental data (Chapter 5). The integrated transition hybrid turbulence model was then applied to circular cylinder at subcritical Reynolds number and yielded good agreements with experimental data (Chapter 6). Applying the transition hybrid model to the full-model led to some major discoveries in unsteady flow physics (Chapter 7).

8.1 Transition Hybrid Model Performance

The transition hybrid model in our study is based on two-equation $k-\omega$SST model that takes account the shear stress transport and blends the advantages of original $k-\omega$ model and $k-\epsilon$ model. Both the hybrid and transition formulation is realized through manipulating the modeled turbulence kinetic energy(TKE). The explicit equation for TKE in $k-\omega$SST model makes this process straightforward: enhanced TKE dissipation in LES region and reduced TKE production in laminar and transition regions. Besides, the existing blending functions in $k-\omega$SST model makes it an ideal choice for preserving the boundary layer in RANS mode, which is the desired feature of DDES over original DES. The open-source framework provided by OpenFOAM facilitated the implementation of the new model, which was compiled into a run-time library.

8.1.1 Transition Model Assessment

The transition model performance was verified and validated through the numerical results from the model's original author's implementation and well-established experimental data. The flat-plate case is a classic example for testing boundary layer transition, the geometry used in our study has a circular leading edge, which introduces laminar separation and reattachment. The V&V process was completed by testing the 2D S809 wind turbine blade, the separation and transition locations were predicted within 5% error compared with benchmark CFD and experimental data.

8.1.2 Circular Cylinder Flow

The transition model was integrated with hybrid formulation and further tested in circular cylinder flow. As a precursor of full-model test and turbulence generator for the unsteady boundary layer downstream, it is vital to make sure that the vortex shedding is at correct frequency and strength. Unlike supercritical cylinder flow, the boundary layer undergoes laminar separation and transition, using a fully-turbulent model will lead to delayed separation and higher shedding frequency as seen in higher Reynolds number cases. The transition model precisely captured the laminar separation points and the shedding frequency. Furthermore, the shielding function in hybrid formulation protected the boundary layer from premature switch to LES mode, which makes the calculation grid-dependent and usually leads to a problem called Modeled-Stress-Depletion(MSD). Mesh in the wake of the cylinder was coarsened to a level that a considerable amount of turbulence energy was resolved while the computational load was still manageable. The PSD of transverse velocity component in the cylinder wake showed gradual decrease in resolved energy level, which is inversely proportional to the local grid size. The grid size outside the immediate wake was kept constant towards the airfoil and same level of resolved turbulence energy was maintained downstream.

8.2 Unsteady Flow Physics Around Airfoil

The successful prediction of circular cylinder flow gave us confidence in extending the application of transition hybrid model to the unsteady flow physics on the downstream airfoil. A separate case with foil-only set up was tested for reference purpose, the corresponding experimental data was also available from our wind tunnel test. As in the 2D S809 airfoil case, the NACA63215b airfoil in our surrogate model experienced same flow physics in clean flow despite one order of magnitude lower in Reynolds number. Good agreements was obtained in separation and transition locations as well as in boundary layer statistics.

As for the hybrid model performance, the hybrid model switched from RANS in cylinder boundary layer to LES in its wake and then back to RANS inside the airfoil boundary layer. The velocity components' PSD confirmed that less turbulence energy was resolved inside the boundary layer despite using finer grids. Inspecting the LM turbulence intermittency field, there existed a thin layer of $\gamma << 1$ around airfoil surface where the laminar sublayer lies.

Further out of the airfoil surface, the LM intermittency field γ rose towards 1. Note that γ is merely a weighting factor of TKE production, which was used to turn on/off of the turbulence model, the value of γ is different from physical definition of turbulence intermittency and even at its limits, i.e. $\gamma = 0$(laminar) and $\gamma = 1$(fully turbulent), there is still lag in the production of TKE for the flow to be fully laminar or turbulent.

Surprisingly, the large and rapid fluctuations in local flow angles in cylinder wake did not lead to airfoil dynamic stall or even flow separation, the turbulent boundary layer remained attached along the entire suction side at all time. Experimental data confirmed our observation and found that the periodic boundary layer exhibited Stokes layer behavior [76]. We also noticed a redistribution of turbulence energy between Reynolds stress components $u'u'$ and $v'v'$ at the leading edge of the airfoil, this phenomena was precisely capture by the experiments and explained by Rapid Distortion Theory(RDT).

Since the dominant unsteadiness is induced by vortices in cylinder wake, the periodicity makes the phase-averaging an ideal analyzing approach. Every period was subdivided into 16 bins and velocity profiles inside each bin were averaged. The lease-square method was adopted to find the wall friction velocity u_τ and we found that the phase-averaged boundary layer profiles collapsed into Spalding's improved Law of Wall in the range of $0 < y^+ < 50$ at multiple locations along the suction side. It suggested that the wall function is not only valid for the instantaneous boundary layer velocity profile near the wall but also for the phase-averaged and mean profiles.

8.3 Future Work and Outlook

The major downside of our current surrogate model is the scale mismatch compared with full-scale problem as summarized in table 4.1. The inflow unsteadiness is the key parameter in determining the blade dynamics, other than the blade root, the reduced frequency of the full-scale blade is approximately one or two orders of magnitude lower that our model. By manipulating the definition of Strouhal number $St = fD/v$ and reduced frequency $k = \omega b/v$ we have $k = \pi St \frac{c}{D}$, St maintains ~ 0.2 for $10^3 < Re_D < 10^6$ the reduced frequency $k \sim 0.63c/D$ is determined by the ratio of the chord length and cylinder diameter, a scale-up model design will focus on increasing the cylinder size. Another benefits of larger cylinder is increasing the turbulence length scale that can engulf the whole airfoil as the atmospheric turbulence does to the full-scale turbine blade. The new flow fields resembles the harmonic gust problem described by Sears function.

The computation resource required will also increase with model scale. The simulation time-step is determined by the size of boundary layer mesh near surface and flow velocity, the new simulation required approximately twice the simulation wall-time assuming linear scaling in parallel computation.

In conclusion, the transition hybrid RANS/LES model showed its potential in calculating unsteady flow physics of a model wind turbine blade. Compared with RANS model, it resolves the turbulence structure down to the local grid size, which is averaged and smeared in unsteady RANS simulations; compared with LES model, the computational cost is affordable for most practical problems and the meshing process is less stringent since the new model can at worst operate in RANS mode. Besides, the integration of transition model enabled the accurate prediction of laminar separation, transition and flow reattachment, which were proven to be first order factors in calculating blade aerodynamics.

Appendix A

OpenFOAM Basics

First developed in 1980s at Imperial College London, OpenFOAM stands for Open Field Operations And Manipulation, it implements a collection of numerical PDE solvers and utilities for continuum mechanics. OpenFOAM was releases under the GNU General Public License as open source software, which allows users to freely use and freely modify the source code. Compared with proprietary CFD code, it provides a framework for developers implementing their in-house solver/algorithms without starting from scratch. The user community grows exponentially since it's release in 2004 owing to its flexibilities, however, it's also criticized for its lack of graphic user interface and documentations.

A.1 Development and applications

OpenFOAM is developed by C++ for its programming flexibility over the more standard engineering programming language FORTRAN. It allows the program to fully utilize the features of object-oriented language, and directly increases its expandability for developers. Dozens of forks are branched from main-branch OpenFOAM as free and proprietary software. A few notable forks includes the OpenFOAM-Extended, which has a large repository of user community generated contributions; Caelus, which extends the OpenFOAM platform over Microsoft Windows; Visual-CFD, which is a graphic user interface developed by OpenCFD.

As a comprehensive compilation of continuum mechanics solvers, OpenFOAM is dedicated to compressible/incompressible combustion, heat transfer or multiphase problems. As a highly-parallelized PDE solve, It also implements solid mechanics, electromagnetic and even financial models.

A.2 Flow solvers and turbulence modeling

OpenFOAM implements a wide variety of flow solvers for different physics. The high-level abstraction and encapsulation of OpenFOAM's mathematical models makes the implementation of new equations straightforward, users are free to modify current solvers or develop new ones with minimum amount of efforts. A example of momentum equation in incompressible PISO solvers is shown below:

```
fvVectorMatrix UEqn
(
    fvm::ddt(U)
    + fvm::div(phi, U)
    + turbulence->divDevReff(U)
);
```

The discrete operators are implemented as function templates in C++, which makes them reusable and highly readable. The discrete schemes for each terms are defined in case file and read at runtime. No default setting for the numerical schemes and residual control in OpenFOAM, users need to specify them for each case.

The hierarchy of turbulence model library was reconstructed in version 3.0, the current study is based on version 2.4.x, which is a stable bug-fixed version. Dozens of LES, RANS and hybrid models are provided for incompressible/compressible flow. Each turbulence model implements the *nuEff()* and *correct()* method, which returns effective eddy viscosity and provides turbulence correction at each time step. All hybrid models are categorized as LES models with the underlying RANS as subgrid scale(SGS) model.

User-defined solvers and turbulence models follow the same construction as native code, users are recommended to create custom libraries for the new code and add into library list at runtime.

A.3 Parallel computing

OpenFOAM uses *OpenMPI* implementation of the message passing interface(MPI) as default. MPI is a standard application programming interface for parallel programming in C, C++ and FORTRAN on distributed-memory machines. Compared with shared-memory mechanism, MPI is more versatile and allows parallel computing over larger scale.

Domain decomposition is the first step of parallel simulation in OpenFOAM, different decomposing schemes are available. In order to maintain proper performance scaling with amount of assigned computing resource, as a rule of thumb, the number of cells per processor should not be below 50,000. Otherwise, the communication overhead between each processor significantly reduces computational efficiency.

OpenFOAM generates one file for each field in every domain at each writing point. For large simulations, the total number of generated files can easily exceed maximum allowance of the file system. Data analysis and visualization also requires parallel routines to reduce processing time, further details will be given in following sections.

A.4 Utilities

As a comprehensive CFD software, OpenFOAM provides multiple pre-/post-processing utilities to aid case setup and data processing. Some mostly used utilities are listed here:

- **checkMesh**: report mesh statistics and check validity of mesh, including domain topology and grid geometry.
- **decomposePar**: automatically decompose flow field according to decomposition settings.
- **reconstructPar**: reconstruct fields of a case that is decomposed for parallel computing.
- **createPatch**: create patches from existing patch or faceSet.
- **vorticity**: compute vorticity field according to velocity field.
- **Lambda2**: create Lambda2 field for visualization of vortex structures.
- **R**: calculate Reynolds stress field by Boussinesq approximation.

Some community-developed utilities further expands the usability of OpenFOAM, *swak4Foam* [100] is a popular third-party library among users, the most notable utilities includes the *groovyBC* and *funkySetFields*, which enable users to specify arbitrary boundary conditions and value of scale or vector field according to user-defined expressions.

Appendix B

SIMPLE/PISO Algorithms

Semi-Implicit Method for Pressure Linked Equation(SIMPLE) [79] and Pressure Implicit with Splitting of Operator(PISO) [78] algorithm are two of the most widely used algorithms for solving incompressible Navier-Stokes equations.

B.1 Algorithm formulations

SIMPLE algorithm in OpenFOAM is used to solve steady problems, it is also used to solve unsteady problem in other software. Its iterative process constructs the correction to the present iteration based on the residuals from last iteration, the standard procedure for incompressible flow is as follows [101]:

1. Start iteration by guessing pressure field, denote as p^*.

2. Calculate velocity field u^*, v^* and w^* by momentum equation using p^*, this is called the **momentum predictor**.

3. Construct a pressure correction term p' so that the velocity field satisfy the continuity

equation, the flow field solutions become:

$$p = p^* + p' \tag{B.1}$$

Apply corresponding velocity field corrections, this is called the **velocity correction**

$$\begin{aligned} u &= u^* + u' \\ v &= v^* + v' \\ w &= w^* + w' \end{aligned} \tag{B.2}$$

4. Repeat process from step 2, until a velocity field that satisfy the continuity equation is found.

In order to maintain numerical stability, under-relaxation factors for both pressure and velocity field are usually used.

$$\begin{aligned} p^{n+1} &= p^n + \alpha_p(p - p^n) \\ \mathbf{u}^{n+1} &= \mathbf{u}^n + \alpha_{\mathbf{u}}(\mathbf{u} - \mathbf{u}^n) \end{aligned} \tag{B.3}$$

Where α_p and $\alpha_{\mathbf{u}}$ are under-relaxation factors that varies from 0 to 1. p^n and $\mathbf{u}^n$ are the pressure and velocity field from last time step, p and $\mathbf{u}$ are new pressure and velocity field calculated in step 3 and p^{n+1} and $\mathbf{u}^{n+1}$ are used in step 2 for the next time step.

The PISO algorithm is constructed based on SIMPLE and following the same principle of momentum predictor and velocity correction. Instead of using one predictor-correction in a time step, PISO algorithm consists of one momentum predictor follows by a series of pressure solutions and velocity corrections.

Bibliography

[1] Windtec Solutions AMSC. Seatitan 10mw wind turbine, 2012.

[2] David Weston. Siemens teases a 10mw+ turbine, June 2016.

[3] Ganesh Vijayakumar. *Non-Steady Dynamics of Atmospheric Turbulence Interaction with Wind Turbine Loadings through Blade-Boundary-Layer-Resolved CFD*. PhD thesis, Penn state, 2015.

[4] Pankaj K Jha, Matthew J Churchfield, Patrick J Moriarty, and Sven Schmitz. Accuracy of state-of-the-art actuator-line modeling for wind turbine wakes. *AIAA Paper*, (2013-0608), 2013.

[5] Niels N Sørensen, JA Michelsen, and S Schreck. Navier–stokes predictions of the nrel phase vi rotor in the nasa ames 80 ft× 120 ft wind tunnel. *Wind Energy*, 5(2-3):151–169, 2002.

[6] CE Lynch and MJ Smith. Unstructured overset incompressible computational fluid dynamics for unsteady wind turbine simulations. *Wind Energy*, 16(7):1033–1048, 2013.

[7] A Le Pape and J Lecanu. 3d navier–stokes computations of a stall-regulated wind turbine. *Wind Energy*, 7(4):309–324, 2004.

[8] Jeppe Johansen, NN Sorensen, JA Michelsen, and S Schreck. Detached-eddy simulation of flow around the nrel phase-vi blade. In *ASME 2002 Wind Energy Symposium*, pages 106–114. American Society of Mechanical Engineers, 2002.

[9] Florian R Menter, RB Langtry, SR Likki, YB Suzen, PG Huang, and S Völker. A correlation-based transition model using local variables—part i: model formulation. *Journal of turbomachinery*, 128(3):413–422, 2006.

[10] Niels N Sørensen. Cfd modelling of laminar-turbulent transition for airfoils and rotors using the γ- model. *Wind Energy*, 12(8):715–733, 2009.

[11] R Lanzafame, S Mauro, and M Messina. Wind turbine cfd modeling using a correlation-based transitional model. *Renewable Energy*, 52:31–39, 2013.

[12] John A Ekaterinaris and Max F Platzer. Computational prediction of airfoil dynamic stall. *Progress in aerospace sciences*, 33(11):759–846, 1998.

[13] Tarak Nath Nandi. *Effects of Blade Boundary Layer Transition and Daytime Atmospheric Turbulence on Wind Turbine Performance Analyzed with Blade-Resolved Simulation and Field Data*. PhD thesis, The Pennsylvania State University, 2017.

[14] Di Zhang, Daniel Cadel, Eric Paterson, and K Todd Lowe. Numerical and experimental study of the unsteady transitional boundary layer on a wind turbine airfoil. In *35th Wind Energy Symposium*, page 0917, 2017.

[15] GWEC. Global installed power capacity (mw)-regional distribution.

[16] Thomas Ackermann et al. *Wind power in power systems*, volume 140. Wiley Online Library, 2012.

[17] US Department of Energy. 20% wind by 2030. *DOE/GO-102008-2567, US Department of Energy*, 2008.

[18] NERRC IVGTF. Task2.1 report: Variable generation power forecasting for operations.

[19] Robert W Thresher and Darrell M Dodge. Trends in the evolution of wind turbine generator configurations and systems. *Wind Energy*, 1(S1):70–86, 1998.

[20] Herman Snel. Review of aerodynamics for wind turbines. *Wind energy*, 6(3):203–211, 2003.

[21] James F Manwell, Jon G McGowan, and Anthony L Rogers. *Wind energy explained: theory, design and application*. John Wiley & Sons, 2010.

[22] E Ferrer and X Munduate. Wind turbine blade tip comparison using cfd. In *Journal of Physics: Conference Series*, volume 75, page 012005. IOP Publishing, 2007.

[23] H Link. Gearbox reliability collaborative-phase 1 and 2 overview (presentation). Technical report, National Renewable Energy Laboratory (NREL), Golden, CO., 2011.

[24] International Electrotechnical Commission et al. Wind turbines-part 1: design requirements. *IEC61400-1*, 2005.

[25] D Zhang and EG Paterson. A study of wave forces on an offshore platform by direct cfd and morison equation. In *E3S Web of Conferences*, volume 5. EDP Sciences, 2015.

[26] James Brasseur, Eric Paterson, Sven Schmitz, Robert Campbell, Ganesh Vijayakumar, Adam Lavely, Balaji Jayaraman, Tarak Nandi, Pankaj Jha, Alex Dunbar, et al. A"cyber wind facility"for hpc wind turbine field experiments. In *APS March Meeting Abstracts*, volume 1, page 1189, 2013.

[27] Horns rev wind farm, courtesy of national oceanic and atmospheric administration (noaa)., 2016.

[28] D Mehta, AH Van Zuijlen, B Koren, JG Holierhoek, and H Bijl. Large eddy simulation of wind farm aerodynamics: A review. *Journal of Wind Engineering and Industrial Aerodynamics*, 133:1–17, 2014.

[29] Karl Nilsson, Stefan Ivanell, Kurt S Hansen, Robert Mikkelsen, Jens N Sørensen, Simon-Philippe Breton, and Dan Henningson. Large-eddy simulations of the lillgrund wind farm. *Wind Energy*, 18(3):449–467, 2015.

[30] Matthew J Churchfield, Sang Lee, John Michalakes, and Patrick J Moriarty. A numerical study of the effects of atmospheric and wake turbulence on wind turbine dynamics. *Journal of turbulence*, (13):N14, 2012.

[31] Mandar Tabib, Adil Rasheed, and Trond Kvamsdal. Les and rans simulation of onshore bessaker wind farm: analysing terrain and wake effects on wind farm performance. In *Journal of Physics: Conference Series*, volume 625, page 012032. IOP Publishing, 2015.

[32] Rebecca Jane Barthelmie, K Hansen, Sten Tronæs Frandsen, Ole Rathmann, JG Schepers, W Schlez, J Phillips, K Rados, A Zervos, ES Politis, et al. Modelling and measuring flow and wind turbine wakes in large wind farms offshore. *Wind Energy*, 12(5):431–444, 2009.

[33] Matthew J Churchfield, Ye Li, and Patrick J Moriarty. A large-eddy simulation study of wake propagation and power production in an array of tidal-current turbines. *Philosophical Transactions of the Royal Society of London A: Mathematical, Physical and Engineering Sciences*, 371(1985):20120421, 2013.

[34] Matthew J Churchfield, Sang Lee, Patrick J Moriarty, Luis A Martinez, Stefano Leonardi, Ganesh Vijayakumar, and James G Brasseur. A large-eddy simulation of wind-plant aerodynamics. *AIAA paper*, 537:2012, 2012.

[35] Jens Norkær Sorensen and Wen Zhong Shen. Numerical modeling of wind turbine wakes. *Journal of fluids engineering*, 124(2):393–399, 2002.

[36] Y Bazilevs, M-C Hsu, I Akkerman, S Wright, K Takizawa, B Henicke, T Spielman, and TE Tezduyar. 3d simulation of wind turbine rotors at full scale. part i: Geometry modeling and aerodynamics. *International Journal for Numerical Methods in Fluids*, 65(1-3):207–235, 2011.

[37] Y Bazilevs, M-C Hsu, J Kiendl, R Wüchner, and K-U Bletzinger. 3d simulation of wind turbine rotors at full scale. part ii: Fluid–structure interaction modeling with composite blades. *International Journal for Numerical Methods in Fluids*, 65(1-3):236–253, 2011.

[38] Ming-Chen Hsu and Yuri Bazilevs. Fluid–structure interaction modeling of wind turbines: simulating the full machine. *Computational Mechanics*, 50(6):821–833, 2012.

[39] RB Langtry, Janusz Gola, and FR Menter. Predicting 2d airfoil and 3d wind turbine rotor performance using a transition model for general cfd codes. *AIAA paper*, 395:2006, 2006.

[40] Tarak N Nandi, James Brasseur, and Ganesh Vijayakumar. Prediction and analysis of the nonsteady transitional boundary layer dynamics for flow over an oscillating wind turbine airfoil using the γ-reθ transition model. In *34th Wind Energy Symposium*, page 0520, 2016.

[41] Raymond Chow and van CP Dam. Computational investigations of blunt trailing-edge and twist modifications to the inboard region of the nrel 5 mw rotor. *Wind Energy*, 16(3):445–458, 2013.

[42] Ph Devinant, T Laverne, and J Hureau. Experimental study of wind-turbine airfoil aerodynamics in high turbulence. *Journal of Wind Engineering and Industrial Aerodynamics*, 90(6):689–707, 2002.

[43] MS Adaramola and P-Å Krogstad. Experimental investigation of wake effects on wind turbine performance. *Renewable Energy*, 36(8):2078–2086, 2011.

[44] Fernando Porté-Agel, Yu-Ting Wu, Hao Lu, and Robert J Conzemius. Large-eddy simulation of atmospheric boundary layer flow through wind turbines and wind farms. *Journal of Wind Engineering and Industrial Aerodynamics*, 99(4):154–168, 2011.

[45] J Whale, KH Papadopoulos, CG Anderson, CG Helmis, and DJ Skyner. A study of the near wake structure of a wind turbine comparing measurements from laboratory and full-scale experiments. *Solar energy*, 56(6):621–633, 1996.

[46] Lee Jay Fingersh, Dave Simms, Maureen Hand, Dave Jager, Jason Cotrell, Mike Robinson, Scott Schreck, and Scott Larwood. Wind tunnel testing of nrel's unsteady aerodynamics experiment. *AIAA paper*, 35:2001, 2001.

[47] Richard Osgood, Gunjit Bir, Heena Mutha, Bart Peeters, Marcin Luczak, and Gert Sablon. Full-scale modal wind turbine tests: comparing shaker excitation with wind excitation. In *Structural Dynamics and Renewable Energy, Volume 1*, pages 113–124. Springer, 2011.

[48] Mads Damgaard, Jacob KF Andersen, et al. Natural frequency and damping estimation of an offshore wind turbine structure. In *The Twenty-second International Offshore and Polar Engineering Conference*. International Society of Offshore and Polar Engineers, 2012.

[49] Mads Damgaard, Lars Bo Ibsen, Lars Vabbersgaard Andersen, and Jacob KF Andersen. Cross-wind modal properties of offshore wind turbines identified by full scale testing. *Journal of Wind Engineering and Industrial Aerodynamics*, 116:94–108, 2013.

[50] AM Savill. One-point closures applied to transition. In *Turbulence and transition modelling*, pages 233–268. Springer, 1996.

[51] BJ Abu-Ghannam and R Shaw. Natural transition of boundary layers—the effects of turbulence, pressure gradient, and flow history. *Journal of Mechanical Engineering Science*, 22(5):213–228, 1980.

[52] FR Menter, T Esch, and S Kubacki. Transition modelling based on local variables. In *5th International Symposium on Turbulence Modeling and Measurements, Mallorca, Spain*, 2002.

[53] Demetri P Telionis and Demetri P Telionis. *Unsteady viscous flows*, volume 9. Springer, 1981.

[54] J. T. Stuart. In recent research of unsteady boundary layers. *E. A.*, 1, 1971.

[55] MM Zdravkovich. Flow around circular cylinders. fundamentals, vol. 1, 1997.

[56] T Maekawa and S Mizuno. Flow around the separation point and in the near-wake of a circular cylinder. *Physics of Fluids (1958-1988)*, 10(9):S184–S186, 1967.

[57] JH Gerrard. Experimental investigation of separated boundary layer undergoing transition to turbulence. *The Physics of Fluids*, 10(9):S98–S100, 1967.

[58] Gerrit H Toebes. The unsteady flow and wake near an oscillating cylinder. ASME, 1968.

[59] Kohsuke Shimizu and Masahiko Kawamura. Spanwise correlation measurement behind a circular cylinder in subcritical reynolds number region. *Journal of the Physical Society of Japan*, 32(5):1454–1454, 1972.

[60] JH Gerrard. The mechanics of the formation region of vortices behind bluff bodies. *Journal of Fluid Mechanics*, 25(02):401–413, 1966.

[61] Brian Cantwell and Donald Coles. An experimental study of entrainment and transport in the turbulent near wake of a circular cylinder. *Journal of fluid mechanics*, 136:321–374, 1983.

[62] Harish Gopalan, Peifeng Ma, Haihua Xu, Ankit Choudhary, Anis Hussain, and Rajeev K Jaiman. Hybrid rans-les formulations for wake interference physics in tandem cylinders and multi-column floaters. In *ASME 2015 34th International Conference on Ocean, Offshore and Arctic Engineering*, pages V002T08A005–V002T08A005. American Society of Mechanical Engineers, 2015.

[63] Luther N Jenkins, Mehdi R Khorrami, Meelan M Choudhari, and Catherine B McGinley. Characterization of unsteady flow structures around tandem cylinders for component interaction studies in airframe noise. *AIAA paper*, 2812:2005, 2005.

[64] Con J Doolan. Flow and noise simulation of the nasa tandem cylinder experiment using openfoam. *AIAA paper*, 3157, 2009.

[65] Mehdi R Khorrami, Meelan M Choudhari, David P Lockard, Luther N Jenkins, and Catherine B McGinley. Unsteady flowfield around tandem cylinders as prototype component interaction in airframe noise. *AIAA journal*, 45(8):1930–1941, 2007.

[66] Zhixiang Xiao, Jian Liu, Jingbo Huang, and Song Fu. Comparisons of three improved des methods on unsteady flows past tandem cylinders. In *Progress in Hybrid RANS-LES Modelling*, pages 231–243. Springer, 2012.

[67] M. Weinmann, R.D. Sandberg, and C. Doolan. Tandem cylinder flow and noise predictions using a hybrid rans/les approach. *International Journal of Heat and Fluid Flow*, 50(0):263 – 278, 2014.

[68] Sunghan Kim, Philip A Wilson, and Zhi-Min Chen. Effect of turbulence modelling on 3-d les of transitional flow behind a circular cylinder. *Ocean Engineering*, 100:19–25, 2015.

[69] Dmitry A Lysenko, Ivar S Ertesvåg, and Kjell Erik Rian. Large-eddy simulation of the flow over a circular cylinder at reynolds number 2× 104. *Flow, turbulence and combustion*, 92(3):673–698, 2014.

[70] Michael Breuer. A challenging test case for large eddy simulation: high reynolds number circular cylinder flow. *International Journal of Heat and Fluid Flow*, 21(5):648–654, 2000.

[71] Y Takagi, N Fujisawa, T Nakano, and A Nashimoto. Cylinder wake influence on the tonal noise and aerodynamic characteristics of a naca0018 airfoil. *Journal of Sound and Vibration*, 297(3):563–577, 2006.

[72] Stefan Szepessy. On the spanwise correlation of vortex shedding from a circular cylinder at high subcritical reynolds number. *Physics of Fluids (1994-present)*, 6(7):2406–2416, 1994.

[73] Charles HK Williamson. Vortex dynamics in the cylinder wake. *Annual review of fluid mechanics*, 28(1):477–539, 1996.

[74] Luther N Jenkins, Dan H Neuhart, Catherine B McGinley, Meelan M Choudhari, and Mehdi R Khorrami. Measurements of unsteady wake interference between tandem cylinders. *AIAA paper*, 3202:2006, 2006.

[75] Christoffer Norberg. Fluctuating lift on a circular cylinder: review and new measurements. *Journal of Fluids and Structures*, 17(1):57–96, 2003.

[76] Daniel R. Cadel. *Advanced instrumentation and measurement techniques for near surface flows*. PhD thesis, Virginia Tech, 2016.

[77] Rodolphe Perrin, Emmanuel Cid, Sebastien Cazin, Alain Sevrain, Marianna Braza, Franck Moradei, and Gilles Harran. Phase-averaged measurements of the turbulence properties in the near wake of a circular cylinder at high reynolds number by 2c-piv and 3c-piv. *Experiments in fluids*, 42(1):93–109, 2007.

[78] Raad I Issa. Solution of the implicitly discretised fluid flow equations by operator-splitting. *Journal of computational physics*, 62(1):40–65, 1986.

[79] Suhas V Patankar and D Brian Spalding. A calculation procedure for heat, mass and momentum transfer in three-dimensional parabolic flows. *International journal of heat and mass transfer*, 15(10):1787–1806, 1972.

[80] Florian R Menter. Two-equation eddy-viscosity turbulence models for engineering applications. *AIAA journal*, 32(8):1598–1605, 1994.

[81] David C Wilcox. Reassessment of the scale-determining equation for advanced turbulence models. *AIAA journal*, 26(11):1299–1310, 1988.

[82] Robin B Langtry and Florian R Menter. Correlation-based transition modeling for unstructured parallelized computational fluid dynamics codes. *AIAA journal*, 47(12):2894–2906, 2009.

[83] Philippe R Spalart, S Deck, ML Shur, KD Squires, M Kh Strelets, and A Travin. A new version of detached-eddy simulation, resistant to ambiguous grid densities. *Theoretical and computational fluid dynamics*, 20(3):181–195, 2006.

[84] PR Spalart, WH Jou, M Strelets, and SR Allmaras. Comments on the feasibility of les for wings, and on a hybrid rans/les approach. *Advances in DNS/LES*, 1:4–8, 1997.

[85] Mikhail S Gritskevich, Andrey V Garbaruk, Jochen Schütze, and Florian R Menter. Development of ddes and iddes formulations for the k-ω shear stress transport model. *Flow, turbulence and combustion*, 88(3):431–449, 2012.

[86] Philippe R Spalart and Christopher L Rumsey. Effective inflow conditions for turbulence models in aerodynamic calculations. *AIAA journal*, 45(10):2544–2553, 2007.

[87] Raymond Morton Hicks and Edward T Schairer. Effects of upper surface modification on the aerodynamic characteristics of the naca 63 sub 2-215 airfoil section. 1979.

[88] J Coupland. Separation and transition over a semi-circular leading edge: T3l transition cases. *Rolls-Royce Applied Science Laboratory Data, ERCOFTAC Transition Modeling Special Interest Group, http://transition. imse. unige. it/cases.*

[89] Robin Blair Langtry. A correlation-based transition model using local variables for unstructured parallelized cfd codes. 2006.

[90] DM Somers. Design and experimental results for the s809 airfoil nrel. Technical report, sr-440-6918. Tech. rep., NREL, 1997.

[91] JL Van Ingen, LMM Boermans, and JJH Blom. Low-speed airfoil section research at delft university of technology. In *12th Congress of the International Council of the Aeronautical Sciences*, 1980.

[92] Robin Blair Langtry, FR Menter, SR Likki, YB Suzen, PG Huang, and S Völker. A correlation-based transition model using local variables—part ii: Test cases and industrial applications. *Journal of Turbomachinery*, 128(3):423–434, 2006.

[93] M Shur, PR Spalart, M Strelets, and A Travin. Detached-eddy simulation of an airfoil at high angle of attack. *Engineering turbulence modelling and experiments*, 4:669–678, 1999.

[94] Hilary Weller. Controlling the computational modes of the arbitrarily structured c grid. *Monthly Weather Review*, 140(10):3220–3234, 2012.

[95] C Norberg. Flow around a circular cylinder: aspects of fluctuating lift. *Journal of Fluids and Structures*, 15(3-4):459–469, 2001.

[96] GH Toebes. Fluidelastic features of flow around cylinders. In *Proceedings of the International Research Seminar, Wind Effects on Buildings and Structures*, pages 323–341, 1967.

[97] JCR Hunt and JMR Graham. Free-stream turbulence near plane boundaries. *Journal of Fluid Mechanics*, 84(02):209–235, 1978.

[98] Stephen B Pope. Turbulent flows, 2001.

[99] DB Spalding. A single formula for the “law of the wall”. *Journal of Applied Mechanics*, 28(3):455–458, 1961.

[100] Contrib/swak4foam.

[101] John David Anderson and J Wendt. *Computational fluid dynamics*, volume 206. Springer, 1995.

[102] Howard Wilson Emmons. The laminar-turbulent transition in a boundary layer—part i. *J. aeronaut. Sci*, 18(7):490–498, 1951.

[103] A Garbaruk, M Shur, M Strelets, PR Spalart, and R Balakrishnan. Ddes and iddes of tandem cylinders. *Proceedings of the Benchmark problems for Airframe Noise Computations BANC*, 2010.

[104] BW Van Oudheusden. Piv-based pressure measurement. *Measurement Science and Technology*, 24(3):032001, 2013.

[105] Gerrit E Elsinga, Fulvio Scarano, Bernhard Wieneke, and Bas W van Oudheusden. Tomographic particle image velocimetry. *Experiments in fluids*, 41(6):933–947, 2006.

[106] Jian Sheng, Edwin Malkiel, and Joseph Katz. Digital holographic microscope for measuring three-dimensional particle distributions and motions. *Applied optics*, 45(16):3893–3901, 2006.

[107] Christian Willert. Stereoscopic digital particle image velocimetry for application in wind tunnel flows. *Measurement science and technology*, 8(12):1465, 1997.

[108] Ronald J Adrian. Scattering particle characteristics and their effect on pulsed laser measurements of fluid flow: speckle velocimetry vs particle image velocimetry. *Applied optics*, 23(11):1690–1691, 1984.

[109] Ajay K Prasad. Particle image velocimetry. *CURRENT SCIENCE-BANGALORE-*, 79(1):51–60, 2000.

[110] Davide Medici and PH Alfredsson. Measurements on a wind turbine wake: 3d effects and bluff body vortex shedding. *Wind Energy*, 9(3):219–236, 2006.

[111] Philip Ernest Hancock and P Bradshaw. The effect of free-stream turbulence on turbulent boundary layers. *Journal of Fluids Engineering*, 105(3):284–289, 1983.

[112] Xiaolei Yang, Fotis Sotiropoulos, Robert J Conzemius, John N Wachtler, and Mike B Strong. Large-eddy simulation of turbulent flow past wind turbines/farms: the virtual wind simulator (vwis). *Wind Energy*, 18(12):2025–2045, 2015.

[113] FR Menter and Y Egorov. The scale-adaptive simulation method for unsteady turbulent flow predictions. part 1: theory and model description. *Flow, Turbulence and Combustion*, 85(1):113–138, 2010.

[114] Pankaj K Jha, Matthew J Churchfield, Patrick J Moriarty, and Sven Schmitz. The effect of various actuator-line modeling approaches on turbine-turbine interactions and wake-turbulence statistics in atmospheric boundary-layer flow. In *Proceedings of the 52th AIAA Aerospace Sciences Meeting, National Harbor, MD, USA*, volume 1317, 2014.

[115] Nilay Sezer-Uzol and Lyle N Long. 3-d time-accurate cfd simulations of wind turbine rotor flow fields. *AIAA paper*, 394:2006, 2006.

[116] Ryan Wiser and Mark Bolinger. 2015 wind technologies market report. *Energy Efficiency and Renewable Energy*, 2015.